



## Durham E-Theses

---

### *Extreme Conditions Crystallography of Polymorphic Co-crystals*

LEE, RACHAEL

#### How to cite:

---

LEE, RACHAEL (2017) *Extreme Conditions Crystallography of Polymorphic Co-crystals*, Durham theses, Durham University. Available at Durham E-Theses Online: <http://etheses.dur.ac.uk/12065/>

#### Use policy

---

The full-text may be used and/or reproduced, and given to third parties in any format or medium, without prior permission or charge, for personal research or study, educational, or not-for-profit purposes provided that:

- a full bibliographic reference is made to the original source
- a [link](#) is made to the metadata record in Durham E-Theses
- the full-text is not changed in any way

The full-text must not be sold in any format or medium without the formal permission of the copyright holders.

Please consult the [full Durham E-Theses policy](#) for further details.

# Extreme Conditions Crystallography of Polymorphic Co-crystals

---

Rachael Lee

Thesis submitted in part fulfilment of the requirements for the degree of  
Doctor of Philosophy at Durham University

Department of Chemistry  
Durham University

2016

### *Declaration*

The work described herein was carried out by Rachael Lee at Durham University between October 2012 and September 2016 under the supervision of Prof. J. W. Steed and Dr. M. R. Probert. All work described was carried out by the author, unless otherwise stated and acknowledged by reference. This work has not been submitted for any other degree at this or any other university previously.

### *Statement of Copyright*

The copyright of this thesis rests with the author. No part of this thesis may be reproduced, transmitted or translated without prior written consent and information derived from it should be acknowledged.

# Abstract

---

This work has two principal sections. The first section is a study of the hydrogen bonding in a series of urea inclusion compounds, utilising neutron diffraction methods and a novel technique for growing neutron diffraction-suitable single crystals. The second section focusses on high pressure crystallography as a technique for exploring polymorphic landscapes, of a series of acid-base co-crystals, and the well-known active pharmaceutical ingredient 5-methyl-2-[(2-nitrophenyl)amino]-3-thiophenecarbonitrile (ROY).

Single crystal neutron structures at several temperatures have been determined for  $\beta$ -phase urea inclusion compounds containing hexadecane, 1,6-dibromohexane and 2,7-octanedione guests. The neutron structure of the 'partial channel' co-crystal of urea and DMF is also reported. This includes an in-depth discussion and analysis of the structure and bonding of this urea series, in particular, how the guest compound affects the symmetry and hydrogen bonding of the host urea network. Additionally, the challenge of obtaining crystals suitable for neutron diffraction is addressed and a new heating/cooling device to aid crystallisation is presented.

Pyridine and formic acid have been crystallised at differing ratios by both cryo-crystallisation and compression in a diamond anvil cell. Mixtures of the liquids in 1:1, 1:2 and 1:4 ratios all crystallise at high pressure, while only the 1:1 and 1:4

compositions were crystallised by *in situ* low temperature capillary crystallisation. The 1:2 structure crystallised by high pressure is a previously unknown co-crystal of pyridine - formic acid. For the 1:4 mixture, a new polymorph has been identified at a pressure of 14.2 kbar with a distinctly different structure and bonding pattern to that of the previously reported low temperature form.

Five new co-crystals of 2,6-dimethylpyridine (DMP) with formic acid (FA) were crystallised by application of pressure in a diamond anvil cell and by *in situ* cryo-crystallisation. Mixtures in ratios 1:1, 1:2 and 1:3 of DMP: FA have been crystallised *via* both methods. Both the 1:2 and 1:3 co-crystals exhibit high pressure/low temperature polymorphism.

ROY has been crystallised from acetone solution using a diamond anvil cell. The needle-like form obtained, named ONP shows similarities with the ORP, ON and Y forms, determined by Raman spectroscopy. The ONP crystals were recovered from the pressure cell by freezing with liquid nitrogen. Synchrotron X-ray data were collected on the sample, although no structure solution and refinement was possible. The unit cell of the ONP shows a crystallographic relationship to the ORP form.

### *Acknowledgements*

My sincerest thanks to:

My supervisors Jon Steed and Mike Probert for all their support and help throughout my stint in academia. Their curiosity and passion for chemistry made it easy for me to feel the same and was particularly welcome on difficult days. I had an excellent supervisory team to turn to who always helped me feel much better about the on-goings of my PhD. I'll always be grateful for the opportunities to travel that came with my studies, to conferences and experimental facilities, the chance to see some wonderful places and meet some lovely people.

Judith Howard, for so warmly welcoming me to Durham and for helping me to find a place here. I remember being surprised the day I came to Durham to have a cup of tea and a chat, and walking out with an offer of a studentship, wondering what had happened.

Dmitry Yufit, for all the crystallography tips and tricks, for the always cheerful and patient attitude.

The folks at ILL for being accommodating and enthusiastic about working with me, and making me feel like I was doing science when I was actually sipping coffee or wine at the foot of the French Alps.

Both the Steed and Probert groups in Durham and Newcastle for being such a friendly and competent bunch of people. It's been a genuine pleasure to work and laugh with all of them. Having a supportive and knowledgeable group certainly makes work more enjoyable. In particular, thanks Andrea and Chris for being the voices of reason and encyclopaedic knowledge.

Kerrie, for the support, sanity checks and dragging me out of the house when I needed it. Andrew, for the copious tea breaks and chats.

And thank you to my parents for their endless love and support, which has always been constant, but particularly needed and appreciated these last few years.

*Table of Contents*

Chapter 1 Introduction to crystallographic techniques .....	1
1.1 Crystallography .....	1
1.1.1 Diffraction theory .....	2
1.1.2 Polymorphism .....	6
1.2 Extreme conditions crystallography.....	10
1.2.1 High pressure crystallography techniques.....	14
1.2.2 Low temperature crystallography.....	27
1.3 Neutron diffraction .....	31
1.4 Raman Spectroscopy .....	33
1.5 References.....	34
Chapter 2 Introduction to supramolecular chemistry .....	38
2.1 Co-crystals .....	38
2.2 Inclusion compounds .....	40
2.2.1 Hydroquinone .....	42
2.2.2 Calixarenes .....	42
2.2.3 Urea.....	46
2.3 Effects of extreme conditions on supramolecular solids.....	47



2.4 Concluding remarks.....	61
2.5 References.....	62
Chapter 3 Neutron Diffraction Studies on Guest-Induced Distortions in Urea Inclusion Compounds.....	65
3.1 Introduction .....	65
3.2 Experimental .....	68
3.2.1 Design of a heating/cooling Peltier thermoelectric cooler.....	70
3.3 Results .....	71
3.3.1 Urea Hexadecane .....	74
3.3.2 Urea 1,6-dibromohexane.....	78
3.3.3 Urea 2,7-octanedione .....	78
3.3.4 Urea – DMF co-crystal.....	80
3.3.5 High pressure studies.....	82
3.4 Discussion.....	83
3.5 Conclusions .....	95
3.6 References .....	96
Chapter 4 Expanding the pyridine-formic acid co-crystal landscape under extreme conditions.....	98
4.1 Introduction .....	98

4.2 Experimental .....	99
4.3 Results and Discussion .....	100
4.3.1 Pyridine Formic acid 1:1 .....	100
4.3.2 Pyridine-Formic acid 1:2 .....	102
4.3.3 Pyridine formic acid 1:4 .....	104
4.3.4 Proton transfer .....	108
4.4 Conclusions .....	111
4.5 References.....	112
Chapter 5 High Pressure/ Low Temperature Polymorphism in 2,6-Dimethylpyridine Formic Acid Co-crystals. ....	114
5.1 Introduction .....	114
5.2 Experimental .....	115
5.3 Results .....	117
5.3.1 1:1 DMP-FA .....	118
5.3.2 1:2 DMP-FA .....	119
5.3.3 1:3 DMP-FA .....	122
5.4 Discussion.....	126
5.5 Conclusions .....	129

5.6 References.....	130
Chapter 6 Polymorphism of ROY at high pressure .....	131
6.1 Introduction .....	131
6.2 Experimental .....	135
6.3 Results and Discussion .....	136
6.3.1 Synchrotron diffraction data .....	142
6.4 Conclusions .....	148
6.5 References.....	149
Chapter 7 Conclusions and future work .....	150
7.1 Acid-base co-crystals.....	150
7.2 High pressure ROY crystallisation .....	152
7.3 Urea inclusion compounds.....	153
Courses.....	155
Conferences and Meetings .....	155
Publications.....	155

*Table of Figures*

Figure 1-1. Reflection of X-ray incident beam by lattice planes.....	3
Figure 1-2. Interference between X-ray beams.....	4
Figure 1-3. Phase diagram of sulfur.....	8
Figure 1-4. XIPHOS II diffractometer for high pressure diffraction, with DAC.....	13
Figure 1-5. Diamond Anvil Cell. (Top) An open DAC. (Bottom) Components within the DAC.....	15
Figure 1-6. BETSA the spark eroder.....	24
Figure 1-7. Ruby fluorescence at high pressure (orange) and ambient pressure (blue).....	26
Figure 1-8. Open flow nitrogen gas cryostat.....	28
Figure 1-9. Scattering factors for neutron diffraction.....	32
Figure 1-10. Energy levels and emissions involved in Raman scattering.....	34
Figure 2-1. $\beta$ -quinol inclusion compound with nitric oxide shown as space filling; A) down <i>c</i> cell axis, B) capsule consisting of six hydroquinone molecules and one NO. (Disordered with respect to NO).....	42
Figure 2-2. <i>p</i> -tert-butylcalix[4]arene.....	43
Figure 2-3. <i>p</i> -tert-butylcalix[4]arene inclusion compounds with A) 1,3,5-trifluorobenzene <sup>30</sup> B) <i>n</i> -butylamine <sup>31</sup> (disordered) and C) azobenzene guests.....	44
Figure 2-4. A) Crystal structure of $\alpha$ -urea. B) $\alpha$ -tape bonding in disubstituted urea. <sup>37</sup> .....	47
Figure 2-5. Ambient and high pressure phases of urea: (a) $\alpha$ -phase $P4_21m$ (b) $\gamma$ -phase $P2_12_12_1$ (c) $\delta$ -phase $P2_12_12_1$ .....	50
Figure 2-6. The HP and LT forms of 3-fluorotoluene.....	53
Figure 2-7. The phases of pyrazole showing partial charges and symmetry relationships present in the hydrogen bonding 'loop'.....	55
Figure 2-8. Polymorphs of diphenyl ether. A) Form I $P2_1/n$ (250 K). B) Form II $P2_12_12_1$ (240 K).....	59

Figure 3-1. X-ray structure of urea with hexadecane guest, viewed down <i>c</i> axis. Host structure only is shown for clarity. ....	66
Figure 3-2. a) Hexadecane. a) 2,7-octanedione. c) 1,6-dibromohexane. d) N,N-dimethylformamide. ....	74
Figure 3-3. View along <i>c</i> axis of urea/hexadecane showing cross section of one 1D channel with unit cell superimposed. Hexadecane appears as a grey dot in the channel centre. ....	75
Figure 3-4. Crystal of HEX mounted on a vanadium pin. ....	76
Figure 3-5. Peak splitting on cooling HEX a) 151 K, b) 150 K, c) 149 K.....	76
Figure 3-6. Hydrogen bonds in UIC of hexadecane. All urea molecules are equivalent. Hexadecane guest omitted for clarity. ....	77
Figure 3-7. a) View down the <i>b</i> axis of 1,6-dibromohexane UIC with unit cell superimposed. b) Space filling representation of the unit cell.....	78
Figure 3-8. View down <i>c</i> axis of 2,7-octanedione UIC with unit cell superimposed. $P6_122$ $a, b = 8.1266(6), c = 76.297(6)$ .....	79
Figure 3-9. Hydrogen bonding between host and guest in OCT.....	80
Figure 3-10. Pseudo-hexagonal packing of UDM, with unit cell superimposed.....	81
Figure 3-11. (Left) Crystals from initial crystallisation attempts of OCT. The arrows indicate where the crystal layers are separating. (Right) Crystals obtained using the TEC.....	84
Figure 3-12. Diagrammatic representations of channel cross-sections and associated lengths/angles for the UIC series (left to right) with guests hexadecane, 1,6-dibromohexane and 2,7-octanedione. ....	87
Figure 3-13. Structure of DBH derived from X-ray data (top) and neutron (bottom) showing the difference in hydrogen atom positions from the two methods. ....	91
Figure 3-14. Pseudo $\alpha$ -urea tape in UDM from two viewpoints.....	93
Figure 3-15. Hydrogen bonding motif in UDM (top) and HEX (bottom). ....	94
Figure 4-1. (Left) Stacking between pyridine rings showing how key parameters are defined. (Right) View down the <i>a</i> axis of pyridine formic acid 1:1, showing layers extending in the <i>c</i> axis direction. ....	101

Figure 4-2. Asymmetric unit of pyridine-formic acid 1:2 (HP) showing the primary hydrogen bonding motif. ....	102
Figure 4-3. Hydrogen bonding interactions between pyridinium and formate ions in the HP 1:2 structure. ....	103
Figure 4-4. View down the $a$ axis of the 1:4 adduct. a) High pressure and b) low temperature. ....	104
Figure 4-5. Asymmetric units of a) high pressure and b) low temperature polymorphs of pyridinium formate tris(formic acid). ....	105
Figure 4-6. Hirshfeld 2D fingerprint plots of 1:1, 1:2, 1:4 HP and 1:4 LT crystal structures of pyridine-formic acid. a) Whole surface, b) OH interactions, c) NH interactions. ....	109
Figure 5-1. $\pi$ - $\pi$ stacking interactions of DMP- FA crystallised with high pressure. .	119
Figure 5-2. 2,6-dimethylpyridinium formate formic acid co-crystal asymmetric units from HP and LT crystallisation. ....	120
Figure 5-3. Packing arrangements of 1:2 DMP-FA from HP and LT. ....	122
Figure 5-4. Asymmetric unit of 1:3 DMP-FA co-crystals. ....	123
Figure 5-5. Overlay of HP and LT structures of 1:3 2,6-dimethylpyridinium formate bis(formic acid). ....	124
Figure 5-6. Space-filling packing diagrams showing the environment of the pyridyl ring in a) HP 1:4 pyridine-FA and b) HP 1:3 DMP-FA. ....	125
Figure 5-7. Hirshfeld surface fingerprint plots of DMP-FA; a) 1:1 LT, b) 1:2 LT, c) 1:2 HP, d) 1:3 LT and e) 1:3 HP, showing features from N-H interactions (1) O-H interactions (2-4, 6) and H-H interactions (5). ....	127
Figure 6-1. Molecular structure of ROY, with torsional angle $\vartheta$ . ....	131
Figure 6-2. Polymorphs of ROY. Adapted with permission from L. Yu, <i>Acc. Chem. Res.</i> , 2010, 43, 1257-1266. Copyright 2010 American Chemical Society .....	133
Figure 6-3. Crystals grown in DAC by application of pressure. A) Y crystals. B) ONP nucleating on gasket surface. C) ONP needles filling the cell. D) Larger ONP needles grown by pressure cycling. ....	138
Figure 6-4. ROY crystals on diamond surface after opening of DAC. A) ONP form. B) Y form. C) Edge of diamond culet. ....	140

Figure 6-5. Raman spectrum of ROY needles grown in a DAC, once recovered from the cell.  $\nu_{\text{CN}}$  peak is highlighted.....141

Figure 6-6. Single diffraction frame of ROY crystals collected on I19, DLS.....144

Figure 6-7. Reciprocal lattice of reflections from ONP crystals. (Top) Total reflections from one data collection. (Bottom) Individual lattice from single crystal.....145

*Table of tables*

Table 1-1. Cell centring types of a lattice unit cell. ....	2
Table 1-2. Crystal systems.....	2
Table 1-3. Limits of hydrostatic media. <sup>52-54</sup> .....	25
Table 3-1. Summary of crystallographic data from neutron diffraction experiments. .....	73
Table 3-2. Unit cells collected at high pressure .....	82
Table 3-3. Occupied space for all structures.....	83
Table 3-4. Hydrogen bonding parameters for HEX at 150 K, and DBH, OCT and UDM at 30 K, determined from neutron diffraction data.....	85
Table 3-5. Parameters of hexagonal cross-section for each UIC. ....	87
Table 3-6. Average hydrogen bond parameters for HEX, DBH, OCT and UDM from neutron data. ....	88
Table 3-7. Torsion angles of all bonding hydrogen atoms in DBH at 30 K, using N-C-N to define the plane of the associated urea molecule. ....	91
Table 3-8. Torsion angles of bonding hydrogen atoms in OCT at 30 K.....	92
Table 4-1. Hydrogen bond details for the unique hydrogen bond in a 1:1 co-crystal of pyridine formic acid. ....	102
Table 4-2. Details of N1-H1...O7 hydrogen bond contact in the high pressure structure of 1:2 pyridine-formic acid. ....	104
Table 4-3. Percentage of unit cell occupied by Py-FA structures. ....	107
Table 4-4. Summary of Crystallographic data.....	107
Table 4-5. Hydrogen bond parameters for pyridine-formic acid series. ....	109
Table 5-1. Summary of crystallographic data. ....	117
Table 5-2. N-H...O bond distances and angles for all structures from X-ray diffraction data. ....	118
Table 5-3. Hydrogen bonding parameters of 1:2 DMP-FA HP .....	121



Table 5-4. Hydrogen bond parameters of HP and LT polymorphs of 1:3 DMP-FA..	125
Table 6-1. Crystallisation solvents of common polymorphs of ROY. <sup>10</sup> .....	134
Table 6-2. Characteristic $\nu_{\text{CN}}$ Raman stretches of ROY polymorphs. <sup>10, 26</sup> .....	142
Table 6-3. Polymorphs of ROY. ....	147

# Chapter 1 Introduction to crystallographic techniques

---

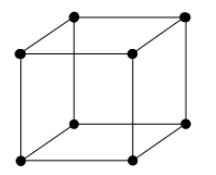
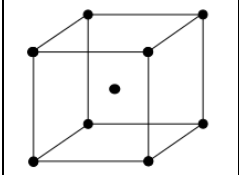
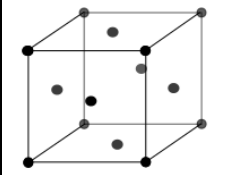
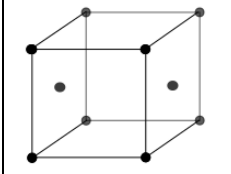
## 1.1 Crystallography

A crystal is a solid form composed of many atoms, molecules or ions which are arranged in a regular repetitive way, giving rise to a highly ordered structure.

Crystals may have a periodic order, aperiodic (quasicrystals),<sup>1</sup> or be incommensurately modulated and hence require higher dimensionality (a superspace group) to describe the symmetry.<sup>2</sup> However, the common defining characteristic between all crystals is that they will diffract an incident beam of X-rays (or neutrons) to give discrete diffraction peaks.

A crystal structure can be reduced to a single unit cell, the parameters, contents and symmetry of which can be used to describe the entire crystal. A crystal can also be described in terms of its lattice; a series of identical points related to each other by translation, which describes the symmetry of the crystal structure but not its contents. A unit cell is chosen by connecting a number of lattice points (Table 1-1).

Table 1-1. Cell centring types of a lattice unit cell.

Type	Primitive (P)	Body centred (I)	Face centred (F)	Cubic (C)
Lattice points	$8 \times 1/8$	$(8 \times 1/8) + 1$	$(8 \times 1/8) + (6 \times 1/2)$	$(8 \times 1/8) + (2 \times 1/2)$
Total	1	2	4	2
View				

A structure which has no symmetry but the identity operation has no restrictions on what the unit cell parameters  $a$ ,  $b$ ,  $c$ ,  $\alpha$ ,  $\beta$  and  $\gamma$  may be, but higher symmetry imposes restrictions on these values. These restrictions can be categorised into seven crystal systems, which together with the four lattice centring types give the fourteen Bravais lattices (Table 1-2).

Table 1-2. Crystal systems

Crystal system	Laue class	Centring types	Restrictions
Triclinic	-1	<i>P</i>	None
Monoclinic	$2/m$	<i>P C</i>	$\alpha = \gamma = 90^\circ$
Orthorhombic	$mmm$	<i>P C I F</i>	$\alpha = \beta = \gamma = 90^\circ$
Tetragonal	$4/m, 4/mmm$	<i>P I</i>	$a = b; \alpha = \beta = \gamma = 90^\circ$
Trigonal	$-3, -3m$	<i>P</i>	$a = b; \alpha = \beta = 90^\circ \gamma = 120^\circ$
Hexagonal	$6/m, 6/mmm$	<i>P</i>	$a = b; \alpha = \beta = 90^\circ \gamma = 120^\circ$
Cubic	$m-3, m-3m$	<i>P I F</i>	$a = b = c; \alpha = \beta = \gamma = 90^\circ$

### 1.1.1 Diffraction theory

Bragg surmised that the occurrence of diffraction can be treated as a series of incident beams being reflected by parallel lattice planes within a crystal (Figure

1-1).<sup>3</sup> When constructive interference occurs between the two beams, and Bragg's Law is satisfied (Equation 1-1, Figure 1-2), a reflection is observed.

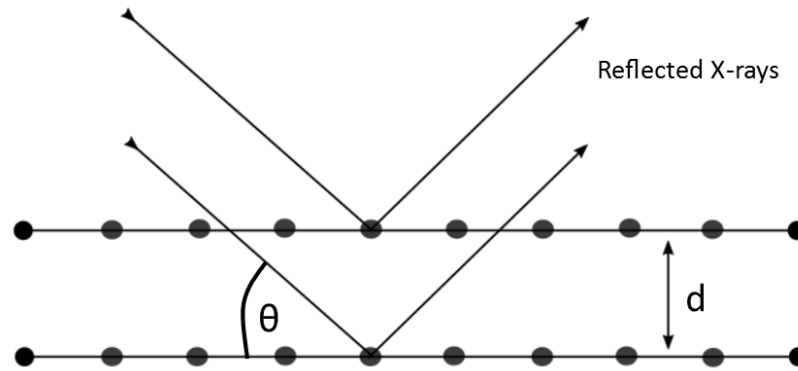


Figure 1-1. Reflection of X-ray incident beam by lattice planes.

$$n\lambda = 2d\sin\theta$$

Equation 1-1. Bragg's Law

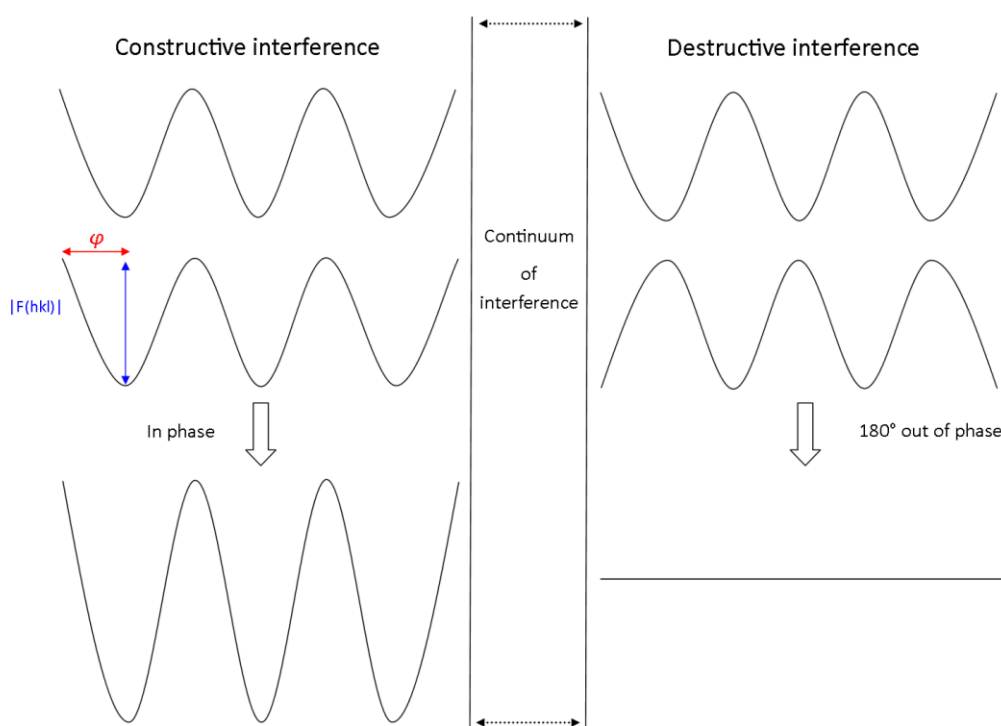


Figure 1-2. Interference between X-ray beams.

Once a dataset of diffraction intensities is collected, indexation determines the unit cell parameters and the crystal system (Table 1-2). Data integration generates a set of integrated intensity files to which systematic corrections can be applied such as  $L_p$  and absorption corrections.<sup>4,5</sup> Systematic absences and equivalent intensities of diffraction peaks are used for space group determination. Data reduction generates a reflection file, which contains information about each indexed reflection such as  $hkl$  values amplitudes and phases.

Each X-ray reflection  $hkl$ , diffracted by a crystal will have an associated amplitude  $|F(hkl)|$  and phase  $\varphi(hkl)$  (Figure 1-2), together these give the structure factor:

$$F(hkl) = |F(hkl)|\exp[i\varphi(hkl)]$$

**Equation 1-2. Structure factor.**

The structure factor contains all the necessary information about the diffracted beam, and  $i$  is used to separate the terms. The intensity of the diffracted beam is directly proportional to the square of the amplitude, so  $|F(hkl)|$  is easily measured (Equation 1-3). The phase information however, is lost during data collection. This is known as the phase problem.

$$|F(hkl)| = K \sqrt{\frac{I_{hkl}}{Lp. Abs}}$$

**Equation 1-3. Structure factor relation to intensity  $I_{hkl}$ .**

A number of popular approaches to addressing the phase problem collectively fall under Direct Methods, which uses the following information to approximate phase relationships:

1. The intensities obtained from data collection.
2. At any point in the crystal, the electron density must be zero or positive. The phases must be related to each other in a way which leaves no negative electron density at any point.
3. The electron density is clustered together at positions where there are atoms.

4. For centrosymmetric structures, the phase angle can only be 0 or 180°.

Using this information, a set of phases based on a random number seed is assigned initially to stronger reflections, and together with the observed amplitudes, a set of calculated structure factors are generated which undergo a Fourier transform to give an initial electron density map, from which a trial structure can be approximated (Equation 1-4).

$$\rho(hkl) = \frac{1}{V} \sum_h \sum_k \sum_l F(hkl) \exp[-2\pi i(hx + ky + lz)]$$

**Equation 1-4. Electron density and structure factor relationship.**

This model is used to calculate a new set of phases for the dataset and the process is repeated iteratively until a sensible set of phases, and thus a crystallographically reasonable structure, is obtained. It is worth noting that the diffraction pattern is the Fourier transform of the electron density in the crystal structure, so the diffraction experiment is a physical Fourier transform. The reverse Fourier transform is carried out mathematically in order to model the electron density. This structure solution and refinement often utilises the SHELX program suite, which uses least squares matrix refinements to best model the crystal structure.<sup>6</sup>

### 1.1.2 Polymorphism

Polymorphism is a common occurrence in crystal structures, with many elements, molecules and mixtures having more than one crystal form. This characteristic is of

considerable importance in many fields, as the properties of polymorphs can differ significantly from one another. Sulfur offers a classic example, with three crystalline polymorphs among its allotropes; orthorhombic,  $\beta$ -monoclinic and  $\gamma$ -monoclinic (Figure 1-3).<sup>7, 8</sup> In the pharmaceutical industry in particular any potential polymorphism of a drug compound must be investigated thoroughly as different crystal forms of a drug substance can have vastly different solubility, bioavailability and other properties which contribute significantly to the safety and efficacy of the medicine.<sup>9-11</sup>

Despite its industrial and pharmaceutical importance, polymorphism is not yet fully understood, and obtaining different polymorphs of a substance can be somewhat of a dark art. Disappearing polymorphs are occasionally glimpsed, before never being obtained again without significant effort, likely due to seeding effects.<sup>12</sup> Polymorphs which should be stable may never be seen in reality, although can be explored computationally by crystal structure prediction (CSP).<sup>13</sup> However, polymorphs are regularly obtained by simple alterations in crystallisation conditions such as the method chosen, the solvent, temperature and pressure.

Polymorphism at high pressure (HP) is a technique that has been gaining interest, with drastic improvements in the equipment available over the past few decades. As a result, it is becoming a more common way to map a substance's structural and polymorphic behaviour (Figure 1-3). While previously the realm of planetary



scientists and geologists, high pressure crystallography is now more widespread as a technique.<sup>14</sup>

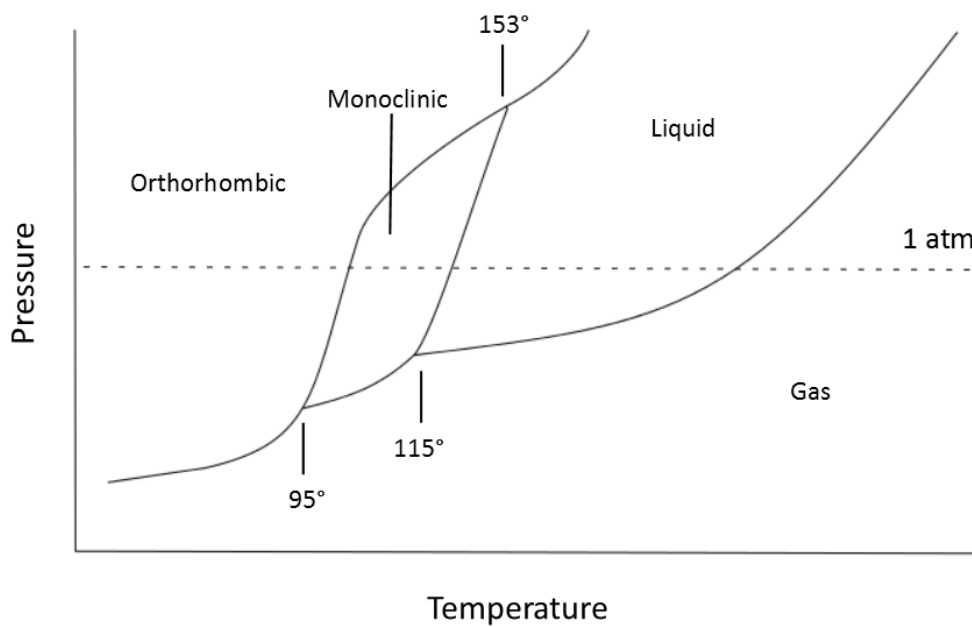


**Figure 1-3. Phase diagram of sulfur.**

The crystallisation of multiple polymorphs of a given substance depends on both kinetic and thermodynamic factors. Variation of temperature and pressure can significantly expand the solid form landscape; some polymorphs are stable only within a narrow range of temperatures and pressure, while others are only obtainable through the application of pressure to a liquid, solution, or existing single crystal which can undergo a phase transition.<sup>15</sup> Examples of compounds which exhibit polymorphism at high pressure or low temperature (LT) are the common simple molecules water,<sup>16</sup> acetone,<sup>17</sup> and benzene,<sup>18</sup> as well as more

complex molecules such as 1-bromo-2,4,6-trifluorobenzene<sup>19</sup> and various amino acids.<sup>20, 21</sup>

Computational crystal structure prediction has proven to be an effective tool in recent years at predicting crystal structure and polymorphism in some substances, and can give an indication of the existence of possible high-pressure polymorphs of a compound, which tend to fall in the higher density region of the energy-density landscape. A series of blind tests on CSP methods have shown how the technique has improved in the last fifteen years.<sup>22-25</sup> Examples are 2-fluorophenylacetylene<sup>26</sup> and 2- and 4-chlorophenol,<sup>27</sup> all of which exhibit HP/LT polymorphism which is reflected in the CSP results. Additionally, the cholesterol drug Dalcetrapib is an excellent example of a high pressure polymorph that has been correctly predicted using CSP, despite the failure of initial crystallisation attempts.<sup>28</sup> Knowing there is a high possibility of such a polymorph's existence, an experimenter is more likely to persist in screening, which is particularly relevant to the pharmaceutical industry where fast, high-throughput screening techniques are preferred. These may overlook, or fail to find, the precise crystallisation conditions of a particular form. From CSP alone, without additional knowledge of the nature of HP/LT polymorphism, it is difficult to determine which structures can be accessed with high pressure. To address this shortcoming, it is useful to conduct further investigations into the subtle structural factors that contribute to polymorphism under different conditions.

Our group have recently shown that crystallisation of 2- and 3-fluorotoluene under high pressure affords structures different from those obtained at low temperature as a result of the dominance of close packing effects at HP rather than the very weak H···F hydrogen bonding (see Chapter 2).<sup>29</sup> It is possible that the presence of a stronger, structure-defining hydrogen bond in such a system would reduce the likelihood of HP/LT polymorphism. However, even in the presence of dominant hydrogen bonding, polymorphism arising from varying arrangements of weaker interactions in the crystal remains a distinct possibility.<sup>30</sup>

## 1.2 Extreme conditions crystallography

The behaviour of materials under extreme conditions, loosely defined as any conditions substantially outside of the ambient environment we live in, has long been of interest to scientists. Laboratory scale experiments under extreme conditions were initially developed by astrophysicists and geoscientists for the purpose of understanding planetary or extra-terrestrial environments. Pressures at the core of Earth reach several million atmospheres,<sup>31</sup> and less accommodating planets and stars have more bizarre conditions still. Early studies focused on the effect of heating, cooling and compression on elemental and mineral composites such as those found in planetary crusts and cores but has since been applied to more complex inorganic systems and organic molecular materials. Achieving extreme conditions in a simulated environment proved difficult in the early days of the science, requiring cumbersome setups impractical for use within conventional

university laboratories. Over the last half century, advances in both instrumentation and X-ray diffraction facilities and techniques have allowed high pressure and low temperature studies to develop as a routine method for investigating the structure and properties of a wide variety of materials. Collecting single crystal diffraction data at low temperatures has become standard practice in most laboratories due to advantageous effects such as reduction in thermal motion and diffuse scattering, as well as stabilisation of sensitive samples, which together offer better data quality and ultimately, more precise and accurate crystal structures. With continual improvement in the variety and availability of cooling systems and the accessibility of temperatures close to absolute zero, it is becoming evident that more can be learned from these conditions as materials exhibit new and unusual properties at low temperature. In terms of high pressure studies, the invention of the Diamond Anvil Cell (DAC), more than half a century ago,<sup>32</sup> with its versatile design and ability to reach extremely high pressures (even beyond the pressure region at which most organic solids break down), has revolutionised high pressure crystallography. A key feature is its simple mechanism of action and the fact that the cell can be mounted directly onto a conventional diffractometer (*vide infra*).<sup>33, 34</sup>

### *Facilities*

Many diffraction studies under extreme conditions require a visit to central facilities because of the specialist nature of the apparatus, and its cost. There are a number

of such facilities available around the world. The Diamond Light Source synchrotron facility in the UK, for instance, offers DACs for use on the single crystal beam line I19. Both the ESRF (France) and Spring8 (Japan) have dedicated high pressure beam lines for powder diffraction, ID27 and BL10XU respectively. Many neutron source facilities also offer various routes to extreme conditions. ISIS UK, ILL in Grenoble, France, ANSTO in Australia and Oak Ridge Spallation Neutron Source in the USA collectively offer a range of cryostats, closed cycle refrigerators and other specialist cryogenics, providing access to a range of temperatures. In the case of the Oxford Instruments KelvinoxVT Dilution Refrigerator Insert at ISIS, temperatures as low as 25 mK can be achieved. High pressure neutron studies are less common because of the larger sample size required, however most facilities offer a range of pressure cells for use on their beamlines.

Certain specialist university diffraction laboratories offer access to instrumentation designed for both HP and LT studies.<sup>35</sup> At the Centre for Science at Extreme Conditions based in Edinburgh University, there is a Bruker APEX-II diffractometer complete with Helix He-flow refrigerator capable of taking samples as low as 20 K. For extreme LT work, Copley *et al.* at Durham University developed a four circle single crystal diffractometer for temperatures down to 9 K. This machine consisted of a rotating anode generator, Huber goniometer, Siemens fast scintillations detector and APD '202' Displex cryogenic refrigerator.<sup>36</sup> Several years later Probert *et al.* carried out a rebuild of this system, taking advantage of the more recent

developments in equipment rather than altering the existing diffractometer.<sup>35</sup> The LT machine, XIPHOS I, consists of a Mo rotating anode generator with Helios focusing optics, producing a 120  $\mu\text{m}$  beam size at the sample position. A four circle Huber goniometer allows accurate positioning and a modified  $^4\text{He}$  ILL Joule-Thomson Cryostat permits temperatures as low as 1.9 K to be achieved. It is equipped with a Bruker APEXII CCD area detector. The equivalent machine for high pressure studies, XIPHOS II (Figure 1-4) consists of a four-circle Bruker diffractometer with Ag-K $\alpha$   $1\mu\text{S}$  generator with multi-layer focusing optics. Diamond anvil cells (see section 1.2.1 ) can be mounted directly onto the diffractometer once attached to a goniometer head.

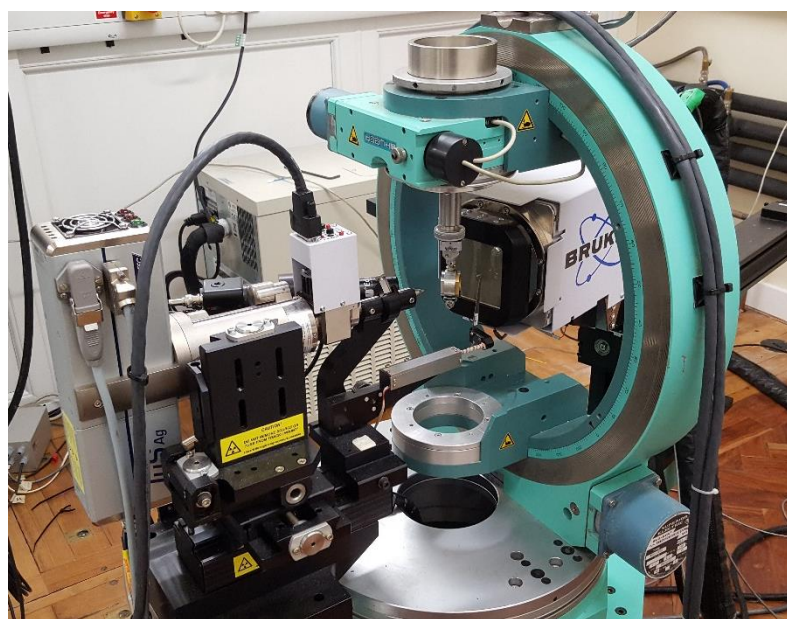


Figure 1-4. XIPHOS II diffractometer for high pressure diffraction, with DAC.

### 1.2.1 High pressure crystallography techniques

#### *The Diamond Anvil Cell*

High pressure single crystal X-ray crystallography is an expanding area of interest, due in large part to the accessibility of pressures on the order of hundreds of GPa provided by the DAC (Figure 1-5). There is also considerable current interest in the structure of porous materials under much more modest pressures of sorbed gases.<sup>37</sup> The distant ancestor of today's high pressure cells was designed by Bridgman,<sup>38</sup> who used an opposing anvil system initially of chrome steel, and subsequently tungsten carbide cemented in cobalt when the original system proved too brittle.<sup>39</sup> A gasket was used to immobilise the sample under investigation. All of the concepts underlying modern opposing anvil equipment were present, but the leap to opposed anvil diamond cells was not made until 1959, by Jamieson.<sup>33</sup> The general set-up of the diamond anvil cell is shown in Figure 1-5. The cell anvils consist of two diamonds, the advantages of which are the low absorption of short wavelength X-rays and transparency to UV, visible and IR radiation as well as the obvious hardness of diamond, allowing the DAC to reach considerable pressures. The first diamonds used in DACs were those confiscated from smugglers by customs agents and donated to research, but the diamonds used these days are rather less exciting synthetic stones.<sup>40</sup>

The diamonds are held in place by a support of brass, steel or tungsten carbide. The sample sits in a small precision drilled hole in a gasket between the culets of the diamonds, with a hydrostatic medium such as paraffin oil or a methanol/ethanol mixture added to ensure isotropic compression. In the sample holder there is also a ruby (5-10  $\mu\text{m}$ ), which allows the pressure inside the cell to be measured (*vide infra*).

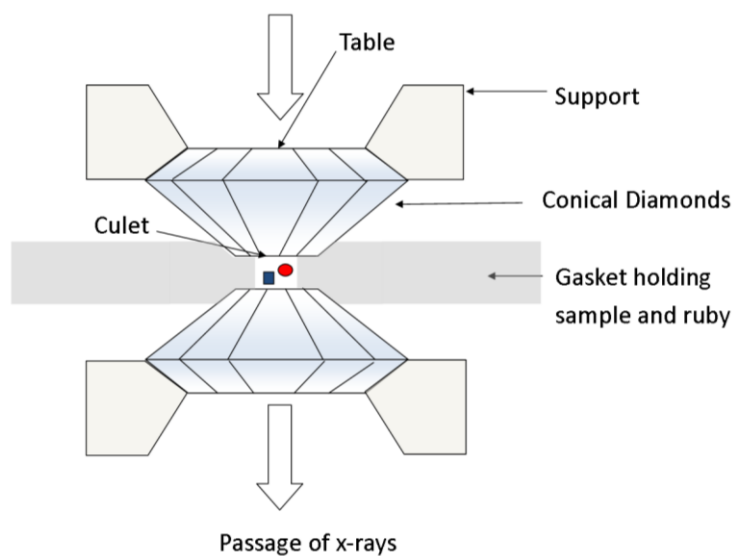


Figure 1-5. Diamond Anvil Cell. (Top) An open DAC. (Bottom) Components within the DAC.



There are some significant advantages that come with the use of the DAC; high pressures can be achieved, as force is applied over a small area, and the sample can be mounted easily on a normal goniometer due to its compact size. However, there are some limitations to this set-up. The most significant problem is obstruction of the X-ray beam by the support, which limits the range of diffraction angles that may be accessed around the crystal. A partial solution is to use a silver X-ray source instead of the more conventional copper and molybdenum sources. While beam intensity is reduced, more data can be collected within the limited diffraction angle around the crystal, as the smaller wavelength (0.56 Å, compared with around 1.54 and 0.71 Å for copper and molybdenum, respectively) means that a greater volume of reciprocal space is accessible as the radius of the limiting sphere is equal to  $2/\lambda$ . Silver X-ray sources have the additional advantage that the radiation produced is less strongly absorbed by the diamonds of the DAC.

Other disadvantages of DACs include restrictions on the size of the crystal which can be used and the indirect way the pressure has to be measured. The pressure cannot be monitored directly as it is applied, but requires a trial-and-error process to achieve the desired pressure range, particularly when a mechanical screw system is used (Figure 1-5), although more control may be obtained by use of a gas membrane driven application of pressure. Dawson summarised the problems with data processing caused by DAC collection in 2004.<sup>41</sup> The diffraction pattern of the crystal under study may contain strong reflections from the diamonds, and

scattering from the beryllium backing discs which are used in some versions of the DAC. Some frames may need to be removed from the data set where the detector has been obscured by the body of the DAC, necessitating a manipulation known as dynamic masking.<sup>41</sup> Masking is a correction method applied to shaded areas of the detector such as those created by the beam stop. The beam stop however, does not move relative to the detector, whereas the DAC does, meaning that not one, but a series of masks is needed to account for the various orientations the cell adopts relative to the detector during data collection. This is done using the program ECLIPSE.<sup>42</sup>

There are a number of absorption and systematic errors which occur when using DACs due to variation of the beam path through the diamonds and shading by the gasket hole. Although acceptable correction can be achieved using only the multi-scan method, as in the program *SADABS*,<sup>43</sup> better data can be gained from a combination of multi-scan and other methods. For example the program *Absorb6.0* applies absorption corrections by modelling the absorption profile of the body of the cell and taking into account gasket shadowing and absorption by the pressure media used in the DAC.<sup>44</sup> In addition, one effect which must be dealt with at the integration stage of data processing is the drop in reflection intensity which may be seen in the incident or diffracted beam when the diamond anvils diffract at the same Bragg angle as the crystal. These 'diamond dips' can be identified and the

affected reflections on the same frame may be scaled appropriately in order to achieve a sensible integration.

One variation on the DAC involves a miniature diamond anvil cell created at the Centre for Science at Extreme Conditions, at Edinburgh University.<sup>45</sup> This is a 'split-cylinder' design, based on the original Merrill-Bassett cell,<sup>46</sup> and is designed specifically to work with a  $^3\text{He}$  platform for use in a physical property measurement system (PPMS). The PPMS is designed to have variety of inserts and operates based on a superconductive cryomagnet, allowing measurement of properties such as electrical resistivity and magnetic susceptibility. The miniature diamond anvil cell in combination with a  $^3\text{He}$  insert allows measurements to be obtained up to 10 GPa and down to 0.35 K.

More recently, a version of the DAC was developed which employs a secondary anvil system in the form of two nanocrystalline diamond (NCD) hemispheres mounted directly on to the culets of the primary diamond anvils, allowing pressures above 600 GPa.<sup>47</sup> These NCD micro-spheres are produced by conversion of 20-50  $\mu\text{m}$  carbon glass spheres into NCD using 20 GPa of pressure and a temperature of 2,200 K with a multi-anvil press. Alterations in the synthetic conditions such as pressure media can offer a mixture of forms of NCD, such as spheres and hemispheres of various shapes. Compression of a NCD sphere (coated with a gold film to reduce luminescence) in a typical DAC with a rhenium gasket and neon as

the pressure medium was used to test the yield strength of the spheres. The pressure directly above the sphere, close to the culet of the primary diamonds, was measured using Raman spectroscopy of the diamond and the ruby fluorescence method was used to measure the pressure around the sphere in the gasket hole. These two values remain the same until the sphere starts bridging between the primary diamonds (as the gasket thickness reduces with increasing pressure) at which point the pressure at the contact point rapidly increases, with a maximum of 97 GPa at the diamond contact and a corresponding pressure of 41 GPa in the chamber as measured by the ruby chip. The yield stress was subsequently calculated at 144-168 GPa, which is comparable to similar values for single crystal diamond. After confirming that the yield strength and brittleness of the NCD spheres are appropriate, hemispheres were then mounted onto a set of primary diamond anvils as second-stage anvils. The hemispheres must be situated in small cavities carved into the diamond culets by pulsed laser or they will be susceptible to movement on application of pressure, overriding the alignment and affecting the sample environment. Disadvantages to this system are principally due to movement of the secondary anvils out of alignment, which can occur when a cavity is not carved into the primary diamonds, when the NCD hemispheres bridge the primary diamonds at pressures lower than 30-35 GPa (the gasket is too thin) and when the sample is larger than the contact area between the hemispheres.

There are also variations on the DAC in which the cell is miniaturised to achieve higher pressures.<sup>48</sup> However, the standard DAC remains the most commonly used setup for very high pressure work due to its relative simplicity and the considerable pressure range which can be achieved safely.

### *Details of the DAC*

There are several considerations to take into account when selecting or constructing a diamond anvil cell for use:

- The type of diamond
- The shape and size of the diamond.
- The gasket
- Sample hole diameter
- Hydrostatic media
- Pressure determination

### *Diamond type*

Diamond quality classification is based on the type of impurities present and the structural form of these impurities. Type I diamonds for example are the most common yellow diamonds which contain nitrogen impurities.<sup>49</sup> This is sub-categorised into IA, where the impurities are clustered within the carbon structure, and IB where the nitrogen atoms become diffused throughout.<sup>49, 50</sup> Type II white diamonds contain no nitrogen impurities and have lower absorption in the infrared region, but are much more expensive due to their rarity. As a result, low-

birefringence Type IA diamonds are the most common anvils and most readily available.

### *Size and shape*

One of the first choices when selecting diamonds for anvils is the cut and size of the diamond. Brilliant cut diamonds are prevalent as this the typical diamond cut used for gemstones and they are therefore readily available. Other designs are also obtainable such as the Drukker Dubbldee design which has a greater table size relative to the culet size (see Figure 1-5).<sup>50</sup> The shape of the diamond can impact the pressure range accessible, for example the more faces cut into the diamond, the greater stresses it can withstand.

The standard measurement for diamond size is the carat, which is defined as  $\frac{1}{5}$ <sup>th</sup> of a gram. Diamonds for anvils tend to be of the order of  $\frac{1}{3}$  or  $\frac{1}{4}$  carat as diamonds any larger than this are more likely to contain flaws which will be exacerbated under pressure and cause the diamond to crack and no longer be functional as an anvil. There are a range of culet sizes available, and those between 0.5 and 1 mm are typical. The smaller the culet size the greater the pressure that can be obtained.

### *The gasket*

The choice of material for the gasket is largely a question of experimenter preference, although some materials are naturally more compressible than others.

Stainless steel is a popular choice, with rhenium being another more expensive option. The best way to obtain a functional gasket is to purchase sheets thicker than intended for the experiment, and then pre-indent each gasket to the thickness required, before drilling the sample hole.<sup>51</sup> The section of gasket around the sample hole, and the diamonds, are then better supported by the thicker material around the hole. The degree of pre-indentation is important to the success of the experiment; all gaskets will deform by extrusion of the sample hole during an experiment, but the initial thickness of the gasket determines whether this extrusion will be inwards or outwards. If the gasket is thin enough, extrusion occurs inwards, the sample hole becomes smaller, the pressure in the sample chamber increases easily and the hole and diamonds are well supported. In the opposite case, when the gasket is too thick, the sample hole extrudes outwards and becomes larger, the diamonds must be advanced further onto the sample to achieve the same pressure and there is less support from the gasket to the sample chamber. Ideally therefore, the gasket should be pre-indented using close to that pressure which will be applied during the experiment so that it is thin enough around the sample hole.

#### *Sample hole diameter*

Ideally, the sample hole radius will be smaller than half of the indentation size, otherwise as the gasket deforms on increasing pressure, the pre-indented material

around the sample hole does not adequately support the extruding edge of the hole and the pressure within the sample hole will increase less than expected for the force applied to the DAC by the operator. For a more detailed explanation of this effect, see the theoretical discussion by Dunstan.<sup>51</sup> The size of the crystal to be used as well as the culet size of the diamonds must also be taken into account. For poorly diffracting materials, larger crystals will be needed for diffraction, which requires a larger gasket hole and consequently, diamonds with a larger culet size must be used to apply adequate pressure.

For the experiments described in this thesis stainless steel discs of 0.25 mm thickness and 9 mm diameter were used to create the gaskets. The DAC was used to pre-indent the gasket to approximately 0.15 mm. A 300  $\mu\text{m}$  hole is drilled in the centre of the indent using spark erosion (Figure 1-6).





Figure 1-6. BETSA the spark eroder.

### *Hydrostatic media*

In order to obtain a hydrostatically pressurised environment in the sample chamber, an appropriate liquid or gas medium must be chosen, taking into account the properties of the crystalline sample under study and the pressure range of the experiment. A liquid medium such as a 4:1 methanol-ethanol mixture is the most common and is simple to use.<sup>52</sup> However, if the sample is soluble in either solvent, or the desired pressure is above 10 GPa (the hydrostatic limit of this mixture) another system must be used. In some cases where more stringent conditions for a

hydrostatic medium must be met, gases such as argon or nitrogen can be used. There are two methods of gas loading into DACs, a cryogenic method and a high pressure method. Cryogenic loading requires the DAC to be partially submerged in a cryogen such as liquid nitrogen, which is used to liquefy the gas to be loaded. The DAC is sealed under the liquefied gas, trapping a portion of it in the sample chamber. The alternative high pressure method uses a gas compressor to increase the gas density at ambient temperature which can then be trapped in the DAC by sealing the sample chamber. Table 1-3 outlines some of the popular choices for hydrostatic media and their limits.<sup>52-54</sup> These values were collected from several publications which use the line widths from ruby fluorescence or diffraction maxima from quartz single crystals to determine the hydrostatic limit.<sup>52</sup>

**Table 1-3. Limits of hydrostatic media.** <sup>52-54</sup>

Medium	Hydrostatic limit (GPa)
4:1 Methanol -ethanol	9.8
2-propanol	4.2
Argon	1.9
Nitrogen	3.0
Glycerol	1.4
Silicone oil	0.9
1:1 Pentane-isopentane	7.0
Helium	23
Paraffin oil	3.0

### Experimental Pressure Measurement

The internal pressure of a DAC can be measured by the ruby  $R_1$  fluorescence method, initially developed by Forman *et al.* in 1972.<sup>55</sup> Rubies fluoresce with a doublet of lines at 692.7 and 694.2 nm at atmospheric pressure. Under pressure, these lines shift linearly to higher wavelength, providing an internal gauge by which the pressure in the cell can be determined.

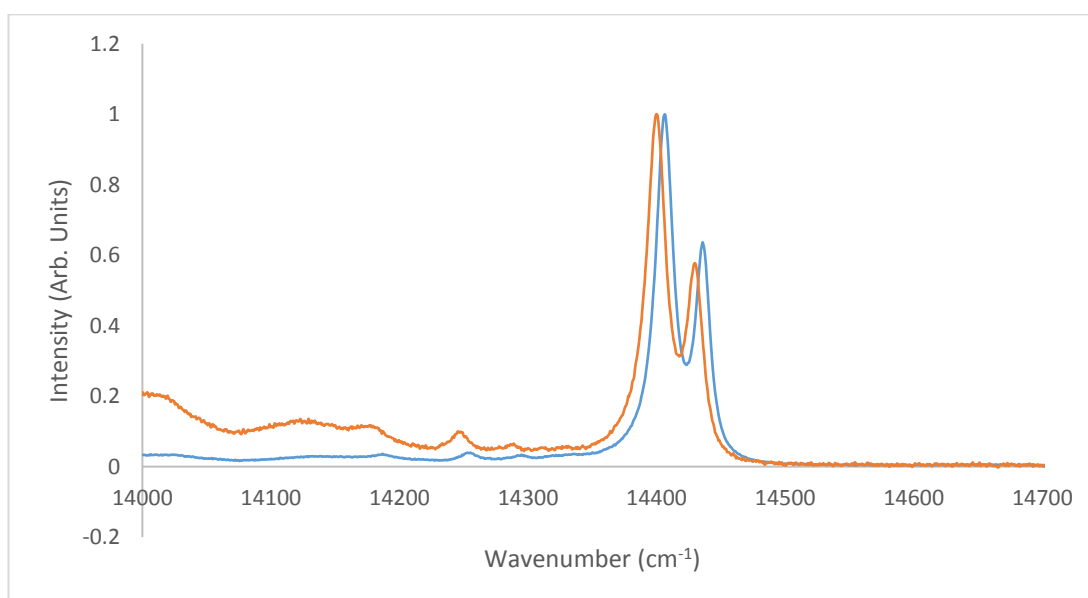


Figure 1-7. Ruby fluorescence at high pressure (orange) and ambient pressure (blue).

While ruby is a common choice to provide a route to measurement of the pressure within the DAC, other internal standards such as quartz or sodium chloride may be used provided their equations of state are well known in order to convert the measured unit cell parameters into the corresponding pressures. Any such internal standards are most effective if they are inert in the atmosphere and the chosen

hydrostatic medium, and the standard should have a low unit cell volume with high symmetry.<sup>56</sup>

### 1.2.2 Low temperature crystallography

Low-temperature X-ray crystallography techniques were developed for the purpose of minimising radiation damage to single crystal specimens as well as reducing thermal motion within the crystal lattice.<sup>34</sup> LT conditions reduce interference caused by thermal diffuse scattering within the crystal. Now, with temperatures approaching absolute zero becoming attainable, LT crystallography may provide access to a new realm of structural investigation, allowing temperature-dependent properties to be probed in unprecedented detail.

#### *Open Flow Gas Cryostats*

##### *Nitrogen based cryostats*

Open flow nitrogen gas cryostats (OFNCs) are the standard instrumentation for single crystal diffractometers in most modern crystallography laboratories. An ONFC can produce temperatures as low as 80 K, but operating temperatures in the range 120-150 K are typical.<sup>35</sup> The major advantage of open flow cryostats is that they do not require a closed system in order to cool a sample effectively, so the crystal can be accessed easily. However, in older versions of these cryostats, it is difficult to precisely maintain the temperature of the sample. The general set up of a modern OFNC overcomes this issue and is detailed in Figure 1-8.<sup>57</sup>

Liquid nitrogen is drawn directly from the unpressurised Dewar vessel (a), through a vacuum-insulated pipe (b). The liquid flows into a high vacuum insulated chamber where it passes through a heating coil (c) and heat exchanger, resulting in vaporisation. Flowing out of the chamber, the gas flow passes through a needle valve (d) which regulates the gas flow rate, and arrives at the diaphragm pump (e) and flow meter (f). The gas is re-cooled as it passes through the other side of the heat exchanger. It then passes over a second heating coil (g) and thermal sensor (h) before arriving at the sample.

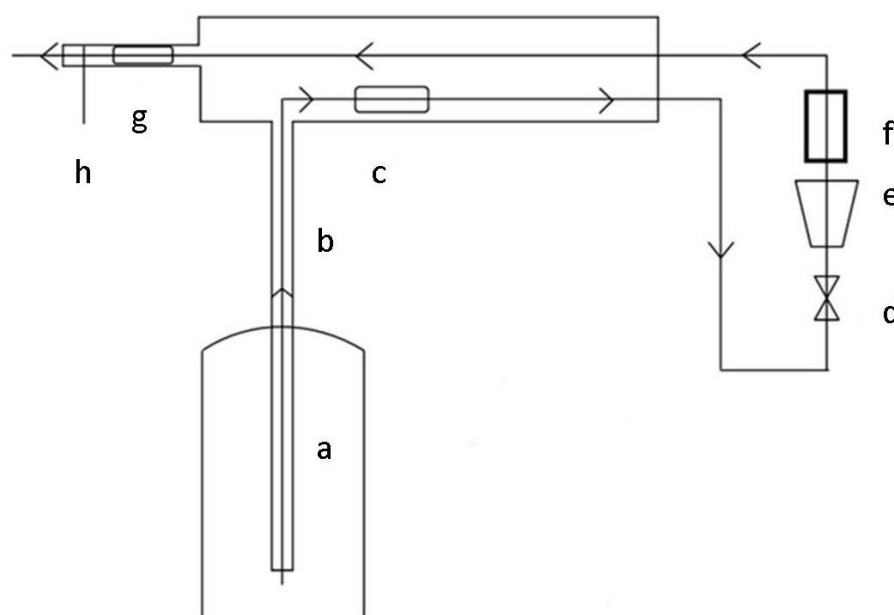


Figure 1-8. Open flow nitrogen gas cryostat.<sup>53</sup>

### *Helium based cryostat*

Following the development of the OFNC, a cooling system based on helium represents a natural progression. Open flow helium gas cryostats (OFHCs), such as the N-Helix systems (available from Oxford Cryosystems), can deliver significantly lower operating temperatures and are the preferred cooling method for high-accuracy LT structure determination below 80 K.<sup>58</sup>

One of the first OFHCs, designed by Moffat and co-workers, was a custom built two-part setup which allows the experimenter to switch between using nitrogen or helium gas depending on the desired temperature (80 K for nitrogen, 10-70 K for helium).<sup>59</sup> In an attempt to improve the accessibility of helium cryostats, Hardie and co-workers described the assembly of an open flow system from an ESR helium cryostat and other, readily available components.<sup>60</sup> Both the Moffat and Hardie systems can be used in diffraction studies without limiting the visibility or accessibility of the crystal during alignment and data collection. However, the use of OFHCs in LT crystallography has so far been limited, due to their rapid consumption of an expensive cryogen. In the Hardie system, cooling to 20 K requires a helium flow of 4 Lh<sup>-1</sup>, and cooling to 14 K demands greater volumes still. Although these consumption rates are an improvement to those achieved by the Moffat group, they are still too large for helium-cooling to be widely adopted in the crystallographic community. One successful application by the Howard and Yaghi

groups used a Helix OFHC to cool MOFs to temperatures between 30 and 293 K, showing that the occupancy of argon and nitrogen gas sites within the MOF structure is temperature dependent.<sup>61</sup>

Closed cycle refrigerators (CCRs) require a much smaller volume of helium gas, as they operate by compression, expansion and recycling of the gas, which in turn is in thermal contact with the sample.<sup>34</sup> One such system, the closed-cycle two-stage helium refrigerator, allows cooling to temperatures as low as 9 K.<sup>36</sup> A common disadvantage of CCRs is that the crystal must be housed in a shroud, resulting in significant background scattering and no possibility of viewing the sample once enclosed. This shroud is commonly composed of beryllium but in the case of neutron systems, aluminium is used.

Similar to data integration from DAC X-ray studies, CCRs necessitate the generation of masks due to the scattering from the beryllium shrouds. Although beryllium is largely transparent to X-rays, the effect is significant enough that a program is required to calculate the appropriate masks. Such a program is '*Masquerade*' which uses the known position of the shrouds and the simulated diffraction pattern of beryllium to determine where scattering from beryllium will occur on the overall diffraction pattern, and the appropriate corrections are made.<sup>62</sup>

### 1.3 Neutron diffraction

Neutron radiation from a nuclear reactor or spallation source offers a complementary technique to X-ray diffraction. Neutrons are a form of particulate radiation which can have wavelengths comparable to X-rays and the distances of interatomic spacing.<sup>63</sup>

Many of the same diffraction principles apply as to X-ray diffraction, with the essential difference being the nature of the interaction between the radiation type and atoms.<sup>64, 65</sup> X-rays are scattered by electrons and the diffraction experiment offers information about the electron density distribution within a structure, and the associated scattering factor is directly proportional to atomic number. Neutrons are scattered by the nuclei of atoms, show no discernible trend in scattering factor and may scatter in or out of phase, giving rise to a positive or negative scattering factor, respectively. Isotopes of an atom may have different scattering factors; as a result hydrogen and deuterium, among other isotopes, can be distinguished where isotope labelling has been utilised (Figure 1-9). Additionally, certain atoms which are close to indistinguishable from each other by X-ray diffraction may be more easily identified by neutron scattering experiments.



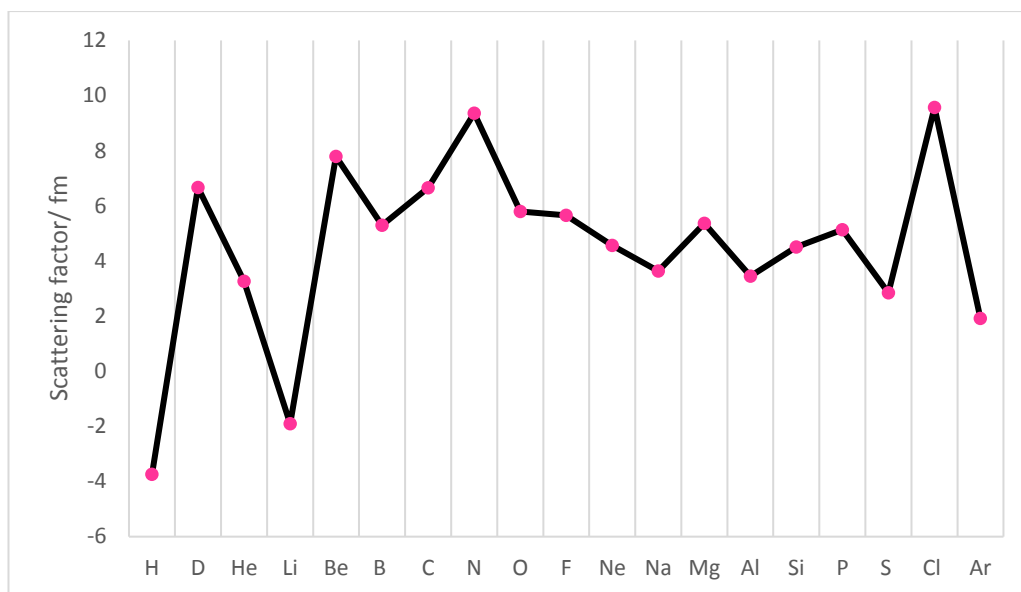


Figure 1-9. Scattering factors for neutron diffraction.

Due to the relatively low diffraction intensity of neutron radiation, absorption and radiation damage are minimised compared to X-ray diffraction. However this means significantly larger crystals are required, which can be difficult to obtain. Neutrons are highly penetrating despite the relatively weak beams currently available from neutron sources and can be mono- or polychromatic.

An example of the advantage of neutron diffraction studies in investigating the detailed structure of hydrogen bonded systems is given in the co-crystals of benzene-1,2,4,5-tetracarboxylic acid (BTA) and 4,4'-bipyridine (BPY).<sup>66, 67</sup> It was found that in the 1:2 co-crystal of BTA and BPY, temperature dependent hydrogen atom migration occurs between the short N...O hydrogen bond between the molecules. At 20 K, the proton is closer to the nitrogen atom of BPY but as the temperature increases to 300 K, it migrates gradually until it is closer to the oxygen

atom of BTA. Such subtle but significant effects in bonding could never be elucidated without neutron diffraction.

#### 1.4 Raman Spectroscopy

Raman spectroscopy is a versatile technique which uses monochromatic radiation to probe the vibrational (phonon) states of a molecule.<sup>68</sup> It is complementary to IR spectroscopy but differs in that it measures the symmetric vibrations of non-polar groups; the electromagnetic radiation produced by oscillating dipoles which are induced by irradiation of a sample. This is dependent on the polarizability of the molecule and in the case of Raman spectroscopy, is most effective on compounds which do not have a centre of symmetry within the molecule.

As Raman spectroscopy measures scattered light from a sample, it requires very little sample preparation. Solids, liquids, gases and crystals can all be investigated by the technique, including those contained in any transparent sample holder such as a glass vial, or a DAC.

When a molecule is irradiated with light it enters a virtual excitation state and can undergo one of three potential mechanisms, shown in Figure 1-10:

1. Rayleigh scattering; the molecule emits the same energy it acquired in an inelastic process.
2. Stokes; the molecule emits at a higher wavelength and relaxes to an excited state higher than that of the ground state.

3. Anti-Stokes; the molecule was already in an excited state before irradiation, and the emitted photon is of lower wavelength than the incident light.

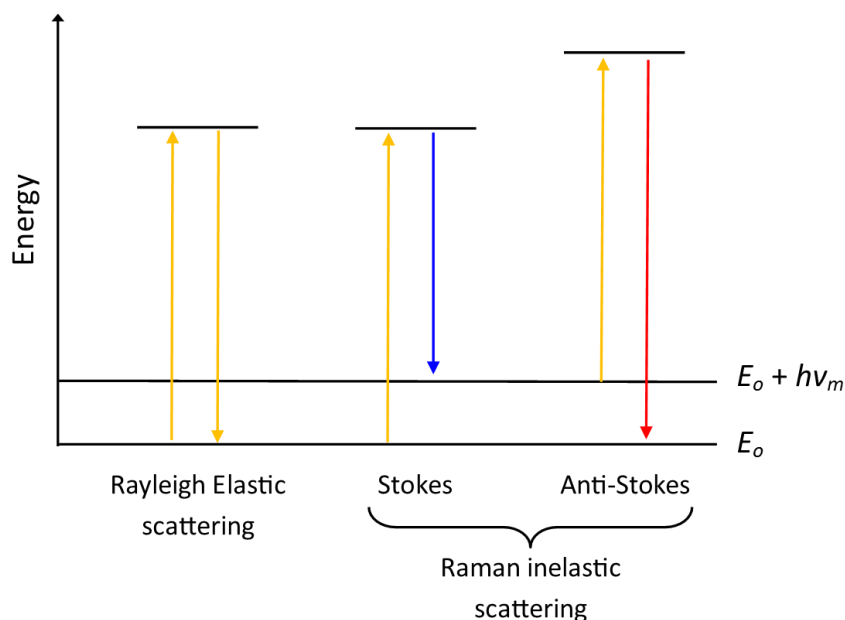


Figure 1-10. Energy levels and emissions involved in Raman scattering.

## 1.5 References

1. D. Shechtman, I. Blech, D. Gratias and J. W. Cahn, *Phys. Rev. Lett.*, 1984, **53**, 1951-1953.
2. P. M. de Wolff, *Acta Crystallogr. Sect A*, 1974, **30**, 777-785.
3. W. L. Bragg, *P. Roy. Soc. Lond. A Mat.* 1913, **89**, 248-277.
4. K. A. Kerr and J. P. Ashmore, *Acta Crystallogr. Sect A*, 1974, **30**, 176-179.
5. *SADABS*, Bruker AXS Inc.: Madison, WI, 2001.
6. G. Sheldrick, *Acta Crystallogr. Sect C*, 2015, **71**, 3-8.
7. A. Caron and J. Donohue, *Acta Crystallogr.*, 1965, **18**, 562-565.
8. B. D. Sharma, *J. Chem. Educ.*, 1987, **64**, 404.
9. W. I. Higuchi, P. K. Lau, T. Higuchi and J. W. Shell, *J. Pharm. Sci.*, 1963, **52**, 150-153.
10. K. Raza, P. Kumar, S. Ratan, R. Malik and S. Arora, *SOJ Pharmacy and Pharmaceutical Science*, 2014, **1**.
11. D. P. Elder, J. E. Patterson and R. Holm, *J. Pharm. Pharmacol.*, 2015, **67**, 757-772.
12. J. D. Dunitz and J. Bernstein, *Acc. Chem. Res.*, 1995, **28**, 193-200.
13. S. Price, *Acta Crystallogr., Sect. B: Struct. Sci.*, 2013, **69**, 313-328.
14. R. Lee, J. A. K. Howard, M. R. Probert and J. W. Steed, *Chem. Soc. Rev.*, 2014, **43**, 4300-4311.
15. E. Boldyreva, *Acta Crystallographica Section A*, 2008, **64**, 218-231.

16. V. F. Petrenko and R. W. Whitworth, *Physics of Ice*, Clarendon Press, 1999.
17. D. R. Allan, S. J. Clark, R. M. Ibberson, S. Parsons, C. R. Pulham and L. Sawyer, *Chem. Commun.*, 1999, DOI: 10.1039/A900558G, 751-752.
18. R. Fourme, D. Andre and M. Renaud, *Acta Crystallogr., Sect. B: Struct. Sci.*, 1971, **27**, 1275-1276.
19. M. R. Probert, Y. H. P. Chung and J. A. K. Howard, *CrystEngComm*, 2010, **12**, 2584-2586.
20. V. S. Minkov, N. A. Tumanov, R. Q. Cabrera and E. V. Boldyreva, *CrystEngComm*, 2010, **12**, 2551-2560.
21. S. A. Moggach, S. Parsons and P. A. Wood, *Crystallogr. Rev.*, 2008, **14**, 143-184.
22. A. V. Kazantsev, P. G. Karamertzanis, C. S. Adjiman, C. C. Pantelides, S. L. Price, P. T. A. Galek, G. M. Day and A. J. Cruz-Cabeza, *Int. J. Pharm.*, 2011, **418**, 168-178.
23. G. M. Day, W. D. S. Motherwell, H. L. Ammon, S. X. M. Boerrigter, R. G. Della Valle, E. Venuti, A. Dzyabchenko, J. D. Dunitz, B. Schweizer, B. P. van Eijck, P. Erk, J. C. Facelli, V. E. Bazterra, M. B. Ferraro, D. W. M. Hofmann, F. J. J. Leusen, C. Liang, C. C. Pantelides, P. G. Karamertzanis, S. L. Price, T. C. Lewis, H. Nowell, A. Torrisi, H. A. Scheraga, Y. A. Arnautova, M. U. Schmidt and P. Verwer, *Acta Crystallogr., Sect. B: Struct. Sci.*, 2005, **61**, 511-527.
24. J. P. M. Lommerse, W. D. S. Motherwell, H. L. Ammon, J. D. Dunitz, A. Gavezzotti, D. W. M. Hofmann, F. J. J. Leusen, W. T. M. Mooij, S. L. Price, B. Schweizer, M. U. Schmidt, B. P. van Eijck, P. Verwer and D. E. Williams, *Acta Crystallogr., Sect. B: Struct. Sci.*, 2000, **56**, 697-714.
25. W. D. S. Motherwell, H. L. Ammon, J. D. Dunitz, A. Dzyabchenko, P. Erk, A. Gavezzotti, D. W. M. Hofmann, F. J. J. Leusen, J. P. M. Lommerse, W. T. M. Mooij, S. L. Price, H. Scheraga, B. Schweizer, M. U. Schmidt, B. P. van Eijck, P. Verwer and D. E. Williams, *Acta Crystallogr., Sect. B: Struct. Sci.*, 2002, **58**, 647-661.
26. J. Ridout, L. S. Price, J. A. K. Howard and M. R. Probert, *Cryst. Growth Des.*, 2014, **14**, 3384-3391.
27. I. D. H. Oswald, D. R. Allan, G. M. Day, W. D. S. Motherwell and S. Parsons, *Cryst. Growth Des.*, 2005, **5**, 1055-1071.
28. M. A. Neumann, J. van de Streek, F. P. A. Fabbiani, P. Hidber and O. Grassmann, *Nat Commun*, 2015, **6**.
29. J. Ridout and M. R. Probert, *Cryst. Growth Des.*, 2013, **13**, 1943-1948.
30. K. Fucke, N. Qureshi, D. S. Yufit, J. A. K. Howard and J. W. Steed, *Cryst. Growth Des.*, 2010, **10**, 880-886.
31. R. Boehler, *Nature*, 1993, **363**, 534-536.
32. W. A. Bassett, *High Pressure Research*, 2009, **29**.
3. J. C. Jamieson, A. W. Lawson and N. D. Nachtrieb, *Rev. Sci. Instrum.*, 1959, **30**, 1016-1019.
34. A. E. Goeta and J. A. K. Howard, *Chem. Soc. Rev.*, 2004, **33**, 490-500.
35. M. R. Probert, C. M. Robertson, J. A. Coome, J. A. K. Howard, B. C. Michell and A. E. Goeta, *J. Appl. Crystallogr.*, 2010, **43**, 1415-1418.
36. R. C. B. Copley, A. E. Goeta, C. W. Lehmann, J. C. Cole, D. S. Yufit, J. A. K. Howard and J. M. Archer, *J. Appl. Crystallogr.*, 1997, **30**, 413-417.
37. T. Jacobs, G. O. Lloyd, J.-A. Gertenbach, K. K. Müller-Nedebock, C. Esterhuysen and L. J. Barbour, *Angew. Chem. Int. Ed.*, 2012, **51**, 4913-4916.

38. R. J. Hemley, *High Pressure Research*, 2010, **30**.
39. P. W. Bridgman, *Proceedings of the Royal Society of London. Series A, Mathematical and Physical Sciences*, 1950, **203**, 1-17.
40. G. J. Piermarini, *Journal of Research of the National Institute of Standards and Technology*, 2001, **106**.
41. A. Dawson, D. R. Allan, S. Parsons and M. Ruf, *J. Appl. Crystallogr.*, 2004, **37**, 410-416.
42. S. Parsons *ECLIPSE* Edinburgh, UK, 2010.
43. G. M. Sheldrick *SADABS*, 2004/1; University of Göttingen, Germany, 2004.
44. R. Angel, *J. Appl. Crystallogr.*, 2004, **37**, 486-492.
45. K. V. Kamenev, J. Sanchez-Benitez and S. Tancharakorn, *High Pressure Research*, 2007, **27**, 189-192.
46. L. Merrill and W. A. Bassett, *Rev. Sci. Instrum.*, 1974, **45**, 290-294.
47. L. Dubrovinsky, N. Dubrovinskaia, V. B. Prakapenka and A. M. Abakumov, *Nat. Commun.*, 2012, **3**, 2160/2161-2160/2167.
48. E. Sterer, M. P. Pasternak and R. D. Taylor, *Rev. Sci. Instrum.*, 1990, **61**, 1117-1119.
49. C. M. Breeding and J. E. Shingley, *Gems & Gemology*, 2009, **45**, 15.
50. D. J. Dunstan and I. L. Spain, *J. Phys. E: Sci. Instrum.*, 1989, **22**, 913-923.
51. D. J. Dunstan, *Rev. Sci. Instrum.*, 1989, **60**, 3789-3795.
52. R. J. Angel, M. Bujak, J. Zhao, G. D. Gatta and S. D. Jacobsen, *J. Appl. Crystallogr.*, 2007, **40**, 26-32.
53. S. Klotz, J.-C. Chervin, P. Munsch and G. L. Marchand, *J. Phys. D: Appl. Phys.*, 2009, **42**, 075413.
54. G. J. Piermarini, S. Block and J. D. Barnett, *J. Appl. Phys.*, 1973, **44**, 5377-5382.
55. R. A. Forman, G. J. Piermarini, J. D. Barnett and S. Block, *Science*, 1972, **176**, 2.
56. R. J. Angel, D. R. Allan, R. Miletich and L. W. Finger, *J. Appl. Crystallogr.*, 1997, **30**, 461-466.
57. J. Cosier and A. M. Glazer, *J. Appl. Crystallogr.*, 1986, **19**, 105-107.
58. A. E. Goeta, L. K. Thompson, C. L. Sheppard, S. S. Tandon, C. W. Lehmann, J. Cosier, C. Webster and J. A. K. Howard, *Acta Crystallographica Section C*, 1999, **55**, 1243-1246.
59. T. Teng, W. Schildkamp, P. Dolmer and K. Moffat, *J. Appl. Crystallogr.*, 1994, **27**.
60. M. J. Hardie, K. Kirschbaum, A. Martin and A. A. Pinkerton, *J. Appl. Crystallogr.*, 1998, **31**, 815-817.
61. J. L. C. Rowsell, E. C. Spencer, J. Eckert, J. A. K. Howard and O. M. Yaghi, *Science*, 2005, **309**, 1350-1354.
62. J. A. Coome, A. E. Goeta, J. A. K. Howard and M. R. Probert, *J. Appl. Crystallogr.*, 2012, **45**, 292-298.
63. L. De Broglie, *Nature*, 1923, **112**, 540.
64. W. Clegg, *Crystal Structure Determination*, Oxford University Press, Incorporated, 1998.
65. J. P. Glusker and K. N. Trueblood, *Crystal Structure Analysis: A Primer*, OUP Oxford, 2010.
66. J. A. Cowan, J. A. K. Howard, S. A. Mason, G. J. McIntyre, S. M.-F. Lo, T. Mak, S. S.-Y. Chui, J. Cai, J. A. Cha and I. D. Williams, *Acta Crystallographica Section C*, 2006, **62**, o157-o161.

67. S. M. F. Lo, J. A. Cowan, J. A. K. Howard, G. J. McIntyre and I. D. Williams, *Acta Crystallogr., Sect. B: Struct. Sci.*, 2003, **59**, 794-801.
68. P. Larkin, *Infrared and raman spectroscopy principles and spectral interpretation*, Elsevier, Oxford, 2011.

## Chapter 2 Introduction to supramolecular chemistry

---

Supramolecular chemistry, as “chemistry beyond the molecule” encompasses vast and varied fields of chemistry including solution state interactions, self-assembling systems, crystal engineering, solid state host-guest assemblies and more. Although the definition of supramolecular chemistry is ever fluctuating and developing, it is always dominated by the non-covalent bond. Within supramolecular chemistry, many different bonding patterns and motifs can be identified, of which co-crystals are one and inclusion compounds are another.

### 2.1 Co-crystals

Co-crystals have long been of significant interest to the scientific community, with numerous potential applications ranging from gas storage and separation,<sup>1</sup> non-linear optical materials<sup>2</sup> and the fine tuning and control of the properties of active pharmaceutical ingredients.<sup>3</sup> The definition of what constitutes a co-crystal is under frequent scrutiny.<sup>3-5</sup> Generally, a co-crystal is a crystal containing two or more components. This definition breaks down when looking more closely at what those components are. It has been argued that any crystal containing a solvent molecule should not warrant the name co-crystal. This definition would exclude all solvates and hydrates from the class despite their being no conceptual difference between a solvate and a co-crystal containing components that have not been used as

solvents.<sup>6</sup> Additionally, a salt containing an anion-cation pair does not qualify as a co-crystal because the components cannot be separated, however the position of a proton can be dependent on conditions and hence even this boundary is sometimes difficult to accurately define for a given system.<sup>7</sup> The scope of co-crystals is also sometimes restricted to crystals formed from reactants which are solid and neutral under ambient conditions.<sup>8</sup> However, application of high pressure to a liquid mixture frequently results in a liquid-solid phase transition to give a crystalline multi-component solid and in the present work we use the term co-crystal to include all multi-component molecular crystals. Where proton transfer has occurred in acid-base mixtures, the resulting crystal will be called a salt co-crystal. Acid-base co-crystals are of particular interest to the pharmaceutical industry as many active pharmaceutical ingredients (APIs) and their co-formers have acid or base functionality. Also, many drugs are specifically designed to exist in salt form in order to achieve the desired properties.<sup>9</sup> An acid-base supramolecular heterosynthone is a good candidate for co-crystal design strategies as selection of the correct co-former allows the opportunity to formulate a drug with the desired solubility, bioavailability, compressibility and stability.<sup>10</sup> An example of this is seen in theophylline, a derivative of purine, which is used to treat asthma and as a diuretic.<sup>11</sup> When crystallised with salicylic, oxalic or glutaric acids theophylline forms hydrogen bonds between the basic nitrogen atom and the hydroxyl group of the acid. The choice of acidic co-former impacts the properties of the co-crystals,



particularly the co-crystal melting temperature in this example. Carboxylic acids are frequently used as API co-formers as the resulting acid-base heterosynthon is more robust than an acid-acid homodimer in a one component API crystals.<sup>9</sup> Bis *et al* demonstrated the favourability of heterosynthons over homosynthons in an analysis of pyridine-hydroxyl interactions in the Cambridge Structural Database.<sup>12</sup>

Many co-crystals, including those designed for pharmaceutical purposes, contain one or more components which are solids at ambient conditions, and are crystallised using a number of methods including solution, solid state grinding or solvent drop grinding methods.<sup>13</sup> However, *in situ* crystallisation techniques using temperature and pressure (see Chapter 1) allow compounds which are liquids at ambient conditions to be co-crystallised. The number of these low melting molecular co-crystals reported in the literature is remarkably low, considering the availability of *in situ* crystallisation methods such as capillary crystallisation. Despite this there are examples of low melting molecular complexes, particularly involving common solvents such as chloroform and methanol.<sup>14-17</sup>

## 2.2 Inclusion compounds

Inclusion compounds (ICs) are distinct in that they can be broken down in terms of a host and a guest; a widely developed concept since 1811 when Sir Humphrey Davy first isolated the clathrate hydrate of chlorine and water.<sup>18</sup> Of the many structural variations seen in inclusion compound chemistry, two broad sub-groups

can be identified; clathrates and channel inclusion compounds. In clathrate compounds, the host structure fully or partially encapsulates the guest molecule, a term which came into use after Powell's work in 1945 on the structure of hydroquinone (see Hydroquinone section).<sup>19</sup> Channel ICs on the other hand, form one dimensional tunnels or a network of tunnels, such as those seen in zeolites. The space created is often occupied by guest molecules. Further categorisation of ICs comes from the stability of the structure upon guest removal. Some clathrates are stable only when the guest molecules are present and in their absence, the host adopts an entirely different packing structure which is termed the  $\alpha$ -phase of that compound, the most stable polymorph. Subsequently, the complete inclusion compound is called the  $\beta_n$  phase, where n denotes different forms with variation in structure, such as unit cell parameters or space group. The  $\beta_0$  phase, if it can be obtained, is the host IC structure minus the presence of any guest.

There are many aspects to consider when discussing the structural features of inclusion compounds, not least the nature of bonding which allows their formation. Interactions such as ion-ion, ion-dipole, dipole-dipole, ion- $\pi$ ,  $\pi$ - $\pi$  all have contributions in supramolecular chemistry.<sup>20</sup> Of particular interest here are hydrogen bonds and van der Waals forces. Van der Waals interactions are ubiquitous in inclusion chemistry, as the chief interaction when organic molecules are encapsulated in a channel or cage, potentially playing a part in directing templation of the host.

### 2.2.1 Hydroquinone

Hydroquinone (Quinol) is a classic example of a molecule capable of forming clathrate inclusion compounds with small guest molecules, such as CO<sub>2</sub>, NH<sub>2</sub>, CH<sub>4</sub>, MeCN, H<sub>2</sub>S as well as the noble gases Ar, Kr and Xe.<sup>21</sup> The structure of the  $\alpha$ -phase of hydroquinone has space group  $P2_1/c$ ,<sup>22, 23</sup> whereas the  $\beta$ -phase adopts the hexagonal form  $R\bar{3}$ .<sup>24</sup> The  $\beta_0$  phase of hydroquinone can be obtained when crystallised from dry ethanol, but it will spontaneously convert to the more stable  $\alpha$ -form.<sup>25</sup> In the presence of a suitable guest which can occupy the cavity created by six hydroquinone molecules, an inclusion compound is formed (Figure 2-1).

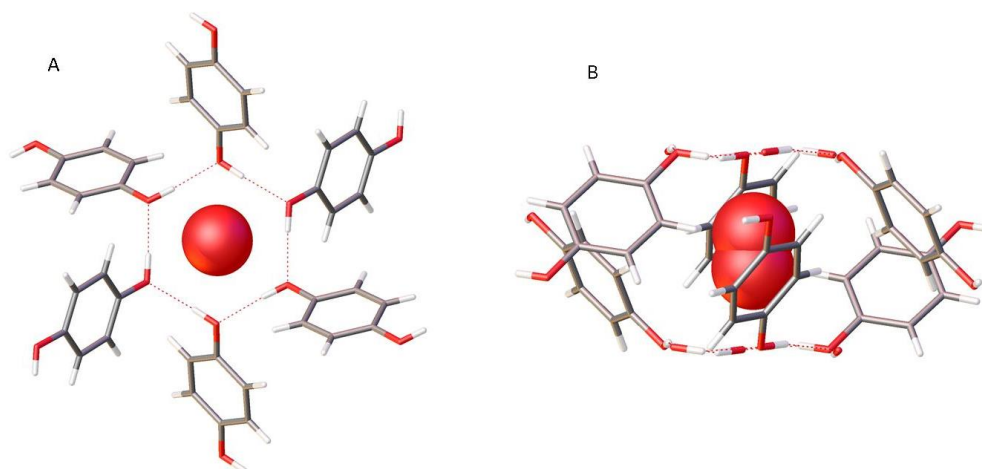


Figure 2-1.  $\beta$ -quinol inclusion compound with nitric oxide shown as space filling; A) down  $c$  cell axis, B) capsule consisting of six hydroquinone molecules and one NO. (Disordered with respect to NO).<sup>24</sup>

### 2.2.2 Calixarenes

Calixarenes, having the general structure shown in Figure 2-2, have existed since the late 19<sup>th</sup> century although this tetrameric structure was not suspected until

some decades later with the work of Zinke, simplifying the synthetic process.<sup>26</sup> It was not until the 1970s that work by Gutsche revealed that calixarenes can have higher than tetrameric structures, and up to calix[20]arenes have been isolated.<sup>27</sup> The same decade also saw the clathrating ability of calixarenes revealed with the X-ray crystal structure of *p*-tert-butylcalix[4]arene : toluene, a system which remains of interest today.<sup>28</sup>

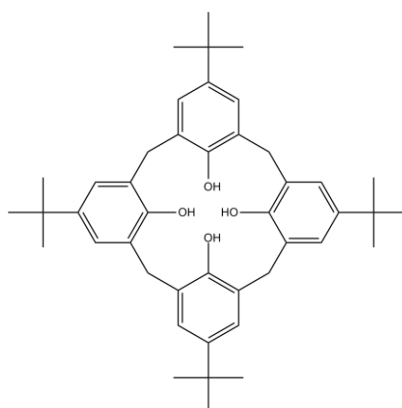


Figure 2-2. *p*-tert-butylcalix[4]arene

Calixarene systems stand apart from many other inclusion complexes as they display both solution and solid state inclusion behaviour with a variety of guests, primarily *via* Van der Waals interactions, provided the liquid medium is suitably non-interacting with either guest or host species and miscible with both.<sup>29</sup> As a host compound, calixarenes display a variety of packing arrangements and host-guest ratios. A 1:1 ratio exists between *p*-tert-butylcalix[4]arene and 1,3,5-trifluorobenzene,<sup>30</sup> however with guests *n*-butylamine<sup>31</sup> and azobenzene,<sup>32</sup> a 1:2 ratio is seen, with the calixarene hosts encapsulating the guest molecule. Even between these two examples, there is a structural difference as seen in Figure 2-3.

With *n*-butylamine (Figure 2-3B), there is axial symmetry relating the two host molecules as they form a capsule around the guest. With azobenzene (Figure 2-3), a capsule is still formed but the two calixarene molecules are offset from each other, related instead by an inversion centre through the azo-bond of the guest.

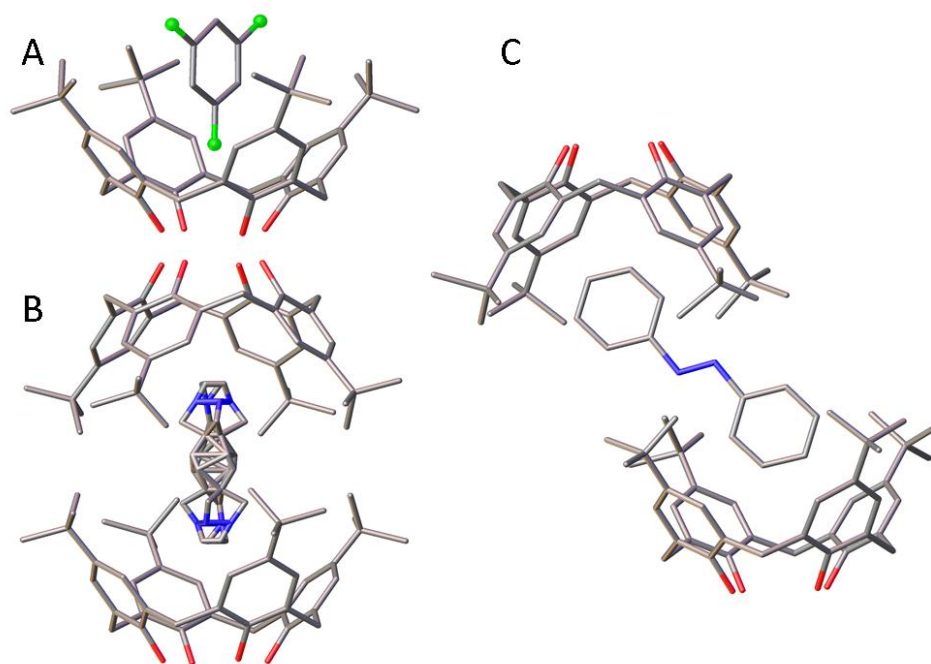


Figure 2-3. *p*-tert-butylcalix[4]arene inclusion compounds with A) 1,3,5-trifluorobenzene<sup>30</sup> B) *n*-butylamine<sup>31</sup> (disordered) and C) azobenzene guests.<sup>32</sup>

Significant work has been carried out on *p*-tert-butylcalix[4]arene (tBC) by Ripmeester *et al.*, a system which proves a versatile host for a variety of guests.<sup>32</sup> Initially this study started as an investigation into the poor refinement of structural models of tBC-toluene, which exhibits a 1:1 guest: host ratio. It was found that this assembly undergoes a structural change below 250 K, where the guest switches

from having four-fold positional disorder to two-fold symmetry, and a correlation is seen between the orientation of toluene and the distortion of the host molecule, as the change in symmetry results in a reorientation of the *tert*-butyl groups of tBC.

Atwood *et al.* reported that a crystal of tBC will undergo a single crystal-to- single crystal transition on uptake or release of vinyl bromide guest.<sup>33</sup> This uptake requires significant cooperativity within the crystal as no channels exist in the original structure, and the molecules must withstand positional or orientational rearrangement to accommodate the guest without undergoing the dissolution of one phase preceding growth of the second. This transition takes place within 15 minutes of soaking in vinyl bromide at -5°C. Both the original structure and the host-guest complex are non-porous structures, but on guest inclusion the packing motif changes from an [AB CD] bilayer system to an [ABAB] system, as the [CD] bilayer translates along the [210] direction by 5.9 Å. As a result, the *c* axis length is halved after guest inclusion.

It was found that exposing a tBC single crystal to vinyl bromide for 10 minutes results in a mixed phase crystal, which after a period of 18 hours in ambient atmosphere transforms to entirely the [ABAB] host-guest system with approximately 60% cavity occupancy.

Another application of calixarene chemistry investigated by the Atwood group is gas adsorption by a microporous system based on 1,2-di-methoxy-*p-tert*-

butylcalix[4]di-hydroquinone.<sup>34</sup> This compound crystallises in a cubic system with nanoscale channels and hydrophobic cages which are occupied by water molecules. Removal of the water leaves the cage structure intact, and subsequently the cages can be filled with small gas molecules such as CO<sub>2</sub>, for which this system shows high selectivity over H<sub>2</sub> gas at ambient temperature.<sup>35</sup> 0.29 wt% of methane is adsorbed at ambient conditions, rising to 5 wt% when the system is cooled to 203 K and pressurised at 3 atm of methane. Further gases tested with system are acetylene and argon.<sup>36</sup> In the case of acetylene, uptake is higher than for both carbon dioxide and hydrogen gases, although this also shows improved guest uptake at lower temperature and elevated pressure. Argon shows a three stage enthalpy of adsorption profile which was interpreted as initial arrangement of argon molecules in the polar channels, followed by filling of the channels with further gas molecules and finally adsorption on the external surface of the structure.

### 2.2.3 Urea

The characteristic of urea which allows it to have such rich supramolecular chemistry is the strength and extent of hydrogen bonding it can be involved in. Urea adopts two main structural types; in crystals of pure urea,  $\alpha$ -urea, this is an  $\alpha$ -tape motif shown in Figure 2-4. Each molecule is donating four hydrogen bonds *via* the N-H groups and accepting four hydrogen bonds *via* the carbonyl group.<sup>37</sup> There are two unique hydrogen bonds in urea highlighted in Figure 2-4A, with bond lengths 2.994(6)(i) and 3.034(5)(ii) Å. The typical bond energy for a hydrogen bond

in a urea  $\alpha$ -tape is  $44.80 \text{ kJmol}^{-1}$ .<sup>38, 39</sup> These hydrogen bonds can be classified as moderate in strength based on bond energy and length.<sup>20</sup> The second bonding type urea adopts, the  $\beta$ -phase, is that of urea inclusion compounds (see Chapter 3).

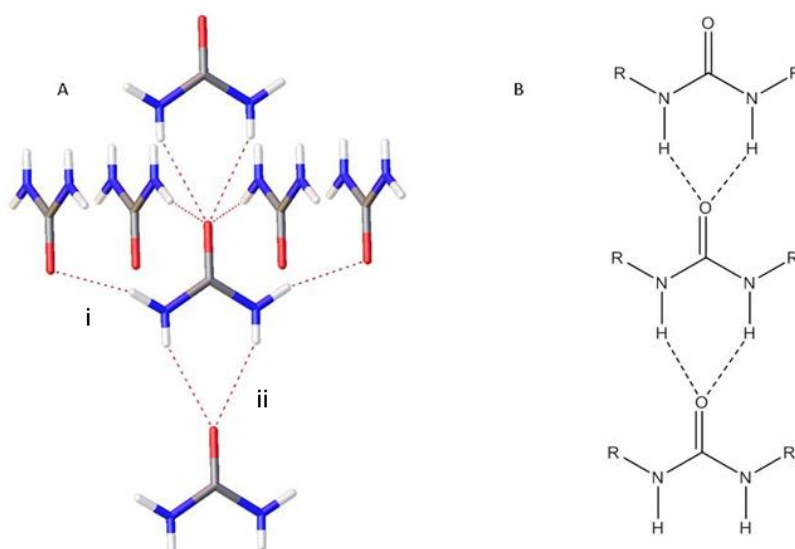


Figure 2-4. A) Crystal structure of  $\alpha$ -urea. B)  $\alpha$ -tape bonding in disubstituted urea.<sup>37</sup>

### 2.3 Effects of extreme conditions on supramolecular solids

While all crystalline solids exhibit some structural variation in response to changes in their environment, this variation can take many different forms. In high pressure studies, particularly those involving DACs, materials can be manipulated in more than one way. Compression can be used to crystallise substances which are liquid at ambient conditions; this may prove particularly useful if the substance is difficult to crystallise or has metastable forms which are difficult to isolate at ambient conditions. Alternatively, solutions of compounds which are solid at ambient



conditions may be compressed, reducing their solubility and facilitating nucleation within the DAC. Only certain solvents can be used for compression studies; as the nucleation occurs, the solvent must act as the hydrostatic medium which applies isotropic pressure to the crystal. Many solvents have low hydrostatic limits, after which point they no longer apply even pressure, or may freeze themselves to a glass or polycrystalline material.<sup>40</sup>

DACs can also be used to compress an existing single crystal of appropriate dimensions. Any of these methods can cause the sample to exhibit changes in its crystal structure.<sup>41</sup> Of significant interest are pressure-induced phase changes resulting in the discovery of new polymorphic forms, for example. Alternatively, the material may exhibit smaller structural changes; compression may occur anisotropically in one or two dimensions, accompanied by changes to the unit cell parameters and/or molecular conformation, or display negative linear compressibility.<sup>42</sup>

In certain cases, a structure may undergo significant structural changes at low temperature other than reduction in disorder and thermal motion; two of the chief motivations for conducting crystallography at low temperature. As with high pressure, low temperature may reveal phase changes or allow the nucleation of crystals or co-crystals which do not exist at ambient conditions.

Urea has a number of known polymorphs and co-crystals. The common ambient form phase I (or  $\alpha$  form) has a tetragonal structure in space group  $P\bar{4}2_1m$  with hydrogen bonding in a  $R_2^1(6)$  motif or “urea  $\alpha$ -tape”.<sup>43</sup> From crystals grown in a DAC, it is evident that a phase transition at 0.48 GPa yields the  $\gamma$  form (the  $\beta$  phase typically refers to the inclusion compound phase of urea) with space group  $P2_12_12_1$  and  $Z = 4$ . Further increasing the pressure to 2.8 GPa results in another transition to the  $\delta$  form, which also falls in the space group  $P2_12_12_1$  with  $Z = 2$ . In the  $\alpha$  form, the carbonyl oxygen atom forms four hydrogen bonds to atoms on three individual neighbouring molecules. This arrangement is similar to the bonding seen in the  $\delta$  phase, which can be considered a compressed version of the ambient  $\alpha$  form, in which the  $a$  axis is shortened by 2.16 Å and the  $b$  axis elongated by 1.77 Å (Figure 2-5). In both structures, each molecule forms 8 hydrogen bonds to its neighbours in total.

The  $\gamma$  phase occurs as an intermediate between the  $\alpha$  and  $\delta$  polymorphs and exhibits a distinctly different structure, with each carbonyl oxygen atom forming only three hydrogen bonds. Also, in comparison to the other polymorphs, the orientations of the molecules appear significantly altered.

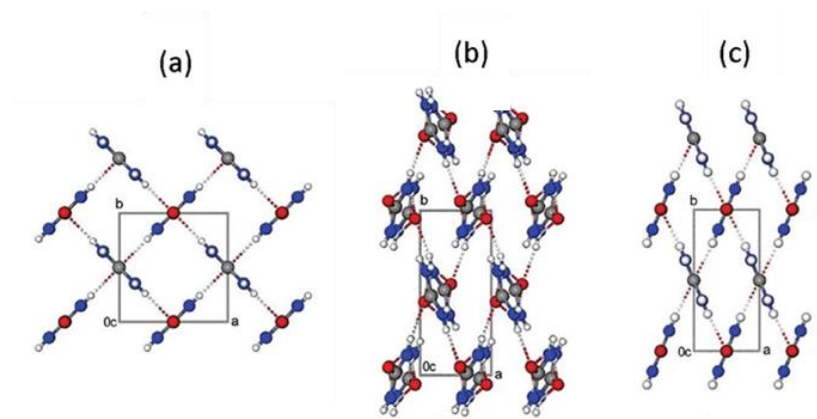


Figure 2-5. Ambient and high pressure phases of urea: (a)  $\alpha$ -phase  $P4_21m$  (b)  $\gamma$ -phase  $P2_12_12_1$  (c)  $\delta$ -phase  $P2_12_12_1$ .

The natural amino acids also display marked phase transitions as a result of elevated pressures. Glycine, the simplest of the amino acids, has three ambient polymorphs labelled  $\alpha$ ,  $\beta$  and  $\gamma$ . These are crystallised from different solvent systems but all comprise zwitterionic glycine molecules linked by  $NH\cdots O$  hydrogen bonds between the ammonium and carboxylate groups. The hydrogen-bonded molecules form one-dimensional chains, which are differently aligned in each of the three ambient polymorphs.<sup>44</sup>  $\alpha$ -glycine has been pressurised in increments up to 6.2 GPa with no change observed in its structure except for an increase in the efficiency of the crystal packing. This is consistent with data from Raman spectroscopy which indicates that the structure of  $\alpha$ -glycine persists up to pressures of 23 GPa. On the other hand,  $\beta$ -glycine undergoes a reversible single-crystal-to-single-crystal transition at 0.8 GPa to a  $\delta$  form, despite structural similarities to the non-responsive  $\alpha$  form under ambient conditions. At ambient conditions,  $\gamma$ -glycine differs from the other forms as it crystallises in the chiral space groups  $P3_1$  and  $P3_2$

and the hydrogen bonded chains arrange in a  $3_1$  screw axis rather than in layers. For this polymorph, a transition to  $\epsilon$ -glycine is seen between 2 and 4.3 GPa with a mixture of the two forms occurring at intermediate pressures, although this is not a single crystal transition and results in a polycrystalline sample. Like other forms,  $\epsilon$ -glycine has a layered structure. Interestingly, on lowering the temperature,  $\epsilon$ -glycine does not immediately convert back to the  $\gamma$  form but instead goes through an unstable intermediate called the  $\zeta$  phase. The structure of this phase has not been determined due to its short lifetime.

Other amino acids, such as serine, leucine and alanine, also show polymorphism under both ambient and extreme conditions.<sup>44</sup> Cysteine for example, which has two ambient forms, shows a decrease of 8.6% in the length of the  $a$  axis on compression of form I to 1.8 GPa, essentially closing up gaps in the extended structure as rows of molecules shift along the  $c$  axis. Upon further compression, a single-crystal-to-single-crystal transition occurs to a third phase, cysteine-III, during which the orientation of the sulfur-containing side-chain changes. On release of compression, cysteine-III is converted to cysteine-I *via* an intermediate, cysteine-IV, which is not seen during the pressure increase. Serine also shows two phase transitions under pressure, at 5.2 and 8.0 GPa, characterised by changes in the hydrogen bonds formed by the hydroxyl group.

Biomolecules other than amino acids are also susceptible to structural changes on the application of pressure. For example, the DNA fragments  $d(\text{GGTATACC})_2$  and  $d(\text{CGCGAATTCGCG})_2$  have both been studied at pressures up to 2 GPa.<sup>45</sup> The first of these crystallises in space group  $P6_1$  with six molecules in the unit cell. This molecule shows a decrease in cell volume up to 1.5 GPa but after this, displays negative compressibility as the pressure continues to increase. Diffraction from this DNA sequence stops above pressures of 2 GPa. Compressibility of the DNA is greatest in the direction of the double helix axis and relatively small in the other directions. The dodecamer, which crystallises in space group  $P2_12_12_1$ , is less stable to pressure and diffraction is lost above 0.7-0.8 GPa. The structure shows 1.9% compression in terms of unit cell volume at 0.3 GPa, with the same pattern of compression along the direction of the double helix.

Ridout *et al.* investigated the high pressure crystallisation and polymorphism of a series of fluorotoluenes that are liquid under ambient conditions and found that both 3- and 4-fluorotoluene exhibit polymorphism under extreme conditions of temperature and pressure.<sup>46</sup> 3-Fluorotoluene exhibits two forms: one in the space group  $P2_1/n$  (the LT form obtained at ambient pressure at 179 K) and another in  $Pbca$  (the HP form obtained at 10 kbar) The structural difference between the two is immediately evident on inspection (Figure 2-6). The HP structure is based on an ABCDABCD repeating pattern in one dimension, while the LT structure displays the same motif in two dimensions. The hydrogen-bonding pattern between layers is

different in each form, with the length of the C-H...F-C hydrogen bond changing from 2.682(3) Å (LT) to 2.441(3) Å (HP). Similarly, 4-fluorotoluene has a polymorph I (LT) in the space group  $P2_1/c$ , which converts under compression to polymorph II (HP), in the space group  $Pnma$ . Interestingly, the high-pressure polymorph exhibits longer hydrogen bond lengths (2.832(2) as opposed to 2.589(3) Å) despite its higher crystal density (1.290 g cm<sup>-3</sup> compared with 1.150 g cm<sup>-3</sup>). This polymorphism is likely the result of the relative weakening of C-H...F-C interactions at high pressures: the structure-directing effect of the hydrogen bonds is lost and maximisation of packing efficiency dictates the structure.

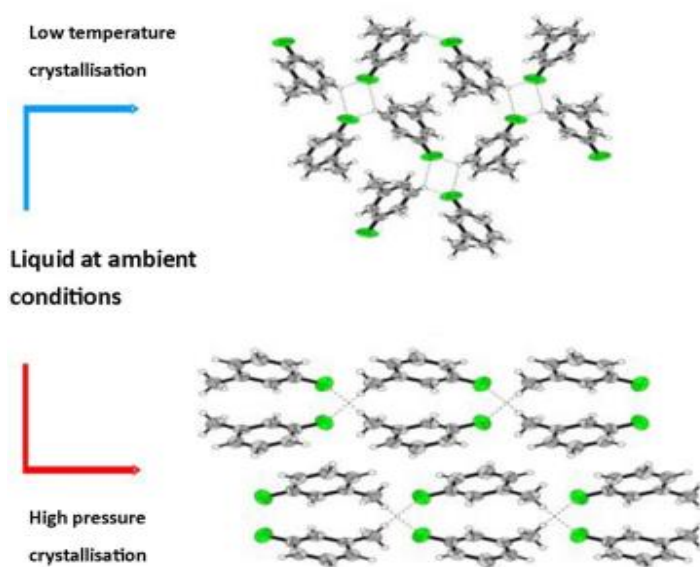


Figure 2-6. The HP and LT forms of 3-fluorotoluene.<sup>46</sup>

Pyrazole offers another example of an organic hydrogen bonded structure which exhibits both temperature and pressure dependency with regards to not only its structure but also its ferroelectric properties.<sup>47</sup> Ferroelectricity is the spontaneous polarisation of a material, which can be reversed by the application of an electric field. The ambient phase of pyrazole crystallises in space group  $Pna2_1$  with  $NH\cdots N$  bonds creating double loop helices. The protons are ordered within these hydrogen bonds. Interestingly, on an increase in temperature, disproportionation of the molecules occurs, showing a temperature dependent ionic disparity, as the protons in the  $NH\cdots N$  hydrogen bonds become disordered, resulting in partial charges on each pyrazole. It seems in this case, temperature alone is sufficient to introduce a neutral to ionic transition which is somewhat atypical between molecules of the same compound. On average, the charge of the cations and anions is +0.1 and -0.1 e, respectively, and in general, increases on increasing temperature although some fluctuation occurs. In addition to this temperature induced effect, the structure of pyrazole undergoes a phase transition above a pressure of 0.45 GPa at 296 K to a centrosymmetric phase  $\beta$ , similar to the  $\alpha$  phase but of higher symmetry in space group  $Pnab$  (Figure 2-7).

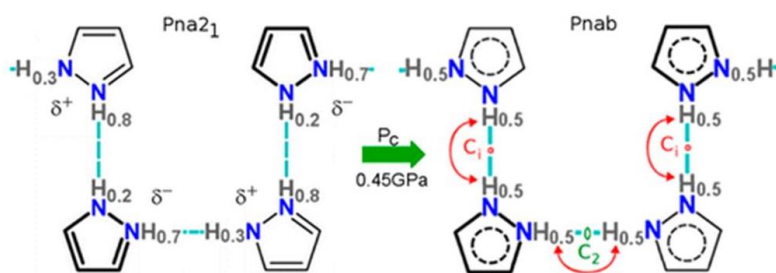


Figure 2-7. The phases of pyrazole showing partial charges and symmetry relationships present in the hydrogen bonding 'loop'.

Hydroquinone is an example of an inclusion compound which exhibits a different crystal form under pressures exceeding  $\sim 20$  MPa.<sup>48</sup> At ambient pressure and temperature, hydroquinone has three forms: the clathrate-forming  $\alpha$  and  $\beta$  and a more densely packed form,  $\gamma$ , which is accessible only *via* sublimation. The  $\beta$  and  $\gamma$  forms both spontaneously transform to the  $\alpha$  form, the most stable phase at room temperature. At 20 MPa and 432.1 K, the system undergoes a phase transition from the  $\alpha$  form to a new  $\delta$  form, demonstrated by Differential Thermal Analysis plots. At temperatures above or below 432.1 K, however, the pressure must be up to 90 MPa for the phase transition to occur. Unfortunately, the conditions under which the  $\delta$  phase exists have not been recreated on a diffractometer so the crystal structure has not been determined. Nonetheless, using the crystal densities and intermolecular potential, it has been concluded that the  $\delta$  form may be similar to the  $\gamma$  form, in the monoclinic space group  $P2_1/c$  and exhibiting four molecules in its unit cell.



Johnstone *et al.* studied single crystals of salicylamide at ambient pressures and up to 5.1 GPa with a DAC. Structural changes were investigated both by compressing an existing single crystal and by growing crystals *in situ*.<sup>49</sup> Salicylamide crystallises under ambient conditions in the space group  $I2/a$  and the hydrogen bonding pattern effectively gives planar dimerization of the molecules, which then form an open network *via*  $\pi\cdots\pi$  stacking interactions. On compression to 5.1 GPa, an anisotropic change is seen in the unit cell parameters; the  $c$  axis decreases by 14.5%, as well as a 4.7% and 4.1% decrease in the  $a$  and  $b$  axes, respectively. The effect of this change is to push the layers of hydrogen bonded molecules closer together. *In situ* crystallisation of salicylamide at 0.2 GPa results in another polymorph, (space group  $P2_12_12_1$ ) similar to that found at ambient conditions but with a twist in the amide group that leads to a change in torsional angle of  $4.1^\circ$ . As a result of the altered amide conformation, the molecules no longer form dimers, but still exhibit two intermolecular hydrogen bonds with the same donor-acceptor pairing.

High pressure diffraction can be used as a tool for investigating the effect of pressure on APIs such as paracetamol. A material may be analysed under compression to screen for polymorphic transitions or investigate the effect of tableting process on the crystal structure. For example, DAC studies were used by Boldyreva *et al* to study the structures of the monoclinic Form I and orthorhombic Form II forms of paracetamol, by compression to 4.5 GPa and 5.5 GPa,

respectively.<sup>50</sup> The bulk compressibilities of the two forms are similar, but the systems display differing anisotropy in their pressure-induced structural changes. Form II exhibits a contraction in three dimensions while Form I displays some expansion above 1.5 GPa. No polymorphic transitions have been observed for either form up to 4.5 GPa on increasing and decreasing the pressure.

Methanol is a representative example of a substance which exhibits polymorphism as a result of changes in both temperature and pressure. On cooling, methanol freezes at 175.37 K, giving the 'high temperature'  $\beta$  phase ( $Cmc2_1$ ) which undergoes a first order phase transition to the lower temperature  $\alpha$  phase ( $P2_12_12_1$ ) at 156-159 K.<sup>17</sup> There is debate as to whether there is a second, second-order phase transition between 156 and 159 K, but no structural information has been reported for this elusive phase.<sup>51</sup> Methanol also has a third structure in  $P\bar{1}$ , which is made evident not by temperature but by increasing the pressure on a single crystal. This was done in a DAC by increasing the pressure above 7 GPa to give a number of crystallites, then reducing the pressure until one seed crystal remained which was subsequently grown to fill the gasket hole at 4.0 GPa.<sup>52</sup>

Low temperature can not only enable crystals to be obtained which do not exist at ambient conditions, but also may reveal polymorphism of a substance. An example of both these outcomes is given by diphenyl ether.<sup>53</sup> The crystal structure of this organic solvent had not been solved previously but *in situ* cryo-crystallisation

allowed a suitable single crystal to be grown in order to obtain a structure in monoclinic space group  $P2_1/n$  at 250 K (Figure 2-8). It was then found that at only 10 K difference, at 240 K, a second orthorhombic form exists in  $P2_12_12_1$ . Both crystallisations were achieved by flash-freezing with  $N_2$  gas and then cycling the temperature until a single crystal was obtained.

There is a small conformational change seen in the diphenyl ether molecule itself with angles between the phenyl ring planes of  $88.4^\circ$  and  $87.6^\circ$  for forms I and II respectively. The largest contribution to the structural change comes from the  $CH\cdots\pi$  interactions. In form one, a three dimensional network is formed with chains of molecules along the  $a$  axis which link to form the larger structure. For form II however,  $CH\cdots\pi$  interactions cause the molecules to form tetramers, which then stack into the extended structure *via*  $CH\cdots O$  interactions. The exact temperature at which this phase change occurs is not reported.

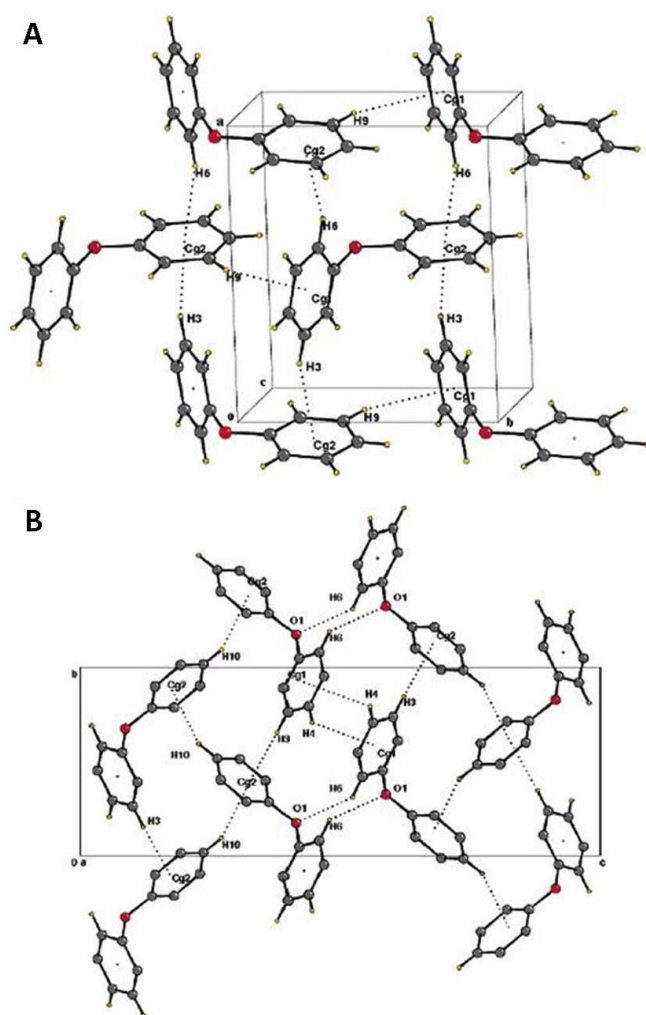


Figure 2-8. Polymorphs of diphenyl ether. A) Form I  $P2_1/n$  (250 K). B) Form II  $P2_12_12_1$  (240 K).

A more complex structure which is affected by external pressure is the ‘magnetic sponge’  $\{[\text{Mn}^{\text{II}}(\text{pydz})(\text{H}_2\text{O})_2][\text{Mn}^{\text{II}}(\text{H}_2\text{O})_2][\text{Nb}^{\text{IV}}(\text{CN})_8]\cdot 3\text{H}_2\text{O}\}_n$  (**2**).<sup>54</sup> At ambient conditions, this compound crystallises from aqueous solution in space group  $P2_1/c$  into a three dimensional grid system with Nb centres and Mn-NC-Nb ladder motifs. Of the eight CN ligands surrounding the niobium centres, seven of them are bridging to manganese ions, with the magnetic moments of the metal centres

aligned anti-parallel, causing the material to be a soft ferrimagnet below the critical temperature  $T_c$  of 43.5 K. The Nb-C bonds of the bridges are the main structural feature affected by the application of pressure. At 1.8 GPa in a DAC, the structure of **2** is similar to the ambient pressure structure but the unit cell has been compressed by ~7.6 % in volume, with shortening of the Nb-C bonds. This is presumed to be the reason for changes in the value of  $T_c$  which are seen with increasing pressure. At pressures 0.57, 0.27 and 0.0 GPa,  $T_c$  has values of 51.0, 48.0 and 43.5 K respectively. This indicates that the antiferromagnetic coupling between Mn and Nb *via* the Nb-CN-Mn bonds is enhanced as the bridge bond shortens with increasing pressure, improving the exchange of spin density between the relevant magnetic orbitals on the metals.

It is becoming evident as research into high pressure crystallography increases that certain crystal forms are only accessible when crystallised *in situ* at high pressures. One such crystal form is the heptahydrate of gabapentin, a  $\gamma$ -amino acid which is a Pfizer product prescribed for the treatment of epilepsy.<sup>55</sup> At ambient pressure, gabapentin has three polymorphs as well as a monohydrate and a hemihydrate hydrochloride salt. The crystals were grown from a saturated aqueous solution of gabapentin in a diamond anvil cell. On precipitation of a number of crystallites at 0.8 GPa, temperature control was used to isolate a single crystallite which was subsequently grown to a suitable size for diffraction. This method was repeated and two crystals were used to collect data, at pressures of 0.87 and 0.90 GPa. The

gabapentin in this structure is in its zwitterionic state, is highly dipolar and as such the structure as a whole consists primarily of alternating columns of polar and non-polar interactions. These two molecule-thick columns have a parallel/anti-parallel arrangement with regards to dipole orientation, and this is also seen in the monohydrate form of gabapentin.

#### 2.4 Concluding remarks

Although work in the area of extreme conditions crystallography has generated significant interest in recent decades, it is still largely an untapped resource for further understanding of structure and bonding interactions in both organic and inorganic solids. What systems have been studied under non-ambient conditions tend to be smaller, inorganic or organometallic compounds, and there is much room for improvement in the investigation into organic and supramolecular systems.

## 2.5 References

1. J. T. A. Jones, T. Hasell, X. Wu, J. Bacsá, K. E. Jelfs, M. Schmidtman, S. Y. Chong, D. J. Adams, A. Trewin, F. Schiffman, F. Cora, B. Slater, A. Steiner, G. M. Day and A. I. Cooper, *Nature*, 2011, **474**, 367-371.
2. K.-S. Huang, D. Britton, M. C. Etter and S. R. Byrn, *J. Mater. Chem.*, 1997, **7**, 713-720.
3. J. W. Steed, *Trends Pharmacol. Sci.*, 2013, **34**, 185-193.
4. G. R. Desiraju, *CrystEngComm*, 2003, **5**, 466-467.
5. J. D. Dunitz, *CrystEngComm*, 2003, **5**, 506-506.
6. L. J. Barbour, D. Das, T. Jacobs, G. O. Lloyd and V. J. Smith, *Supramolecular Chemistry: From Molecules to Nanomaterials*, John Wiley & Sons, Ltd, 2012.
7. C. B. Aakeröy, M. E. Fasulo and J. Desper, *Mol. Pharm.*, 2007, **4**, 317-322.
8. C. B. Aakeroy and D. J. Salmon, *CrystEngComm*, 2005, **7**, 439-448.
9. N. Qiao, M. Li, W. Schlindwein, N. Malek, A. Davies and G. Trappitt, *Int. J. Pharm.*, 2011, **419**, 1-11.
10. N. Shan and M. J. Zaworotko, *Drug Discovery Today*, 2008, **13**, 440-446.
11. S. Zhang, H. Chen and A. C. Rasmuson, *CrystEngComm*, 2015, **17**, 4125-4135.
12. J. A. Bis, P. Vishweshwar, D. Weyna and M. J. Zaworotko, *Mol. Pharm.*, 2007, **4**, 401-416.
13. P. Vishweshwar, J. A. McMahon, J. A. Bis and M. J. Zaworotko, *J. Pharm. Sci.*, 2006, **95**, 499-516.
14. D. S. Yufit and J. A. K. Howard, *CrystEngComm*, 2010, **12**, 737-741.
15. D. S. Yufit, R. Zubatyuk, O. V. Shishkin and J. A. K. Howard, *CrystEngComm*, 2012, **14**, 8222-8227.
16. D. S. Yufit and J. A. K. Howard, *CrystEngComm*, 2012, **14**, 2003-2008.
17. M. T. Kirchner, D. Das and R. Boese, *Cryst. Growth Des.*, 2008, **8**, 763-765.
18. H. Davy, *Philos. Trans. R. Soc. London*, 1811, **101**, 1-35.
19. D. E. Palin and H. M. Powell, *Nature*, 1945, **156**, 334-335.
20. J. W. Steed and J. L. Atwood, *Supramolecular Chemistry*, John Wiley & Sons, Chichester, 2nd edn., 2009.
21. P. Sixou and P. Dansas, *Berichte der Bunsengesellschaft für physikalische Chemie*, 1976, **80**, 364-389.
22. W. A. Caspari, *Journal of the Chemical Society (Resumed)*, 1926, **129**, 2944-2948.
23. D. E. Palin and H. M. Powell, *Journal of the Chemical Society (Resumed)*, 1948, **0**, 815-821.
24. N. Arulsamy, D. S. Bohle, J. L. Butikofer, P. W. Stephens and G. T. Yee, *Chem. Commun.*, 2004, 1856-1857.
25. S. C. Wallwork and H. M. Powell, *Journal of the Chemical Society-Perkin Transactions 2*, 1980, **0**, 641-646.
26. A. Zinke, E. Ziegler, E. Martinowitz, H. Pichelmayer, M. Tomio, H. Wittmann-Zinke and S. Zwanziger, *Ber. Dtsch. Chem. Ges. B*, 1944, **77B**, 264-272.
27. C. D. Gutsche and R. Muthukrishnan, *J. Org. Chem.*, 1978, **43**, 4905-4906.
28. G. D. Andreetti, R. Ungaro and A. Pochini, *J. Chem. Soc., Chem. Commun.*, 1979, **0**, 1005-1007.

29. I. Stibor and P. Lhotak, in *Encyclopedia of Supramolecular Chemistry*, eds. J. L. Atwood and J. W. Steed, Marcel Dekker, New York, 1 edn., 2004, vol. 1, pp. 145-152.
30. G. D. Enright, K. A. Udachin and J. A. Ripmeester, *Chem. Commun.*, 2004, 1360-1361.
31. K. A. Udachin, G. D. Enright, P. O. Brown and J. A. Ripmeester, *Chem. Commun.*, 2002, 2162-2163.
32. J. A. Ripmeester, G. D. Enright, C. I. Ratcliffe, K. A. Udachin and I. L. Moudrakovski, *Chem. Commun.*, 2006, 4986-4996.
33. J. L. Atwood, L. J. Barbour, A. Jerga and B. L. Schottel, *Science*, 2002, **298**, 1000-1002.
34. C. Tedesco, L. Erra, M. Brunelli, V. Cipolletti, C. Gaeta, A. N. Fitch, J. L. Atwood and P. Neri, *Chem. Eur. J.*, 2010, **16**, 2371-2374.
35. P. K. Thallapally, B. P. McGrail, J. L. Atwood, C. Gaeta, C. Tedesco and P. Neri, *Chem. Mater.*, 2007, **19**, 3355-3357.
36. L. Erra, C. Tedesco, V. R. Cipolletti, L. Annunziata, C. Gaeta, M. Brunelli, A. N. Fitch, C. Knofel, P. L. Llewellyn, J. L. Atwood and P. Neri, *PCCP*, 2012, **14**, 311-317.
37. N. Sklar, M. E. Senko and B. Post, *Acta Crystallogr.*, 1961, **14**, 716-720.
38. M. George, G. Tan, V. T. John and R. G. Weiss, *Chemistry - A European Journal*, 2005, **11**, 3243-3254.
39. A. Masunov and J. J. Dannenberg, *The Journal of Physical Chemistry B*, 2000, **104**, 806-810.
40. R. Lee, J. A. K. Howard, M. R. Probert and J. W. Steed, *Chem. Soc. Rev.*, 2014, **43**, 4300-4311.
21. E. Boldyreva, *Acta Crystallographica Section A*, 2008, **64**, 218-231.
42. A. B. Cairns, J. Catafesta, C. Levelut, J. Rouquette, A. van der Lee, L. Peters, A. L. Thompson, V. Dmitriev, J. Haines and A. L. Goodwin, *Nat. Mater.*, 2013, **12**, 212-216.
43. A. Olejniczak, K. Ostrowska and A. Katrusiak, *J. Phys. Chem. C*, 2009, **113**, 15761-15767.
44. S. A. Moggach, S. Parsons and P. A. Wood, *Crystallogr. Rev.*, 2008, **14**, 143-184.
45. I. Ascone, R. Kahn, E. Girard, T. Prange, A.-C. Dhaussy, M. Mezouar, N. Ponikwicki and R. Fourme, *J. Appl. Crystallogr.*, 2010, **43**, 407-416.
46. J. Ridout and M. R. Probert, *Cryst. Growth Des.*, 2013, **13**, 1943-1948.
47. M. Sikora and A. Katrusiak, *J. Phys. Chem. C*, 2013, **117**, 10661-10668.
48. M. Naoki, T. Yoshizawa, N. Fukushima, M. Ogiso and M. Yoshino, *The Journal of Physical Chemistry B*, 1999, **103**, 6309-6313.
49. R. D. L. Johnstone, A. R. Lennie, S. F. Parker, S. Parsons, E. Pidcock, P. R. Richardson, J. E. Warren and P. A. Wood, *CrystEngComm*, 2010, **12**, 1065-1078.
50. E. V. Boldyreva, T. P. Shakhtshneider, H. Ahsbahs, H. Sowa and H. Uchtmann, *J. Therm. Anal. Calorim.*, 2002, **68**, 437-452.
51. B. H. Torrie, O. S. Binbrek, M. Strauss and I. P. Swainson, *J. Solid State Chem.*, 2002, **166**, 415-420.
52. D. R. Allan, S. J. Clark, M. J. P. Brugmans, G. J. Ackland and W. L. Vos, *Phys. Rev. B: Condens. Matter Mater. Phys.*, 1998, **58**, R11809-R11812.
53. A. R. Choudhury, K. Islam, M. T. Kirchner, G. Mehta and T. N. Guru Row, *J. Am. Chem. Soc.*, 2004, **126**, 12274-12275.



54. D. Pinkowicz, K. Kurpiewska, K. Lewinski, M. Balanda, M. Mihalik, M. Zentkova and B. Sieklucka, *CrystEngComm*, 2012, **14**, 5224-5229.
55. F. P. A. Fabbiani, D. C. Levendis, G. Buth, W. F. Kuhs, N. Shankland and H. Sowa, *CrystEngComm*, 2010, **12**, 2354-2360.

# Chapter 3 Neutron Diffraction Studies on Guest-Induced Distortions in Urea Inclusion Compounds

---

## 3.1 Introduction

Urea inclusion compounds (UICs), the  $\beta$ -phase of urea, were first discovered in 1949 by Schlenk and described as “urea addition crystals”.<sup>1</sup> Since then this class of compound has been studied comprehensively, and found to display various structural and behavioural characteristics of interest, largely influenced by the nature of the guest molecule. These crystals have a hexagonally symmetrical honeycomb channel structure formed by an extensively hydrogen bonded helical urea network which encapsulates the guest molecules (Figure 3-1).<sup>2</sup> A variety of guest compounds facilitate UIC formation, within certain limitations; typically relatively long chain molecules with little or no branching. This includes long chain alkanes  $C_7H_{16}$  to  $C_{20}H_{42}$ ,<sup>3</sup>  $\alpha,\omega$ -dihaloalkanes  $X(CH_2)_n X$  where  $n = 7-10$ ,<sup>4</sup> and  $(\alpha+1),(\omega-1)$ -diketones,<sup>5</sup> among other long chain and slightly branched compounds. When the guest is altered, so too is the behaviour of the host network. Despite the degree of interest in this class of compounds, few neutron diffraction experiments have been used in their study, and then only on incommensurate examples.<sup>6</sup> Neutron Laue diffraction had been utilized to study phase transitions of an  $n$ -nonadecane UIC, identifying a previously unseen phase transition and associated superspace group.<sup>7</sup>  $n$ -Hexadecane/urea has been previously studied by both X-ray

and neutron diffraction techniques but no atomic coordinates are reported in the CSD.<sup>6, 8</sup> Discussed here is the first commensurate urea inclusion compound structures elucidated from single crystal neutron diffraction experiments.

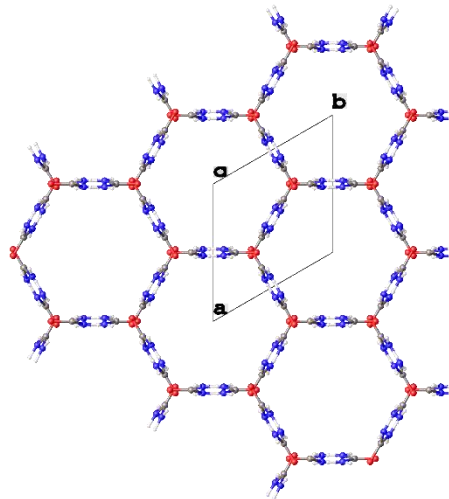


Figure 3-1. X-ray structure of urea with hexadecane guest, viewed down *c* axis. Host structure only is shown for clarity.

The host-guest relationship is classed as incommensurate when no sensible integers can be found to satisfy the relationship  $nc_g = mc_h$ , where  $c_h$  and  $c_g$  are the repeat distances of the host and guest, respectively.<sup>9</sup> The dynamic disorder of the guest causes the overall structure to maintain the hexagonal symmetry of the urea network. The simplest class of UIC contains an alkane guest, which has an incommensurate host-guest relationship and significant disorder in the host channels.<sup>3</sup>

A commensurate relationship between the host and guest may also be observed, in cases where hydrogen bonding occurs between the guest and urea molecules, or

when the guest can adopt a conformation which is complementary to the periodicity of the host. A number of bis(methyl) ketone UICs display a commensurate relationship as the carbonyl groups form hydrogen bonds with adjacent urea molecules in the host wall.<sup>5</sup> In the case of 2,10-undecanedione/urea, the resulting distortion creates macroscopic domains within the crystal structure which are susceptible to reorientation when a small compressive stress is applied to certain crystal faces, resulting in ferroelastic behaviour.<sup>10</sup>

UICs of 1,6-dibromohexane, 1-bromo-6-chlorohexane and 1,6-dichlorohexane also exhibit a commensurate host-guest relationship.<sup>4</sup> In this instance the guest coils into an atypical gauche conformation to avoid unfavourable guest-guest interactions and creates a distortion of the host network away from hexagonal symmetry as a result of the cross sectional shape of the dihaloalkane.<sup>4, 11</sup> The guests undergo torsional conversions between gauche conformations in a temperature dependent manner; at higher temperatures the guests are more mobile and the structures experience a phase transition to a higher symmetry hexagonal phase, as increased frequency of torsional jumps equilibrates the internal stress applied to the host by the guest.

Temperature dependent phase transitions are consistently seen across a range of UICs, for example both 1,10-dibromodecane and 1,12-dibromododecane UICs display a single-crystal to single-crystal phase transition going from a high temperature hexagonal phase typical of high symmetry UICs, to a lower temperature orthorhombic structure.<sup>12</sup> In both cases, this host-guest relationship

remains incommensurate, much like that of alkane UICs. This further highlights the importance of guest size on commensurability of UICs, as 1,6-dibromohexane from the same  $\alpha,\omega$ -dihaloalkane family of compounds has a commensurate relationship with the urea network.

The UIC of 2-bromotetradecane also transitions from a high temperature hexagonal phase to a lower temperature orthorhombic phase, and further to a monoclinic phase below 142 K.<sup>13</sup> The distortions of the channel on lowering the temperature can be attributed to changes in guest molecule orientation, although the structure is incommensurate regardless of temperature. As the guests' dynamic orientational disorder is reduced at lower temperature, the host network adopts a lower symmetry, accommodating the change.

In this work we undertake a detailed study of the hydrogen bonding interactions in the urea host network and between urea and guest molecules using complementary single crystal X-ray and neutron diffraction. Particular emphasis is placed on examples of UICs which, due to unusual interaction between the host and guest, display atypical structural features resulting in distortion of the host network away from the classical hexagonal symmetry of  $\beta$ -urea.<sup>5, 11</sup>

### 3.2 Experimental

1,6-Dibromohexane, hexadecane and urea were obtained from Sigma-Aldrich. DMF was obtained from Fisher Scientific. 2,7-Octanedione was obtained from Aurora Fine Chemicals LLC. 1,6-Dibromohexane/urea (DBH) was crystallised by slow cooling

from MeOH. Urea-DMF (UDM) was crystallised from a concentrated solution of urea in DMF.<sup>14</sup> Hexadecane UIC (HEX) was crystallised by adding liquid hexadecane to a solution of urea in MeOH, then adding 2-propanol dropwise until the components were miscible. The solution was agitated by sonication until clear and allowed to slowly evaporate.

Single crystal X-ray data were collected on an Agilent Gemini S-Ultra diffractometer equipped with Cryostream (Oxford Cryosystems) open-flow nitrogen cryostat, using graphite monochromated Mo K $\alpha$ -radiation ( $\lambda = 0.71069\text{\AA}$ ). All structures were solved by direct methods and refined by full-matrix least squares on  $F^2$  for all data using SHELX-2015/2<sup>15</sup> and OLEX2<sup>16</sup> software. All non-hydrogen atoms were refined with anisotropic displacement parameters, hydrogen atoms were located on the difference Fourier maps and refined isotropically. All X-ray structures henceforth discussed (DBH, OCT, UDM) refer to those reported in existing literature.<sup>5, 8, 11, 14</sup> except for HEX, which was re-determined in order to obtain atomic coordinates of the host network.

Neutron data were collected on the thermal four-circle D19 diffractometer at ILL, Grenoble which uses a large position sensitive detector ( $120^\circ \times 30^\circ$ ) and two stage Displex cryorefrigerator for cooling. An incident wavelength of  $1.1698\text{\AA}$  was used for DBH and HEX, and UDM. For OCT a wavelength of  $1.4547\text{\AA}$  was used.

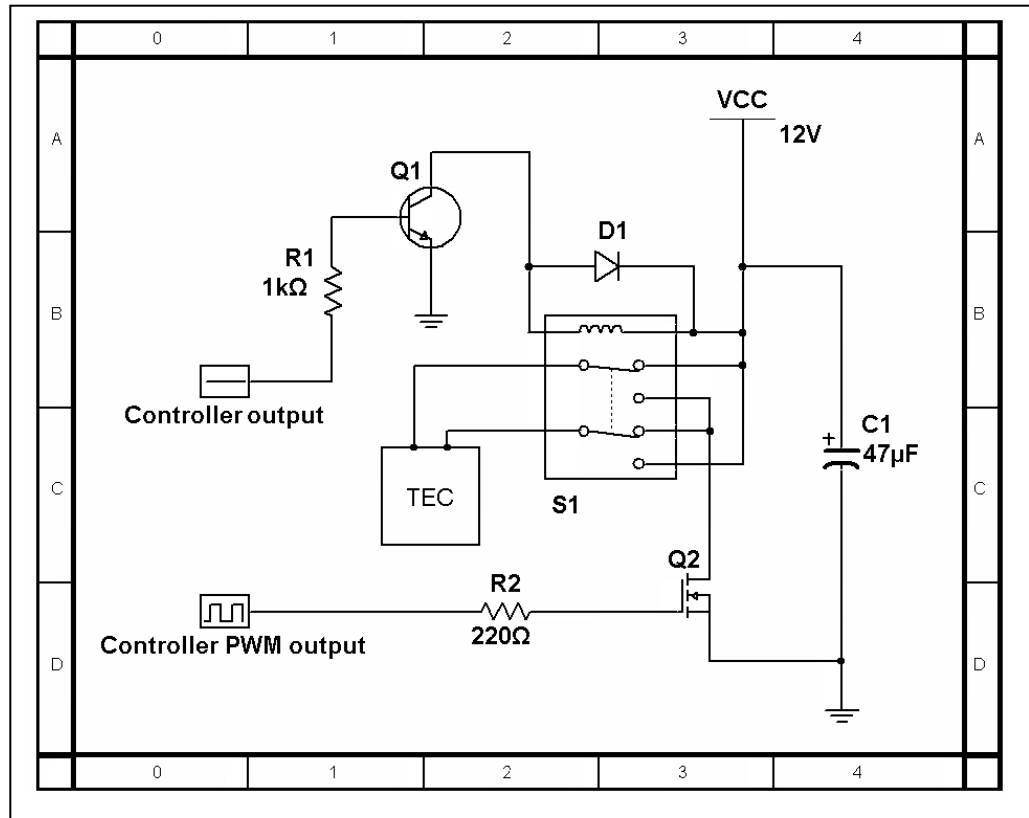
High pressure studies were carried out using a diamond anvil cell, by loading crystals of each compound into a gasket of 0.25 mm steel pre-indented to 0.15 mm with a precision drilled  $300\text{ }\mu\text{m}$  hole, situated between two diamond anvils.<sup>17</sup>

Paraffin oil was used as the hydrostatic medium and a ruby chip was added to the cell to allow pressure determination by the ruby fluorescence method.<sup>18</sup> Data were collected on the XIPHOS II diffractometer at Newcastle University, using a four-circle Huber goniometer with Ag-K $\alpha$   $I\mu S$  generator.<sup>19-21</sup>

Urea / 2,7-octanedione (OCT) was crystallised using a specially designed Peltier thermoelectric cooling (TEC) unit (see below). A concentrated methanol solution of urea and 2,7-octanedione was cooled from 50°C to 12°C over a period of 4 days and held at 12°C for a further 2 days to optimise crystal size. After this point, the crystals proved to degrade rapidly unless removed from the mother liquor and stored under inert oil.

### 3.2.1 Design of a heating/cooling Peltier thermoelectric cooler

Schematic 3-1 shows the circuit design of the Peltier TEC control unit. The controller outputs are 5V TTL logic level, all resistors are rated for ¼ watt and the TEC used was a TEC1-12706 (72 W). The relay S1 is a double-pole double-throw type wired in an H-bridge configuration. By altering the frequency of the pulse-width modulated signal supplied to the gate of the N-channel MOSFET Q2 (P35NF10), the power delivered to the TEC is governed by the controller. The direction that heat is pumped across the TEC can be changed by signalling the NPN transistor Q1 (2N3904), this causes the relay S1 to latch and inverts the polarity applied across the TEC. Source code for the controller and additional information on the circuit design can be found at: <https://github.com/nu-xtal-tools/ControlTEC>.



Schematic 3-1. Circuit design of the Peltier TEC control unit

### 3.3 Results

Urea inclusion compounds of hexadecane, 2,7-octanedione, 1,6-dibromohexane and N,N-dimethylformamide (Figure 3-2), were crystallised and analysed by both X-ray and neutron diffraction at a range of temperatures. These particular examples were chosen as they represent a series where the changing guest,<sup>4, 5, 8</sup> or co-former,<sup>14</sup> varies the symmetry and bonding in a pseudo-systematic way. HEX is a representative example of a ‘typical’ hexagonal urea clathrate and is the simplest and most symmetrical UIC in the group, OCT maintains hexagonal symmetry at the expense of hydrogen bonding continuity and unit cell size, DBH has monoclinic symmetry as a result of internal stress applied by a bulky guest molecule, and UDM is not a traditional channel type inclusion compound, but maintains certain



structural features similar to the hexagonal channel along one axis. In addition, the guest molecules were chosen for OCT and DBH as their UIC structures were known to be commensurate, eliminating any barriers to observing the finer detail of hydrogen bonding, which is difficult to resolve in incommensurate structures due to guest disorder.

The main features of each structure are outlined in this section. Further analysis and comparison of structure and bonding can be found in the discussion section.

Table 3-1. Summary of crystallographic data from neutron diffraction experiments.

	HEX		DBH			OCT	UDM	
Formula	C <sub>9</sub> H <sub>12</sub> N <sub>6</sub> O <sub>3</sub>		C <sub>6</sub> H <sub>12</sub> Br <sub>2</sub> 6(CH <sub>4</sub> N <sub>2</sub> O)			C <sub>8</sub> H <sub>14</sub> O <sub>2</sub> 7(CH <sub>4</sub> N <sub>2</sub> O)	C <sub>3</sub> H <sub>4</sub> NO 3(CH <sub>4</sub> N <sub>2</sub> O)	
T/ K	150	260	30	120	260	30	30	120
Crystal system	Hexagonal		Monoclinic			Hexagonal	Triclinic	
Space group	P6 <sub>5</sub> 22		P2 <sub>1</sub> /n			P6 <sub>5</sub> 22	P $\bar{1}$	
a/ Å	8.1529(5)	8.1219(14)	8.5518(2)	8.5793(6)	8.5793(6)	8.1007(5)	7.3797(2)	7.4648(3)
b/ Å	8.1529(5)	8.1219(14)	10.8605(2)	10.8922(8)	10.8922(8)	8.1007(5)	9.9588(3)	9.8804(4)
c / Å	10.9819(6)	10.9891(13)	13.3296(3)	13.4160(12)	13.4160(12)	76.213(5)	10.9509(2)	10.8588(3)
$\alpha$ / °	90		90			90	64.5386(13)	65.2370(19)
$\beta$ / °	90		92.919(2)	92.779(7)	92.779(7)	90	77.4999(14)	78.769(2)
$\gamma$ / °	120		90			120	67.8699(14)	69.732(2)
Z	2		2			6	4	
Z'	0.167		0.5			0.5	2	
Z''	2		4			5	4	
V/ Å <sup>3</sup>	632.17(7)	627.78(17)	1236.40(5)	1252.22(17)	1252.2(2)	4331.1(5)	671.68(3)	681.06(5)
D <sub>c</sub>	1.325	1.335	1.623	1.603	1.603	1.294	1.253	1.235
Unique reflns.	2838	2453	12134	13110	13186	18067	7491	7193
Completeness %	93	90	92	92	92	97	88	88
R <sub>1</sub>	0.068	0.062	0.032	0.042	0.043	0.091	0.055	0.054
wR <sub>2</sub>	0.188	0.181	0.066	0.093	0.088	0.203	0.142	0.014
GooF	1.12	1.11	1.19	1.16	1.05	1.15	1.17	1.11

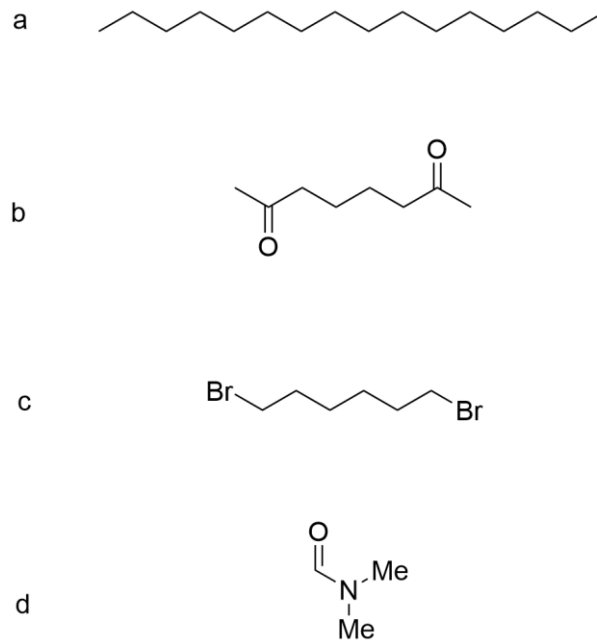


Figure 3-2. a) Hexadecane. b) 2,7-octanedione. c) 1,6-dibromohexane. d) N,N-dimethylformamide.

### 3.3.1 Urea Hexadecane

The X-ray crystal structure of urea/hexadecane, was reported by Chatani *et al.* in 1976.<sup>8</sup> Figure 3-3, derived from the re-determined X-ray structure, demonstrates how the complex displays a characteristic hexagonal channel motif, with the 16 carbon atom guest molecule hexadecane occupying the channels.<sup>22</sup> Given the lack of hydrogen bonding capability or other functionality in the included hydrocarbon, the guest has an incommensurate relationship with the host network and is significantly disordered throughout the structure. It appears in the X-ray experiment as a 'smear' of electron density within the one dimensional channels. This structure offers a useful example of a symmetrical channel essentially unperturbed by guest interactions given the  $\beta_0$  hexagonal framework has never been crystallised without a guest present.<sup>23</sup>

The structure and dimensions of this UIC represent a model urea framework against which other analogues can be compared. This contrast will contribute to understanding the extent to which the guest can influence the nature of the host network.

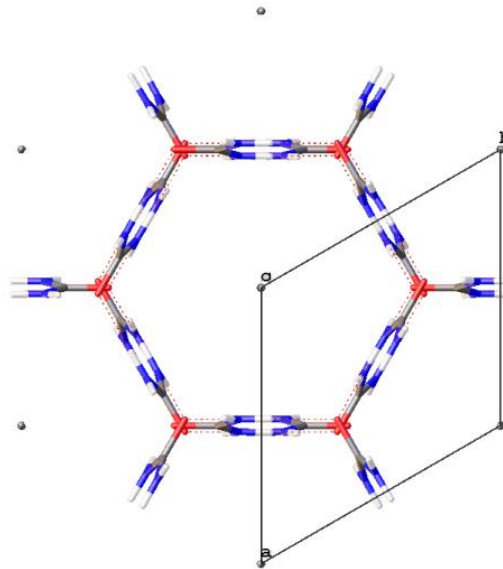


Figure 3-3. View along *c* axis of urea/hexadecane showing cross section of one 1D channel with unit cell superimposed. Hexadecane appears as a grey dot in the channel centre.

At 150 K the UIC of hexadecane adopts space group  $P6_122$  (Table 3-1). Below 150 K, a phase transition is observed which consistently causes the crystals to become multiply twinned and makes further single crystal diffraction unfeasible. Yeo *et al.* determined this low temperature phase to be orthorhombic  $P2_12_12_1$  from powder diffraction data by Rietveld refinement, using the high temperature phase as a model, producing a distorted form of the hexagonal phase arising from reduced motion of the guest in the channels.<sup>24</sup> When the crystal (Figure 3-4) was warmed

back to 151 K, the phase transition is reversible, and the split peaks merge (Figure 3-5). This is notable as typically, split diffraction spots are associated with degradation and cracking of the crystal due to a phase transition and often is not reversible.

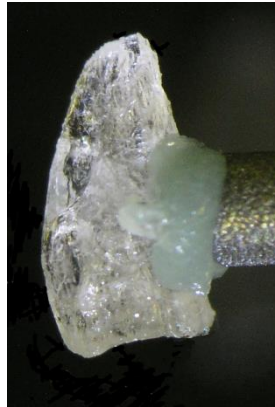


Figure 3-4. Crystal of HEX mounted on a vanadium pin.

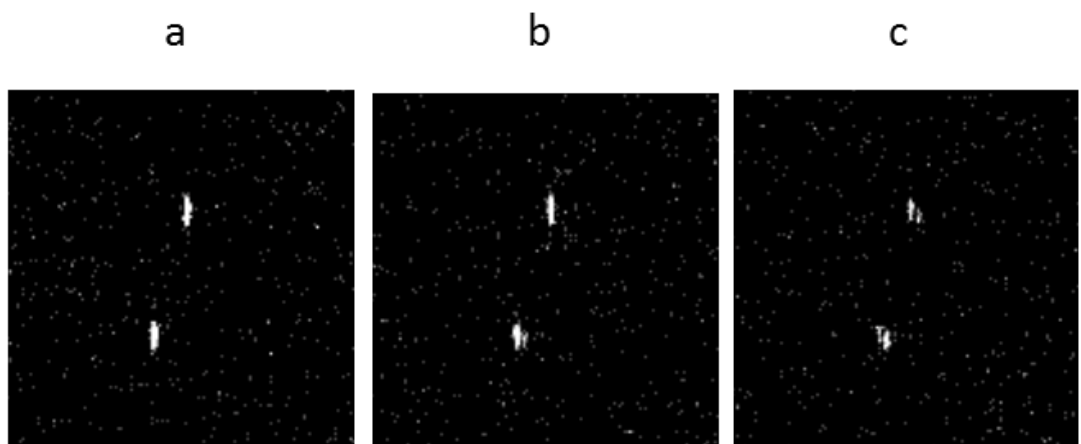


Figure 3-5. Peak splitting on cooling HEX a) 151 K, b) 150 K, c) 149 K.

A similar example of such unusual behaviour is seen for piroxicam monohydrate,<sup>25</sup> which on cooling between 120 and 22 K undergoes peak splitting. Within 11 hours, the peaks have re-merged although in this case, there is no evidence for a first

order phase transition as both the 120 K data and that collected at 22 K after peak coalescence show the same monohydrate phase and the re-merging of the peaks is time dependent, rather than temperature dependent.

The asymmetric unit of HEX contains a partial urea molecule, thus the hydrogen bonding for the entire system can be described by the two symmetry unique hydrogen bonds of the  $\text{NH}_2$  group (Figure 3-6). Data collected by single crystal neutron diffraction were used to determine the hydrogen bonding distances between urea molecules, detailed in Table 3-4.

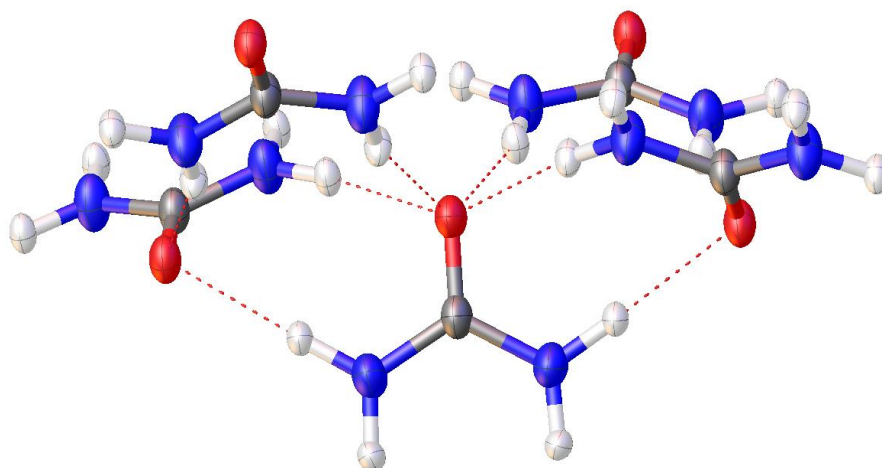


Figure 3-6. Hydrogen bonds in UIC of hexadecane. All urea molecules are equivalent. Hexadecane guest omitted for clarity.

### 3.3.2 Urea 1,6-dibromohexane

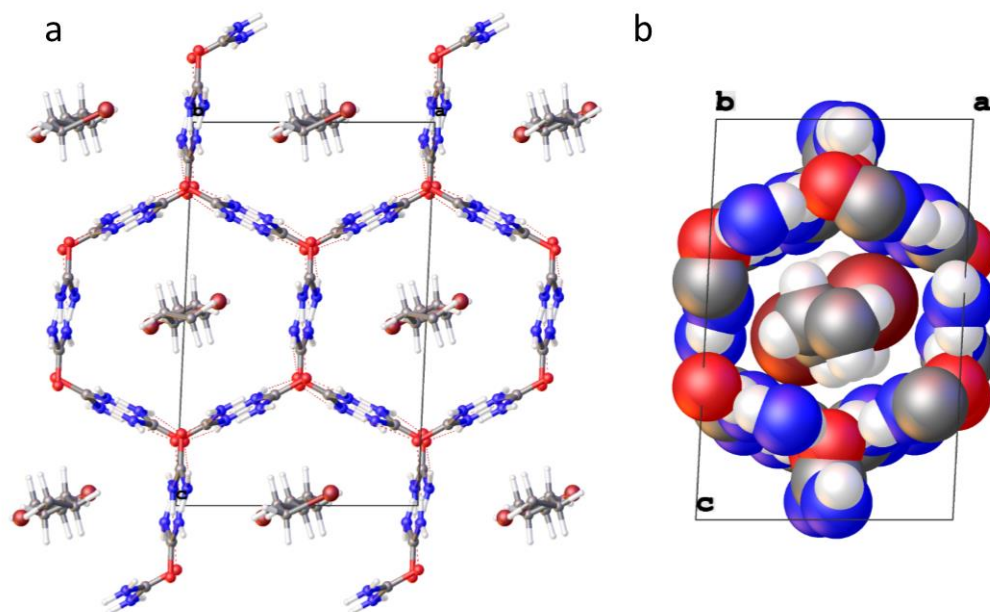


Figure 3-7. a) View down the *b* axis of 1,6-dibromohexane UIC with unit cell superimposed. b) Space filling representation of the unit cell.

The UIC of 1,6-dibromohexane stands out among UICs in general, as the guest has a commensurate relationship with the host network, despite having no hydrogen bonds between the guest and host. Within the channels, the 1,6-dibromohexane molecules are oriented in a gauche conformation,<sup>11</sup> overcoming the energy barrier associated with steric hindrance in order to avoid unfavourable Br...Br interactions between guest molecules. This conformation has a significant effect on the host structure, seen in Figure 3-7, as the channels are distorted relative to those seen in HEX, in order to accommodate the bromo substituents. This results in a monoclinic structure (Table 3-1).

### 3.3.3 Urea 2,7-octanedione

The 2,7-octanedione UIC was first reported by Hollingsworth and co-workers in 1996.<sup>26</sup> Like 1,6-dibromohexane, the 2,7-octanedione guest has a commensurate

relationship with the urea network (Figure 3-8). The presence of the ketone functionalities contributes to hydrogen bonding between the guest and host, facilitated by the twisting of certain urea molecules away from the plane created by the channel walls. For a unit cell similar in size to that of the hexadecane UIC, this would break the hexagonal symmetry of the structure, but the periodicity of the twisted urea molecules is such that a  $P6_522$  space group is maintained, with an unusually long  $c$  axis of 76.3 Å as a result, incorporating 3.5 crystallographically independent urea molecules.<sup>27</sup> This provides a unique challenge for structure determination by neutron diffraction that was addressed by using an incident wavelength of 1.4547 Å (Table 3-1). Figure 3-9 shows how urea molecules in the host walls break from the extended hydrogen bonding network to interact with the carbonyl oxygen of the guest. A hydrogen bond is formed by both NH groups of the molecule with guests in the channels either side, effectively creating a bridge between adjacent channels which is not present in the other UIC examples given here.

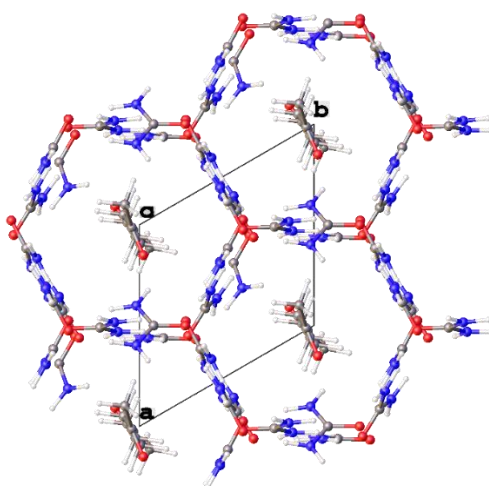


Figure 3-8. View down  $c$  axis of 2,7-octanedione UIC with unit cell superimposed.  $P6_522$   $a$ ,  $b$  = 8.1266(6),  $c$  = 76.297(6).



This motif which involves hydrogen bonding between the host and guest is seen for other guest compounds,<sup>26</sup> which have hydrogen bonding acceptor capability, and represents an alternate type of distortion from the conventional HEX type structure than is seen in DBH and other examples. Instead of a larger-scale supramolecular distortion which alters the channel shape, discrete urea molecules are tilted away from the larger network, bonding with the guest molecule and facilitating commensurate inclusion (Figure 3-9).

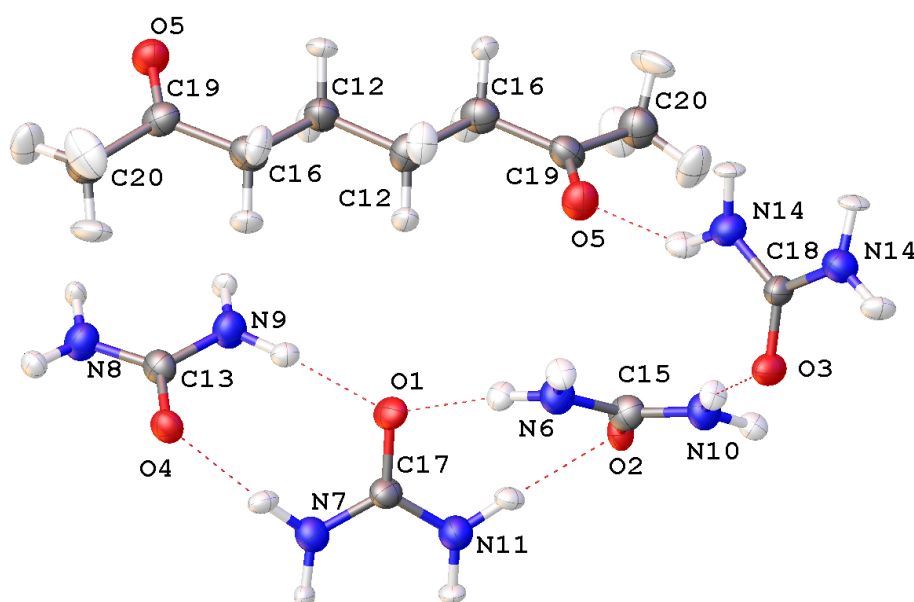


Figure 3-9. Hydrogen bonding between host and guest in OCT.

### 3.3.4 Urea – DMF co-crystal

Urea and DMF co-crystallise in a 3:1 ratio, not as a typical  $\beta$ -phase channel inclusion compound but as a stoichiometric co-crystal, first reported by Fernandes *et al* in 2007.<sup>14</sup> DMF does not meet the requirements of a potential UIC guest as it is too

branched and does not contain a long aliphatic chain. The DMF carbonyl oxygen forms a hydrogen bond with two neighbouring urea molecules with  $H\cdots O$  distances of 1.907(4) and 1.966(3) Å at 30 K. The unit cell of UDM displays a hydrogen bonding pattern between the urea molecules which is similar to that in HEX and other UICs. In effect, the structure comprises small sections of a UIC –type bonded urea network which are ‘interrupted’ by the DMF carbonyl oxygen atom. The packing and bonding of UDM can be seen in Figure 3-10, and is discussed further below.

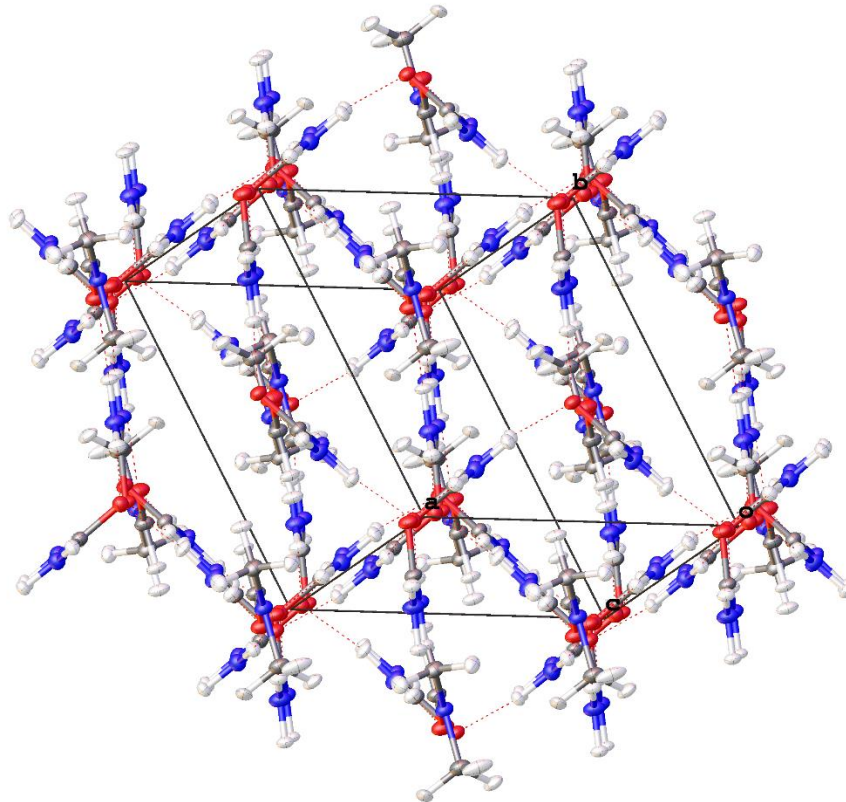


Figure 3-10. Pseudo-hexagonal packing of UDM, with unit cell superimposed.

### 3.3.5 High pressure studies

In order to ascertain whether the application of high pressure could result in a change of the symmetry of the UIC systems as a result of increasing the significance of the guest host interactions, the UICs HEX, DBH, OCT and the co-crystal UDM were studied under high pressure using a diamond anvil cell.<sup>17, 28, 29</sup> HEX, DBH and UDM displayed the conventional compression in unit cell axes and volume which occurs on application of pressure. Crystals of OCT were not resilient to applied pressure, and degraded above 0.71 kbar. As such only one unit cell was collected for OCT. Pressures and the associated unit cells are given in Table 3-2. Above these pressures, the crystals degraded to the point where single crystal diffraction was no longer possible.

**Table 3-2. Unit cells collected at high pressure**

	Pressure/ kbar	$a/\text{\AA}$	$b/\text{\AA}$	$c/\text{\AA}$	$V/\text{\AA}^3$
HEX	Ambient (150 K)	8.1529(5)	8.1529(5)	10.9819(6)	632.2(1)
	2.44	8.190(3)	8.190(3)	10.996(4)	638.7(4)
	5.17	8.116(3)	8.116(3)	10.944(4)	624.3(4)
DBH	Ambient (120 K)	8.5793(6)	10.8922(8)	13.4160(12)	1252.2(2)
	0.50	8.624(2)	10.935(2)	13.664(3)	1287.5(5)
	2.14	8.597(2)	10.872(2)	13.416(3)	1252.4(4)
OCT	Ambient (30 K)	8.1007(5)	8.1007(5)	76.213(5)	4331.1(5)
	0.71	8.115(10)	8.115(10)	76.04(9)	4336(9)
UDM	Ambient (30 K)	7.3797(2)	9.9588(3)	10.9509(2)	671.68(3)
	0.32	7.76(3)	9.829(7)	10.712(10)	710(3)
	4.87	7.621(11)	9.836(11)	10.691(11)	695.9(14)

It is worth noting that the volumes listed in Table 3-2 are larger than those seen in the neutron data reported here, as all high pressure diffraction data was collected at ambient temperature.

From the data given in Table 3-2, we can see that HEX, DBH and UDM undergo a compression of 2.3, 2.7 and 2.0% for a pressure change of 2.73, 1.64 and 4.55 kbar, respectively. UDM appears to be the least compressible of the structures, despite having the marginally largest void space of the systems studied. All of the structures have similar occupied space percentages, shown in Table 3-3, calculated using the default settings for void space calculation of OLEX2; resolution 0.2 Å, distance 0.0 Å.<sup>16</sup> None of the structures exhibited any pressure-induced phase changes.

**Table 3-3. Occupied space for all structures.**

Structure	Occupied space ambient pressure/ %	Unit cell compression/ %
HEX 150 K	65.1	2.3
DBH 120 K	67.6	2.7
OCT 30 K	64.6	-
UDM 120 K	62.6	2.0

### 3.4 Discussion

#### *Crystallisation of urea/2,7-octanedione*

Initial crystallisation attempts to obtain large crystals of OCT suitable for neutron diffraction were carried out by slow cooling. A ratio of 1:6 urea: 2,7-octanedione was used, in a concentrated MeOH solution at 60°C. The vial containing the solution

was placed in a covered Dewar flask surrounded by water at 60°C. The crystals obtained were orange in colour (likely as a result of trace impurities), and consistently multiply twinned, although their hexagonal habit was still in evidence (Figure 3-11). Interestingly, the crystals often break in an unusual way, with an edge portion of one or more hexagonal face of the crystal coming away when agitated suggesting an 'onion skin' type of multiple crystal.

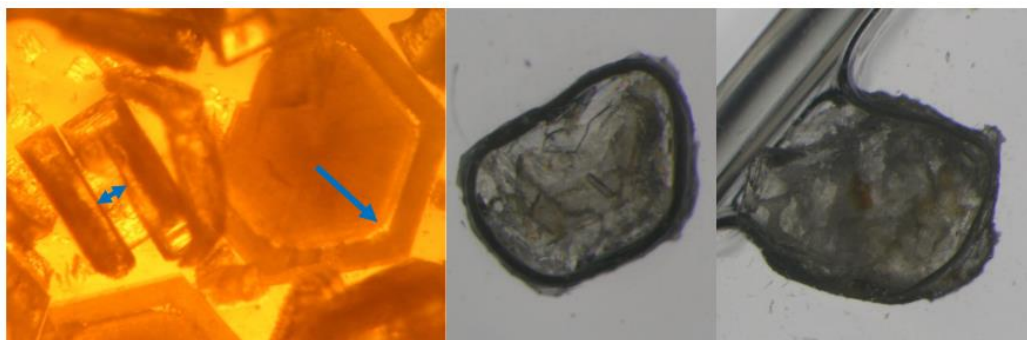


Figure 3-11. (Left) Crystals from initial crystallisation attempts of OCT. The arrows indicate where the crystal layers are separating. (Right) Crystals obtained using the TEC.

When a suitably large single crystal of OCT was obtained, data were collected with both X-ray and neutron diffraction methods. A structure solution could be obtained from the X-ray data, albeit with poor refinement indicators. Neutron data collected on a large crystal from the initial crystallisation attempts at SXD at ISIS, Didcot, UK gave a very poor refinement against the model obtained from X-ray diffraction. A dual refinement was attempted, fixing the non-hydrogen atom positions obtained from the X-ray model, and then refining against the neutron data to locate hydrogen atoms. However the resulting structure was of low precision. The combination of poor crystal quality and the very large  $c$  unit cell parameter of OCT of 76.3 Å make this a particularly challenging system.

In order to have more precise control over the crystallisation conditions a heating/cooling Peltier thermoelectric cooler (TEC) was designed to allow highly controlled cooling without the apparent multiple crystallisation stages suggested by the previously grown samples. A concentrated methanol solution of urea and 2,7-octanedione was cooled from 50°C to 12°C over a period of 4 days and held at 12°C for a further 2 days to optimize crystal size. This resulted in well-formed single crystals of around 8.9 mm<sup>3</sup> volume suitable for single crystal neutron diffraction (see experimental section). Regardless of crystallisation conditions, all OCT crystals showed degradation over time once removed from the mother liquor.

**Table 3-4. Hydrogen bonding parameters for HEX at 150 K, and DBH, OCT and UDM at 30 K, determined from neutron diffraction data.**

	Donor	Hydrogen	Acceptor	D-H/Å	H...A/Å	D...A/Å	D-H...A/°
HEX150	N2	H2A	O1	1.010(4)	1.965(4)	2.9460(19)	163.0(4)
	N2	H2B	O1	1.006(4)	2.009(4)	3.0096(16)	172.5(5)
DBH30	N3	H3A	O8	1.0123(17)	1.9829(19)	2.9934(9)	175.85(18)
	N3	H3B	O10	1.0095(17)	2.0319(19)	2.9991(10)	159.67(16)
	N4	H4A	O10	1.0130(17)	1.9648(18)	2.9704(9)	171.49(17)
	N4	H4B	O8	1.0138(17)	1.9321(18)	2.9227(9)	164.83(15)
	N6	H6A	O2	1.0108(17)	1.9564(18)	2.9580(9)	170.49(17)
	N6	H6B	O10	1.0117(18)	1.9586(19)	2.9395(10)	162.56(15)
	N7	H7A	O10	1.0091(17)	1.9747(19)	2.9740(9)	170.17(18)
	N7	H7B	O2	1.0159(18)	1.979(2)	2.9632(10)	162.28(16)
	N11	H11A	O2	1.0123(16)	1.9850(18)	2.9864(9)	169.69(16)
	N11	H11B	O2	1.0071(18)	2.0145(19)	2.9928(10)	163.19(15)
	N12	H12A	O8	1.0106(16)	1.9894(18)	2.9893(9)	169.75(17)

Urea Inclusion Compounds

	N12	H12B	O8	1.0101(17)	1.9321(19)	2.9183(9)	164.61(16)
OCT30	N6	H6A	O1	1.003(19)	1.923(18)	2.918(9)	171.6(15)
	N6	H6B	O4	0.997(14)	1.920(14)	2.879(9)	160.3(13)
	N7	H7A	O4	0.99(2)	1.972(18)	2.952(9)	170.7(14)
	N7	H7B	O1	0.990(17)	2.031(15)	2.953(9)	154.3(11)
	N8	H8A	O3	0.973(18)	2.052(16)	3.016(7)	170.6(14)
	N8	H8B	O2	0.982(17)	1.929(15)	2.894(9)	167.2(11)
	N9	H9A	O1	0.989(19)	1.949(18)	2.936(9)	175.1(13)
	N9	H9B	O1	0.998(15)	2.003(14)	2.937(9)	154.7(11)
	N10	H10A	O2	0.98(2)	1.963(18)	2.939(9)	175.5(12)
	N10	H10B	O3	0.998(13)	1.973(12)	2.938(7)	161.9(11)
	N11	H11A	O2	1.001(19)	2.031(17)	3.018(9)	168.4(14)
	N11	H11B	O4	1.000(15)	1.897(15)	2.890(9)	171.2(14)
	N14	H14A	O5	0.98(2)	2.10(2)	2.969(10)	146.2(14)
	N14	H14B	O2	1.007(15)	1.971(15)	2.939(9)	160.5(14)
UDM30	N4	H4A	O2	1.010(3)	1.893(3)	2.8957(18)	171.5(3)
	N4	H4B	O1	1.009(3)	1.891(3)	2.8334(17)	154.2(3)
	N5	H5A	O3	1.009(3)	1.919(3)	2.9195(17)	170.5(3)
	N5	H5B	O2	1.010(3)	2.290(4)	3.1255(18)	139.2(3)
	N6	H6A	O3	1.009(3)	1.917(3)	2.9088(18)	166.9(3)
	N6	H6B	O1	1.003(3)	2.231(4)	3.0567(18)	138.7(3)
	N7	H7A	O2	1.005(3)	1.883(3)	2.8746(18)	168.5(3)
	N7	H7B	O9	1.000(3)	1.966(3)	2.9634(19)	175.4(3)
	N12	H12A	O9	1.014(3)	1.907(4)	2.921(2)	178.3(3)
	N12	H12B	O2	1.000(3)	1.966(4)	2.8990(18)	154.2(3)
	N13	H13A	O1	1.011(3)	1.869(3)	2.8755(17)	173.1(3)
	N13	H13B	O1	1.004(3)	1.973(4)	2.8785(18)	148.7(3)

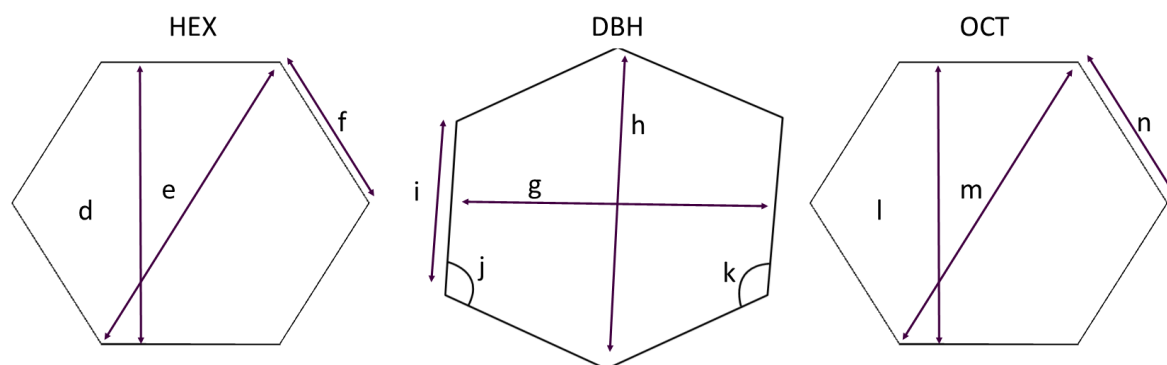


Figure 3-12. Diagrammatic representations of channel cross-sections and associated lengths/angles for the UIC series (left to right) with guests hexadecane, 1,6-dibromohexane and 2,7-octanedione.

Table 3-5. Parameters of hexagonal cross-section for each UIC.

HEX 150 K	DBH 30 K	OCT 30 K
$d = 8.15 \text{ \AA}$	$g = 8.58 \text{ \AA}$	$l = 8.10 \text{ \AA}$
$e = 9.41 \text{ \AA}$	$h = 9.97 \text{ \AA}$	$m = 9.35 \text{ \AA}$
$f = 4.71 \text{ \AA}$	$i = 4.98 \text{ \AA}$	$n = 4.68 \text{ \AA}$
$\text{area} = 57.64 \text{ \AA}^2$	$j = 117.4^\circ$	$\text{area} = 56.90 \text{ \AA}^2$
	$k = 122.6^\circ$	
	$\text{area} = 64.43 \text{ \AA}^2$	

The values given in Figure 3-12 and Table 3-5 show the variation in channel structure between UICs of different guest compounds, DBH in particular stands out, with a larger channel size than its higher symmetry counter-parts. The diameter of the channels in HEX and OCT are similar at 8.15 and 8.10 Å, respectively, whereas DBH has a channel diameter of 8.58 Å. The length of one 'edge' of the DBH channel is also larger, at 4.98 Å compared to 4.71 for HEX and 4.68 for OCT. The channels show a reasonable progression in size relative to the size and shape of the guest molecules – hexadecane has the smallest van der Waals radius, followed by 2,7-



octanedione and then the significantly larger 1,6-dibromohexane. However, there is no significant change in the average hydrogen bond lengths and distances between the examples (Table 3-6).

**Table 3-6. Average hydrogen bond parameters for HEX, DBH, OCT and UDM from neutron data.**

	Temperature/K	D-H/Å	H...A/Å	D...A/Å	D-H...A/°
HEX	150	1.01	1.99	2.978	167.8
HEX	260	1.00	1.98	2.929	163.2
DBH	30	1.01	1.98	2.967	167.1
DBH	120	1.01	1.99	2.982	167.0
DBH	260	1.00	2.01	2.991	166.8
OCT	30	0.99	1.98	2.941	164.9
UDM	30	1.01	1.98	2.929	161.6
UDM	120	1.00	2.00	2.946	161.9

Although there is little difference in the average hydrogen bond distances and angles between HEX and DBH, differences can be seen in individual hydrogen bonds. For DBH, the hydrogen bond associated with the acute angle of the hexagonal channel, N3-H3B...O10, has the longest D-A distance and narrowest angle, 159.67(16) ° of the hydrogen bonds (Table 3-4). The neighbouring bond on the same corner N4-H4B...O8 has an angle of 164.83(15) °. Conversely, the bonds on the widest corner of the hexagonal channel cross section have larger angles of 175.85(18) and 171.49(17) ° for N3 and N4, respectively. These bond angles fall within the same range as those seen in the highly symmetric HEX structure, however their distribution within the network, relative to the distortion in the

channels, shows how the finer aspects of hydrogen bonding in these systems are affected by the guest exerting an internal pressure on the host.

The UIC of (*E,E*)-1,4-diiodo-1,3-butadiene (DIBD) offers an example of host distortion resulting from guest conformation, similar to that seen in DBH.<sup>30</sup> The guest molecule in this instance is planar, the iodine atoms are twisted away from the carbon atom plane by only 1°. As such, no significant conformational distortions are required in order for DIBD to be accommodated by the urea network, however the host structure is still distorted slightly from the hexagonal symmetry seen in HEX and has the space group  $P2_1/n$ .

The distortion seen in DBH is similar to that of the low temperature phase of the hexadecane analogue,<sup>24</sup> in which the  $6_1$  screw axis is lost in a hexagonal to orthorhombic transition, as the host lattice is seemingly elongated in one direction. The corner-to-corner distance of HEX goes from 9.41 Å at 150 K to 9.70 Å at 120 K. This is associated with a reduction in the dynamic disorder of the hexadecane guest, albeit not to the extent that it can be modelled. This distortion is more exaggerated in DBH where this distance is 9.97 Å.

Table 3-6 includes the average hydrogen bond values for all neutron structures collected, including the varied temperatures. Most UICs undergo a temperature dependent phase transition including HEX, as discussed previously.<sup>31</sup> DBH, OCT and UDM do not undergo phase transitions in the temperature ranges discussed here, but DBH has a phase transition at 63°C to a hexagonally symmetric structure phase.<sup>11</sup> The D...A distances of HEX, DBH and UDM tend to be slightly longer at

higher temperature, or show no change. HEX seems to be the most susceptible to changes in temperature, with a larger change on average to the D...A bond distances, although this is still only a change of 0.04 Å between 150 and 260 K. The most significant change in an individual bond occurs in DBH where the D...A distance of the hydrogen bond N6-H6B...O1, between two urea molecules, increases by 0.04 Å.

The hydrogen atom positions from the neutron diffraction data show that the N-H bonds in certain locations deviate significantly from the typical planarity of a urea molecule in order to form the motif which creates the walls of the host network. A visual comparison is shown in Figure 3-13, showing an in-plane view of the hydrogen bonding involving protons H11B and H12B, which are *anti* to the carbonyl group. In the structure determined from X-ray data, the atom positions are assigned according to standard geometries, consistent with the planarity of the urea molecule. Figure 3-13 however, shows that *anti*-hydrogen atoms are twisted away from the N-C-N plane in order to bond, in this case with oxygen atoms O2 and O8. The same is true for the H3A-N3-C1-N4 torsion angle, at 169.7(2) °.

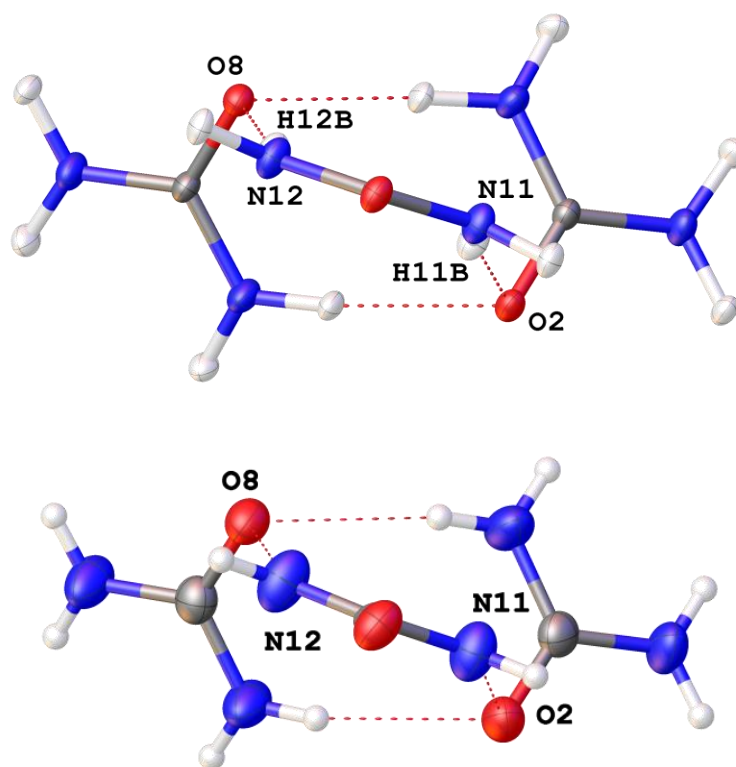


Figure 3-13. Structure of DBH derived from neutron data at 30 K (top) and X-ray data at 120 K (bottom) showing the difference in hydrogen atom positions from the two methods.

Table 3-7. Torsion angles of all bonding hydrogen atoms in DBH at 30 K, using N-C-N to define the plane of the associated urea molecule.

H3A	169.7(2)	H7A	177.5(5)
H3B	5.1(3)	H7B	2.0(1)
H4A	173.4(2)	H11A	171.8(2)
H4B	8.1(2)	H11B	15.1(2)
H6A	178.5(2)	H12A	173.8(2)
H6B	0.3(2)	H12B	3.3(2)

In the tetragonal  $\alpha$ -form of urea, the equivalent torsion angles are  $0^\circ$ , as one would expect from a planar molecule.<sup>32</sup> In the HEX UIC, the equivalent torsional angles are  $176.7(3)$  and  $1.7(3)^\circ$  respectively. Those for urea 1,6-dibromohexane are detailed in Table 3-7.

The same twisting of urea can be seen in OCT, as the urea bonded with the 2,6-octanedione guest has a greater intramolecular torsion angle than that of neighbouring urea molecules. The effect is less than seen for DBH, but a torsional angle of 11.5(11) ° is still seen for the urea bonded to the guest molecule (Table 3-8).

**Table 3-8. Torsion angles of bonding hydrogen atoms in OCT at 30 K.**

H6A	178.3(12)	H9A	174.4(11)	H14A	179.2(13)
H6B	7.3(11)	H9B	3.6(16)	H14B	11.5(11)
H7A	177.9(11)	H10A	178.5(11)		
H7B	1.4(14)	H10B	2.1(11)		
H8A	170.8(12)	H11A	177.7(11)		
H8B	3.1(17)	H11B	4.8(14)		

Of the hydrogen bonds in OCT, N14-H14A-O5 has the most acute intramolecular bond angle at 146.2(14) °, as the urea molecule twists away from the host walls in order to interact with the guest carbonyl oxygen atom on each side, bridging individual channels.

The urea-DMF hydrogen bonds present in UDM are, on average, of shorter D...A distance than seen in any of HEX, OCT or DBH, at 2.929 Å (Table 3-6). Additionally, the angles throughout the structure tend to be more acute. One structural feature present in UDM which is not seen in the UICs is a type of corrugated urea  $\alpha$ -tape, which creates anti-parallel tapes of urea which contribute to the appearance of hexagonal character (Figure 3-14).

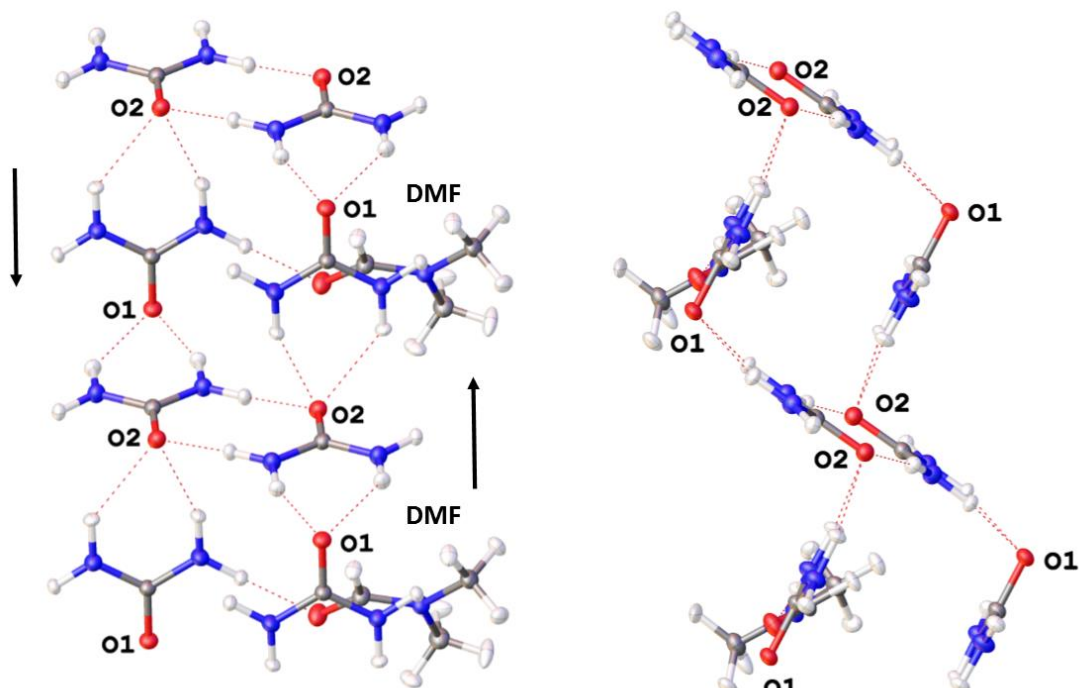


Figure 3-14. Pseudo  $\alpha$ -urea tape in UDM from two viewpoints.

There is a hydrogen bonding motif present in UDM between two independent urea molecules and DMF. Completed by the inversion centre of structure, these create a bonding pattern which closely resembles that found in HEX, forming a portion of the channel walls. In UDM, this section is effectively interrupted by DMF (Figure 3-15).

Hydrogen bonding data for UDM are shown in Table 3-4. Figure 3-15 shows the hydrogen bonding between urea molecules and DMF, which in this structure are closer to being in plane than in the equivalent motif in HEX. The hydrogen bonds to the DMF carbonyl oxygen atom are longer than any urea-urea bonds in the section shown. The bond N12-H13B $\cdots$ O1 has a particularly acute angle of  $148.7(3)^\circ$  compared with the equivalent angle in HEX of  $172.5(5)^\circ$ .

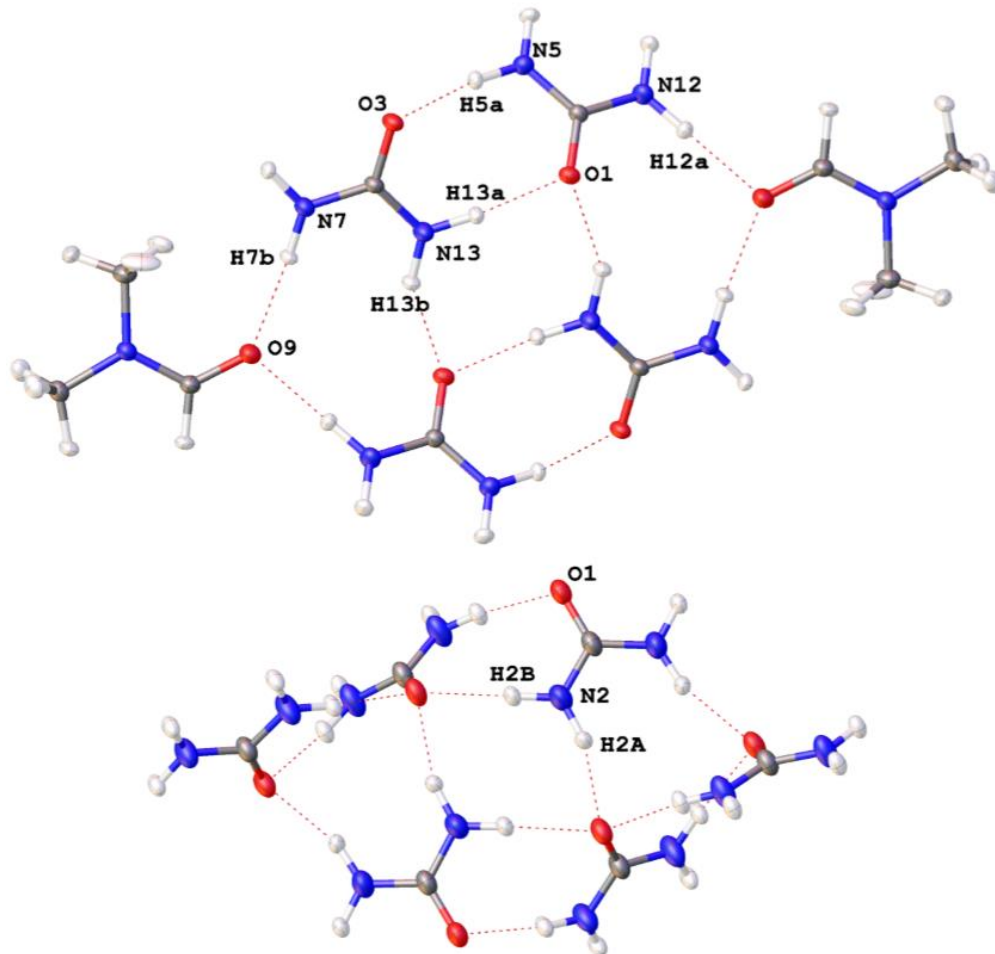


Figure 3-15. Hydrogen bonding motif in UDM (top) and HEX (bottom).

The UIC of sebaconitrile offers an interesting comparative example of an inclusion compound in which the typical channel structure is disrupted, similar to the effect seen in UDM but in this case maintaining the channel structure of a UIC. In urea/sebaconitrile, segments of the urea host are offset from each other at the junction between adjacent guest molecules.<sup>33</sup> The potential for strong dipole-dipole interactions between adjacent guests would predict a more conventional UIC structure, but the molecules do not fall within van der Waals contact, instead the

nitrile groups are hydrogen bonded to two urea molecules in the neighbouring channel section, similar to the channel bridging seen in OCT, as the guest bonds with urea host molecules. This sebaconitrile UIC, with space group  $C2/c$ , has similarities with the monoclinic DBH, as hexagonal symmetry is sacrificed in order to accommodate the guest within the channels. Additionally, the channel structure itself is altered significantly compared to HEX, having parallels to the disrupted urea bonding pattern in UDM.

### 3.5 Conclusions

Perturbations arise in urea inclusion compounds as a result of guest molecule shape, size and bonding capabilities. The size and nature of the guest play a vital role in whether or not an inclusion compound is formed and have a significant influence on the channel structure and host-guest relationship.

Bonding capability influences UIC structure, as guests which are able to form hydrogen bonds may interrupt the urea network and effectively be incorporated into the host structure *via* hydrogen bonding, while still occupying the channel space, resulting in a commensurate host-guest relationship. In the absence of such hydrogen bonding groups, or other particular characteristic, there will be an incommensurate host-guest relationship and the guest position will be unresolved in one dimension.

We have further emphasized the value of neutron diffraction techniques in investigating the nuances of hydrogen bonded systems, as crystal structures determined solely by X-ray diffraction techniques may be missing some of the finer



details and subtleties of hydrogen bonded structures. With appropriate techniques neutron quality crystals of even very challenging systems such as OCT can be prepared and studied using modern instrumentation.

Overall, the urea inclusion compound host framework is quite adaptable and significant distortions can be tolerated without significant changes in the hydrogen bond metrics. Distortion of the hexagonal channels can be seen in the shortening and lengthening of hydrogen bonds relative to their position within the network, as seen in DBH, but no significant perturbation from the classic hexagonal channel of HEX is required to accommodate guests of different types. 2,7-octanedione is readily incorporated into a UIC, with a particularly long H...A distance 2.052(16) Å and acute DHA angle 146.2(14)° relative to bonds in other UICs, highlighting the versatility of the network, and preference for commensurate inclusion when an appropriate guest is present.

### 3.6 References

See DOI: 10.5291/ILL-DATA.5-12-308 and 10.5291/ILL-DATA.5-12-318 for neutron diffraction data.

1. F. Bengen, W. Schlenk, *Cell. Mol. Life Sci.* 1949, **5**,
2. A. E. Smith, *Acta Crystallogr.* 1952, **5**, 224-235.
3. F. Imashiro, T. Maeda, T. Nakai, A. Saika, I. Terao, *J. Phys. Chem.* 1986, **90**, 5498-5500.
4. K. D. M. Harris, S. P. Smart, M. D. Hollingsworth, *J. Chem. Soc., Faraday Trans.* 1991, **87**, 3423-9.
5. M. E. Brown, J. D. Chaney, B. D. Santarsiero, M. D. Hollingsworth, *Chem. Mater.* 1996, **8**, 1588-1591.
6. R. Forst, H. Jagodzinski, H. Boysen, F. Frey, *Acta Crystallogr., Sect. B: Struct. Sci.* 1990, **46**, 70-78.
7. S. Zerdance, C. Mariette, G. J. McIntyre, M. -H. Lemee-Cailleau, P. Rabiller, L. Guerin, J. C. Ameline, B. Toudic, *Acta Crystallogr., Sect. B: Struct. Sci.* 2015, **71**, 293-299.
8. Y. Chatani, Y. Taki, H. Tadokoro, *Acta Crystallogr., Sect. B: Struct. Sci.* 1977, **33**, 309-311.

9. A. J. O. Rennie, K. D. M. Harris, *P. Roy. Soc. Lond. A Mat.* 1990, **430**, 615-640.
10. M. E. Brown, M. D. Hollingsworth, *Nature* 1995, **376**, 323-327.
11. M. D. Hollingsworth, U. Werner-Zwanziger, M. E. Brown, J. D. Chaney, J. C. Huffman, K. D. M. Harris, S. P. Smart *J. Am. Chem. Soc.* 1999, **121**, 9732-9733.
12. L. Yeo, K. D. M. Harris, *Acta Crystallogr., Sect. B: Struct. Sci.* 1997, **53**, 822-830.
13. Yeo, L.; Harris, K. D. M. *Can. J. Chem.* 1999, **77**, 2105-2118.
14. P. Fernandes, A. J. Florence, F. Fabbiani, W. I. F. David, K. Shankland, *Acta Crystallogr., Sect. E: Struct. Rep. Online* 2007, **63**, o4861.
15. G. Sheldrick, *Acta Crystallogr. Sect. C: Cryst. Struct. Commun.* 2015, **71**, 3-8.
16. O. V. Dolomanov, L. J. Bourhis, R. J. Gildea, J. A. K. Howard, H. Puschmann, *J. Appl. Crystallogr.* 2009, **42**, 339-341.
17. R. Lee, J. A. K. Howard, M. R. Probert, J. W. Steed, *Chem. Soc. Rev.* 2014, **43**, 4300-4311.
18. G. J. Piermarini, S. Block, J. D. Barnett, R. A. Forman, *J. Appl. Phys.* 1975, **46**, 2774-2780.
19. M. R. Probert, J. A. Coome, A. E. Goeta, J. A. K. Howard, *Acta Crystallogr., Sect. A: Found. Crystallogr.* 2011, **67**, C528.
20. M. R. Probert, C. M. Robertson, J. A. Coome, J. A. K. Howard, B. C. Michell, A. E. Goeta, *J. Appl. Crystallogr.* 2010, **43**, 1415-1418.
21. T. Schulz, K. Meindl, D. Leusser, D. Stern, J. Graf, C. Michaelsen, M. Ruf, G. M. Sheldrick, D. Stalke, *J. Appl. Crystallogr.* 2009, **42**, 885-891.
22. R. Forst, H. Jagodzinski, H. Boysen, F. Frey, *Acta Crystallogr., Sect. B: Struct. Sci.* 1987, **B43**, 187-97.
23. K. D. M. Harris, *J. Phys. Chem. Solids* 1992, **53**, 529-537.
24. L. Yeo, B. M. Kariuki, H. Serrano-Gonzalez, K. D. M. Harris, *J. Phys. Chem. B* 1997, **101**, 9926-9931.
25. K. Fucke, A. J. Edwards, M. R. Probert, S. E. Tallentire, J. A. K. Howard, J. W. Steed, *ChemPhysChem* 2013, **14**, 675-679.
26. M. E. Brown, J. D. Chaney, B. D. Santarsiero, M. D. Hollingsworth, *Chem. Mater.* 1996, **8**, 1588-1591.
27. K. M. Steed, J. W. Steed, *Chem. Rev.* 2015, **115**, 2895-2933.
28. A. Katrusiak, *Acta Crystallogr., Sect. A: Found. Crystallogr.* 2008, **64**, 135-148.
29. E. Boldyreva, *Acta Crystallogr., Sect. A: Found. Crystallogr.* 2008, **64**, 218-231.
30. A. F. Lashua, T. M. Smith, H. Hu, L. Wei, D. G. Allis, M. B. Sponsler, B. S. Hudson, *Cryst. Growth Des.* 2013, **13**, 3852-3855.
31. K. D. M. Harris, *Chem. Soc. Rev.* 1997, **26**, 279-289.
32. S. Swaminathan, B. M. Craven, R. K. McMullan, *Acta Crystallogr., Sect. B: Struct. Sci. B* 1984, **40**, 300-306.
33. M. D. Hollingsworth, B. D. Santarsiero, K. D. M. Harris, *Angew. Chem. Int. Ed.* 1994, **33**, 649-652.

# Chapter 4 Expanding the pyridine-formic acid co-crystal landscape under extreme conditions

---

## 4.1 Introduction

Herein, we investigate a series of co-crystals composed of pyridine and formic acid. Of these, the structures of the 1:1 and 1:4 co-crystals have been previously reported at low temperature and ambient pressure.<sup>1</sup> Pyridine-formic acid is a system which displays a strong O-H $\cdots$ N hydrogen bond, however the degree of proton transfer can be manipulated by the addition of further equivalents of formic acid; as the relative concentration of polar components increases, the O-H $\cdots$ N bond gradually increases in strength until proton transfer occurs.<sup>2</sup> This results in a system with different bonding types and motifs to the original system, which may have a significant effect on HP/LT polymorphism of this series. The pyridine formic acid system was chosen for study due to its well-documented concentration dependent stoichiomorphism. Any deficiency in knowledge of the extent of their behaviour and bonding capabilities can be seen as an oversight. Small molecule weak acid-base interactions are a classic example of a hydrogen-bonding motif seen in supramolecular chemistry, and the pyridine-formic acid mixture presented a simple and logical route to investigating such high-pressure crystal structure landscapes.

## 4.2 Experimental

New low temperature structures were obtained from *in situ* cryo-crystallisation.

Pyridine-formic acid mixtures were loaded into a 0.3 mm borosilicate glass capillary, which was sealed at both ends, attached to a pin and then mounted on the diffractometer. Both Bruker CCD SMART 6K and Agilent Xcalibur Gemini diffractometers were used each equipped with Oxford Cryosystems open flow nitrogen cryostats. A combination of cooling and flash freezing with liquid nitrogen was used to obtain a polycrystalline material, and crystals suitable for diffraction were obtained by temperature cycling just below the melting point of the crystals. Above the melting point, all the crystals returned to the liquid phase.

High-pressure structures were obtained by *in situ* compression in a diamond anvil cell (DAC). A 0.25 mm thickness steel gasket, pre-indented to 0.15 mm, with a precision drilled 300  $\mu\text{m}$  hole created the sample chamber between the two diamond anvils, of culet size 0.8 mm. A ruby chip was included in the sample chamber for pressure determination. Pressure was applied until the sample gave a polycrystalline material, at which point the pressure was cycled around the melting transition at ambient temperature to give a single crystal. Given that no solvent was used, the crystal could be grown to fill the entire sample chamber. The diamond anvil cell was directly attached to a goniometer head and mounted on the diffractometer. Data were collected using the XIPHOS II<sup>3,4</sup> diffractometer at Newcastle University, a four-circle Bruker diffractometer with Ag-K $\alpha$   $1\mu\text{S}$  generator.<sup>5</sup> The pressure inside the cell was measured after equilibration by the R<sub>1</sub> ruby fluorescence method.<sup>6</sup> Data collection conditions are detailed in Table 4-1. HP data

were collected beyond the phase boundary by over-pressurising the cell to ensure the crystal remained stable during the experiment. On reduction of pressure, all crystals melted back to the liquid phase.

Data were handled in the Bruker APEX2<sup>7</sup> software suite with SAINT<sup>8</sup> and SADABS<sup>9</sup> used for integration, cell refinement and scaling. Dynamic masks were generated using the program ECLIPSE<sup>10</sup>. The Olex2<sup>11</sup> interface for the SHELX<sup>12</sup> program suite was used for structure solution and refinement. All hydrogen atoms on heteroatoms were located in Fourier difference maps.

### 4.3 Results and Discussion

Pyridine and formic acid co-crystallise at HP in the ratios 1:1, 1:2 and 1:4. LT structures are already known for the 1:1 and 1:4 mixtures.<sup>1</sup> The 1:1 co-crystal adopts the same form at both LT and at HP (9.2 GPa); however different polymorphs were obtained for the 1:4 mixture at LT (200 K) and HP (14.2 kbar). No LT form could be isolated for the 1:2 mixture.

#### 4.3.1 Pyridine Formic acid 1:1

A 1:1 mixture of pyridine and formic acid crystallises in space group  $P2_1/n$ . The crystals obtained from pressurisation and cryo-crystallisation adopt the same crystal packing arrangement, the principal structural difference being the packing density which was markedly higher for the HP phase (Table 4-3). The primary intermolecular interaction is an O-H $\cdots$ N hydrogen bond with a donor-acceptor distance of 2.663(3) Å in the LT structure. The structure exhibits  $\pi$ - $\pi$  stacking between equivalent pyridine molecules along the  $b$  axis. Defining a plane across individual molecules shows a centroid-centroid distance of 3.817(3) Å. These

centroids are offset from each other by 1.32(2) Å relative to the plane of the ring.

Adjacent stacks are offset from each other and form a layered motif in the *c* axis, with alternating layers of formic acid and pyridine molecules (Figure 4-1).

HP data for the 1:1 co-crystal were collected at 9.71 kbar. This was an over-pressurisation to prevent the crystal melting during data collection. Despite being the same polymorph, the structure at HP exhibits some changes in packing as a result of the applied pressure. The O-H $\cdots$ N hydrogen bond is compressed to a donor-acceptor distance of 2.63(1) Å. Similarly, the pyridine rings are forced closer together with the ring planes having a centroid-centroid distance of 3.647(1) Å with an offset of 1.240(4) Å. A summary of the hydrogen bonding is given in Table 4-1.

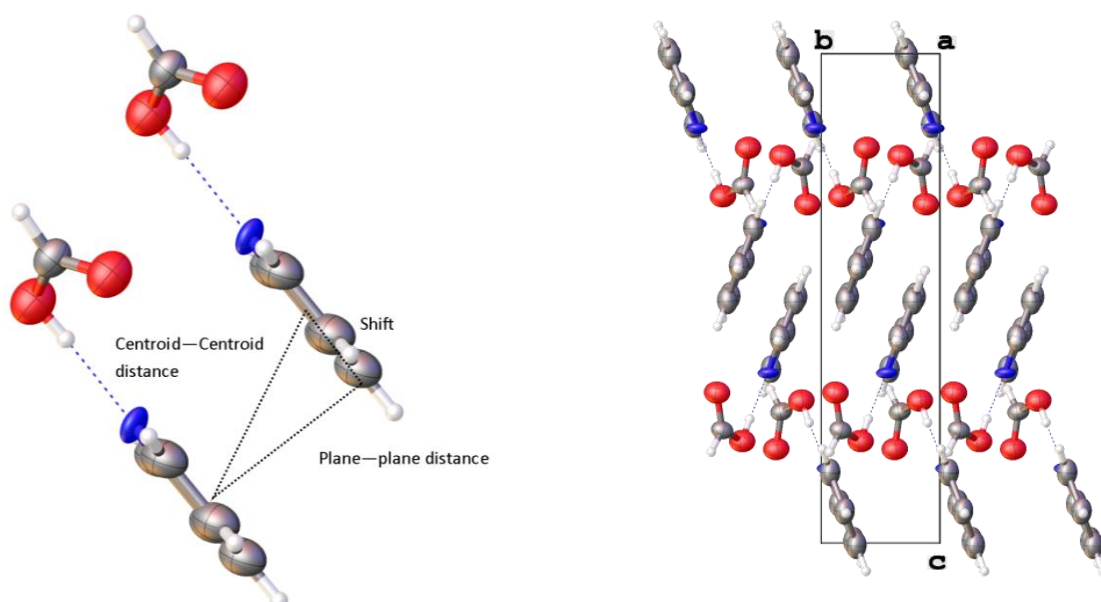


Figure 4-1. (Left) Stacking between pyridine rings showing how key parameters are defined. (Right) View down the *a* axis of pyridine formic acid 1:1, showing layers extending in the *c* axis direction.

Table 4-1. Hydrogen bond details for the unique hydrogen bond in a 1:1 co-crystal of pyridine formic acid.

Contact	Low temperature	High pressure
H-A (Å)	1.69(4)	1.81(1)
D-A (Å)	2.663(3)	2.63(1)
D-H (Å)	0.98(4)	0.82(1)
D-H-A (°)	172(4)	176.9(7)

### 4.3.2 Pyridine-Formic acid 1:2

The pyridine - formic acid 1:2 co-crystal was found to crystallise only by pressurisation of the liquid mixture; capillary crystallisation at LT afforded only a glass. The asymmetric unit contains one pyridinium ion, a formate ion and a formic acid molecule. Hence the structure is strictly a salt co-crystal of formic acid and pyridinium formate. The shortest intermolecular contacts comprise both N-H $\cdots$ O and O-H $\cdots$ O hydrogen bonds in a short chain of hydrogen interactions, shown in Figure 4-2.

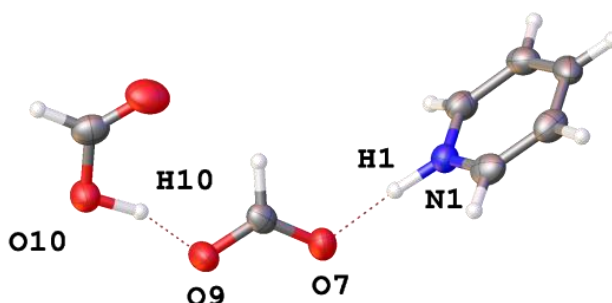
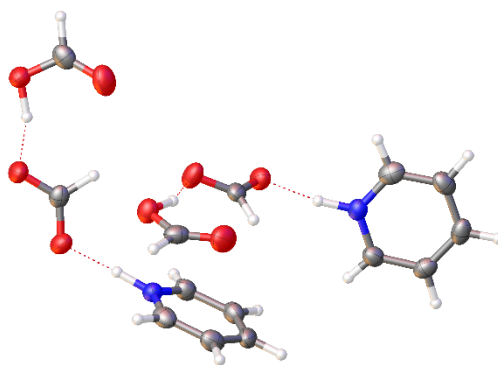


Figure 4-2. Asymmetric unit of pyridine-formic acid 1:2 (HP) showing the primary hydrogen bonding motif.

The pyridinium-formate interaction has a donor-acceptor distance of 2.647(3) Å (see Table 4-2), compared to 2.634(12) Å for the HP 1:1 co-crystal. There is little

difference in the  $N\cdots O$  distances between the two structures, despite a significant change in the nature of the hydrogen bond between the molecules. The  $N-H\cdots O$  and  $C-H\cdots O$  interactions form a bonding motif confined to a single plane, as shown in Figure 4-3. The angle between the plane of the pyridinium ion, and the formate/formic acid pair is such that the hydrogen bonding network is propagated in three dimensions. Further interactions occur between the formate ion and the edge of the pyridinium ion, with each of the oxygen atoms exhibiting two  $C-H\cdots O$  interactions. The formic acid – formate charge-assisted hydrogen bond has D-A  $O\cdots O$  distance of 2.458(4) Å. The O-H bond of the formic acid is 1.05(6) Å, slightly longer than a conventional OH bond, indicating that the proton is partially shared between the two molecules, without any apparent disorder between two distinct positions.



**Figure 4-3. Hydrogen bonding interactions between pyridinium and formate ions in the HP 1:2 structure.**

An analogous structure of a pyridine - oxalic acid co-crystal has been reported which crystallises as dipyridinium bis(hydrogen-oxalate) oxalic acid, in which the pyridinium ion is hydrogen bonded to the hydrogen oxalate ion.<sup>13</sup> The primary hydrogen bond has a D-H distance of 1.00(3) Å, HA distance 1.97(3) Å and DA distance 2.792(3) Å. The longer bond distance indicates a slightly weaker



interaction, which is consistent with the larger size and hence greater delocalisation of the negative charge on the hydrogen oxalate anion compared with the formate ion in the pyridine-formic acid structure.

**Table 4-2. Details of N1-H1...O7 hydrogen bond contact in the high pressure structure of 1:2 pyridine-formic acid.**

Contact	High Pressure
H-A (Å)	1.62(4)
D-A (Å)	2.647(3)
D-H (Å)	1.04(3)
Angle (°)	171(4)

#### 4.3.3 Pyridine formic acid 1:4

As in the case of the 1:1 co-crystal, a 1:4 mixture of pyridine and formic acid crystallises under both HP and LT conditions. In this case, however, different polymorphs are obtained via the two methods. The LT form crystallises in orthorhombic space group  $Pca2_1$ , while in the HP form, the symmetry is reduced, giving space group  $P2_1$ . Figure 4-4 shows the view down the  $a$  axes for both the HP and LT polymorphs.

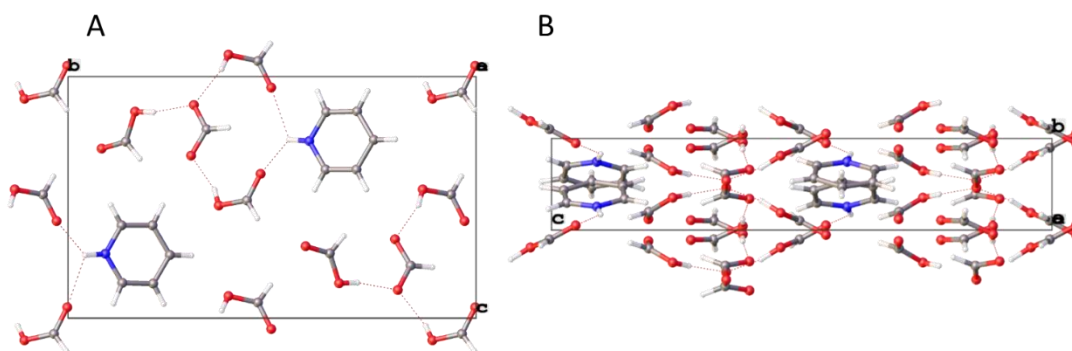


**Figure 4-4. View down the  $a$  axis of the 1:4 adduct. a) High pressure and b) low temperature.**

Both forms contain a pyridinium ion, with one formate ion and three formic acid molecules (Figure 4-5). In the LT form, there are two novel hydrogen bonds between the pyridinium hydrogen atom and two neighboring carbonyl oxygen atoms of formic acid molecules with D-A distances 2.870(3) and 3.019(4) Å. One of these formic acid molecules is 'bridging' a C-N bond in the pyridinium ring, with an O-H···H-C hydrogen bond adjacent to the C=O···H-N primary interaction. In the HP polymorph, this interaction is altered; there are still two hydrogen bonds involving the pyridinium N-H, but no seven-membered-ring style bonding pattern which is present in the LT form. These two interactions are with two carbonyl oxygen atoms from formic acid with D-A distances 2.853(10) and 3.105(9) Å.

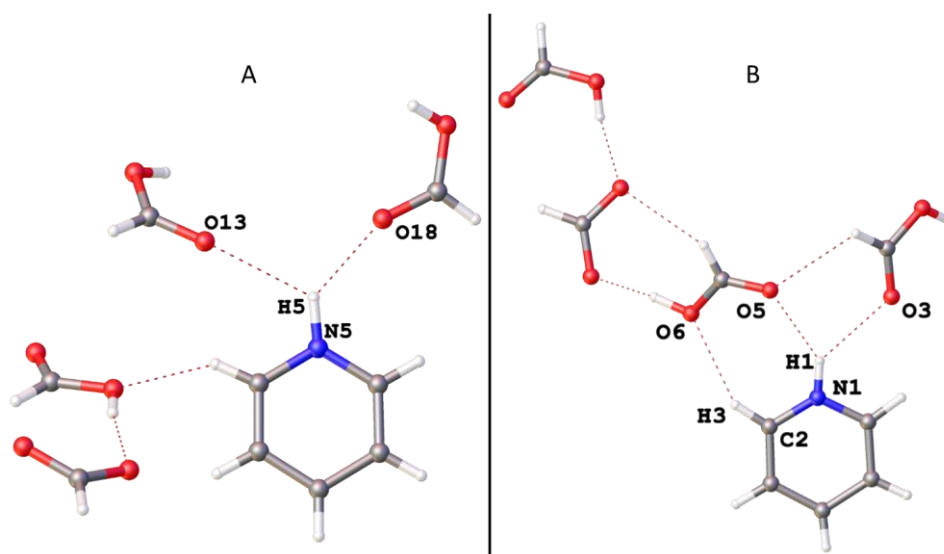


Figure 4-5. Asymmetric units of a) high pressure and b) low temperature polymorphs of pyridinium formate tris(formic acid).

The strong directional hydrogen bond which dominates the packing of the 1:1 structure is lengthened at the higher ratio of formic acid and HP. As proton transfer has occurred, the ion-ion interaction between pyridinium and formate ions becomes more dominant. Charge assisted hydrogen bond interactions are still seen

in both LT and HP 1:4 structures, but are weaker with longer bond distances, more oblique angles and bifurcated hydrogen bonding.

Ion-ion interactions are comparable in strength to covalent bonds with bond strengths 100-350 kJ mol<sup>-1</sup>. Hydrogen bonds are weaker with strengths in the range 4-60 kJ mol<sup>-1</sup> but are highly directional. The N...HO hydrogen bond in the 1:1 pyridine formic acid co-crystal qualifies as a moderate electrostatic hydrogen bond based on the D-A distances of 2.663(3) Å and 2.634(12) Å for the LT and HP versions, respectively.<sup>14, 15</sup> The distance of the charge assisted hydrogen bond in the 1:2 salt co-crystal is comparable at 2.647(3) Å. In the 1:4 case, for the LT polymorph, the NH<sup>+</sup>...O<sup>-</sup> bond has a D-A distance 2.870(3) Å. For the HP polymorph, the closest hydrogen contact is 2.853(10) Å. Close packing effects have greater dominance over the structure, and the components adopt a conformation which gives the structure a higher packing efficiency than the LT polymorph. A comparison of the occupied space calculated using the OLEX2 package for all structures is given in Table 4-3. In all cases, the higher pressure structure has the higher density packing.

There are  $\pi$ - $\pi$  stacking interactions present in both polymorphs of the 1:4 mixture and as expected, the minimum distance between pyridine rings in the HP structure, 3.560(1) Å, is shorter than the distance of 3.702(3) Å observed in the LT polymorph. The offset between the rings is also slightly smaller in the HP phase.

Table 4-3. Percentage of unit cell occupied by Py-FA structures.

Ratio	Low temperature	High pressure
1:1	67.51	72.13
1:2	-	76.36
1:4	69.36	73.66

Table 4-4. Summary of Crystallographic data.

	1:1 LT <sup>1</sup>	1:1 HP	1:2 HP	1:4 LT <sup>1</sup>	1:4 HP
Empirical formula	C <sub>6</sub> H <sub>7</sub> NO <sub>2</sub>	C <sub>6</sub> H <sub>7</sub> NO <sub>2</sub>	C <sub>7</sub> H <sub>9</sub> NO <sub>4</sub>	C <sub>9</sub> H <sub>18</sub> NO <sub>8</sub>	C <sub>9</sub> H <sub>13</sub> NO <sub>8</sub>
<i>T</i> / K	173	295	295	183	295
<i>P</i> / kbar	ambient	9.2(2)	10.9(2)	ambient	14.2(2)
Crystal system	Monoclinic	Monoclinic	Monoclinic	Orthorhombic	Monoclinic
Space group	<i>P2</i> <sub>1</sub> / <i>n</i>	<i>P2</i> <sub>1</sub> / <i>n</i>	<i>P2</i> <sub>1</sub> / <i>n</i>	<i>Pca2</i> <sub>1</sub>	<i>P2</i> <sub>1</sub>
<i>a</i> / Å	10.954(6)	10.760(2)	7.4036(4)	16.35(1)	3.560(1)
<i>b</i> / Å	3.817(3)	3.647(1)	13.380(2)	3.702(3)	16.533(5)
<i>c</i> / Å	15.842(7)	15.549(5)	8.2074(6)	20.23(1)	9.798(2)
$\beta$ / °	104.96(5)	104.15(2)	114.05(1)	90	93.78(1)
<i>Z</i>	4	4	4	4	2
<i>V</i> / Å <sup>3</sup>	639.9(7)	591.6(2)	742.5(1)	1224.5	575.4(2)
<i>D</i> <sub>c</sub> / gcm <sup>-3</sup>	1.30	1.41	1.53	1.43	1.52
Unique reflns.	1120	5497	6501	1835	2638
Completeness %	-	42	66	-	50
<i>R</i> <sub>1</sub>	0.047	0.071	0.050	0.041	0.041
<i>wR</i> <sub>2</sub>	0.167	0.209	0.134	0.114	0.093
Goof	-	1.17	1.05	-	1.08

#### 4.3.4 Proton transfer

As the proportion of formic acid present in the mixture reaches two equivalents, proton transfer occurs in the crystal structure, and persists as the ratio increases further. It has been previously reported that for such a hydrogen bonded system, increasing the acid: base ratio strengthens the  $AH\cdots B$  bond to the point of proton transfer.<sup>16</sup> There is evidence for this process also occurring in solution. In a low temperature NMR study of a pyridine-acetic acid mixture, increasing the relative concentration of acetic acid was found by Smirnov *et al.* to favour protonation of pyridine, although this could only be seen at temperatures below 120 K due to the high rate of proton exchange at ambient temperature.<sup>17</sup> This effect can be seen in the solid state also, in the pyridine-formic acid series; proton transfer occurs in the 1:2 adduct, with a  $N^+-H$  bond distance of 1.04(3) Å. In the 1:4 LT adduct, this bond has decreased in length to 0.87(5) Å, implying that the presence of an additional two formic acid molecules in the immediate environment further promotes the O-H-N proton transfer further localising the proton on the nitrogen atom. This effect warrants further investigation by single crystal neutron diffraction in order to fully resolve the hydrogen atom positions. Table 4-5 shows the bond distances for the primary pyridine-formic acid or pyridinium-formate hydrogen bond for each structure. Note that the donor and acceptor atoms change as proton transfer takes place.

Table 4-5. Hydrogen bond parameters for pyridine-formic acid series.

Ratio	D	H	A	DH/Å	HA/Å	DA/Å	DHA/°
1:1 HP	O7	H7	N1	0.821(8)	1.814(9)	2.634(12)	176.9(7)
1:2 HP	N1	H1	O7	1.04(4)	1.62(4)	2.647(3)	171(4)
1:4 LT	N1	H1	O7	0.87(5)	2.14(5)	2.870(3)	141(4)
1:4 HP	N5	H5	O18	0.99(8)	2.08(6)	2.853(10)	134(4)

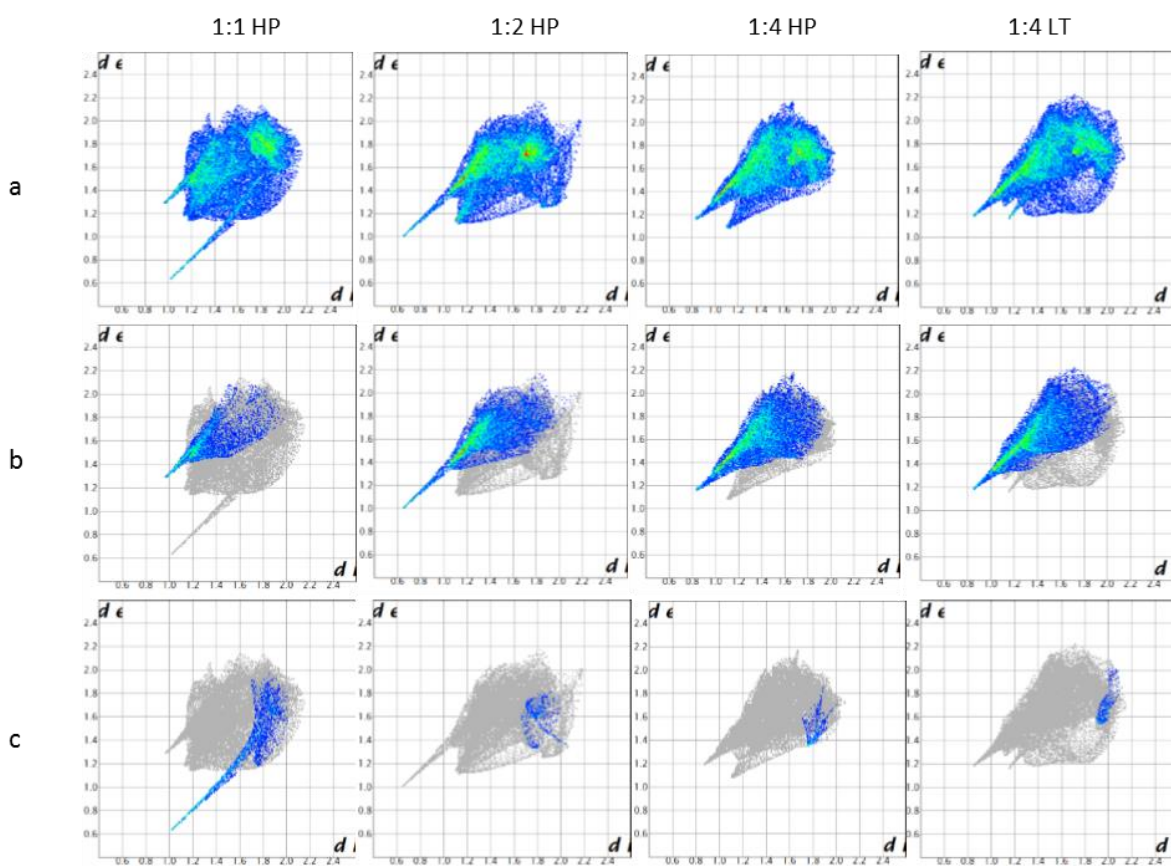


Figure 4-6. Hirshfeld 2D fingerprint plots of 1:1, 1:2, 1:4 HP and 1:4 LT crystal structures of pyridine-formic acid. a) Whole surface, b) OH interactions, c) NH interactions.

A useful tool for the analysis of the intermolecular contacts in a crystal structure is offered by the program Crystal Explorer, which can be used to generate Hirshfeld surfaces for molecules and also provides a 2D representation of these contacts called ‘fingerprint plots’.<sup>18, 19</sup> The compression of crystal structures at high pressure has been analysed in this way and shows the typical differences between LT and HP

structures. HP fingerprint plots tend to be more compressed, as contacts within the structures are also compressed, as well as tending towards higher symmetry about the  $d_i = d_e$  diagonal.<sup>20</sup> Surfaces and fingerprint plots were generated for the pyridine/pyridinium in each of the structures 1:1, 1:2, 1:4 HP and 1:4 LT where  $d_e$  is the distance between the Hirshfeld surface and nearest contact external to the surface, and  $d_i$  is the same but internal to the surface, shown in Figure 4-6.

For the 1:1 structure, the large peak on the lower part of the fingerprint plot is the result of the prominent O-H $\cdots$ N hydrogen bond. There is also a weaker interaction between C-H groups of the ring and an oxygen atom of formic acid which creates the smaller peak on the left of the fingerprint plot. This interaction accounts for 14% of the generated surface, and includes contributions from more than one C-H $\cdots$ O contact. The bulk of the points in the plot are from H $\cdots$ H interactions.

The H $\cdots$ O plots in Figure 4-6 shows clearly how different the interactions are in the 1:2 structure compared to the 1:1. The extended region on the left of the fingerprint plot represents all H $\cdots$ O interactions, accounting for 37% of the total surface interaction. This includes both the charge assisted hydrogen bond and all C-H $\cdots$ O contacts, which cannot be separated in this type of analysis.

For the 1:4 HP structure, the main peak in the fingerprint plot arises from O $\cdots$ H interactions. However, compared to the 1:2 fingerprint plot, this peak occurs at greater  $d_e$ , showing that the nearest contacts to the pyridinium proton are further away than for the 1:2 structure. This type of interaction accounts for 44% of the pyridinium surface interactions; a higher contribution than for the other two structures but also at greater distance from the pyridinium ion.

The LT polymorph of the 1:4 mixture has a different bonding pattern to that of the HP polymorph. In the fingerprint plot, the main peak on the left represents the H $\cdots$ O contacts, accounting for 46% of the surface. The large diffuse region at  $d_e \sim 1.2$  is largely from H $\cdots$ H contacts. This region is compressed in the HP structure fingerprint plot, as the molecules are more closely packed and therefore have shorter atom to atom contacts.

#### 4.4 Conclusions

We have shown that similar systems, comprised of the same components can have very different responses to high pressure and low temperature crystallisation.

The 1:2 mixture of pyridine and formic acid gives a glass on flash freezing and temperature cycling in a capillary, while application of HP affords a previously unreported salt co-crystal containing a charge-assisted hydrogen bond.

The 1:4 mixture of the same components exhibits LT/HP polymorphism, and adopts distinctly different structures under the two sets of conditions. It is clear that one contribution to this difference is the less directional hydrogen bonding in the 1:4 mixture, which allows close packing of molecules to have a greater effect, and a new polymorph to form when the components are compressed to high pressure, resulting in shorter atom-to-atom contacts and higher crystal density. The presence of such an interaction in the 1:1 mixture contributes to the structure's stability with regards to extreme conditions, enabling this system to maintain the same phase across the explored conditions.



We have also shown that where cryo-crystallisation is ineffective, a crystal structure may still be obtained by application of high pressure, and that the fingerprint plots of Hirshfeld surface interactions can easily highlight the prominence of particular interactions across different phases. This is evidence that a polymorph of a compound may exist only at pressures beyond ambient conditions, which may be predicted by CSP methods where time-consuming practical methods are unsuitable, such as screening for polymorphs of an active pharmaceutical ingredient. Additionally, where CSP results identify a possible a low energy polymorph that cannot be isolated by traditional crystallisation methods, HP crystallisation may represent an alternative route to isolation of novel solid forms.<sup>21</sup>

#### 4.5 References

1. D. Wiechert and D. Mootz, *Angew. Chem. Int. Ed.*, 1999, **38**, 1974-1976.
2. N. V. Drichko, G. Y. Kerenskaia and V. M. Schreiber, *J. Mol. Struct.*, 1999, **477**, 127-141.
3. M. R. Probert, C. M. Robertson, J. A. Coome, J. A. K. Howard, B. C. Michell and A. E. Goeta, *J. Appl. Crystallogr.*, 2010, **43**, 1415-1418.
4. M. R. Probert, J. A. Coome, A. E. Goeta and J. A. K. Howard, *Acta Crystallographica Section A*, 2011, **67**, C528.
5. T. Schulz, K. Meindl, D. Leusser, D. Stern, J. Graf, C. Michaelsen, M. Ruf, G. M. Sheldrick and D. Stalke, *J. Appl. Crystallogr.*, 2009, **42**, 885-891.
6. G. J. Piermarini, S. Block, J. D. Barnett and R. A. Forman, *J. Appl. Phys.*, 1975, **46**, 2774-2780.
7. *APEX2*, 1.08; Bruker AXS Inc.: Madison, WI, 2004.
8. *SAINT*, Bruker AXS Inc.: Madison, WI, 2007.
9. *SADABS*, Bruker AXS Inc.: Madison, WI, 2001.
10. S. Parsons *ECLIPSE* Edinburgh, UK, 2010.
11. O. V. Dolomanov, L. J. Bourhis, R. J. Gildea, J. A. K. Howard and H. Puschmann, *J. Appl. Crystallogr.*, 2009, **42**, 339-341.
12. G. M. Sheldrick, *Acta Crystallogr., Sect. A: Found. Crystallogr.*, 2008.
13. G. R. Newkome, K. J. Theriot and F. R. Fronczek, *Acta Crystallographica Section C*, 1986, **42**, 1539-1541.
14. J. W. Steed and J. L. Atwood, *Supramolecular Chemistry*, John Wiley & Sons, Chichester, 2nd edn., 2009.
15. G. A. Jeffrey, *An Introduction to Hydrogen Bonding*, Oxford University Press, 1997.
16. V. Balevicius, R. Bariseviciute, K. Aidas, I. Svoboda, H. Ehrenberg and H. Fuess, *PCCP*, 2007, **9**, 3181-3189.

17. S. N. Smirnov, N. S. Golubev, G. S. Denisov, H. Benedict, P. Schah-Mohammedi and H.-H. Limbach, *J. Am. Chem. Soc.*, 1996, **118**, 4094-4101.
18. M. A. Spackman and D. Jayatilaka, *CrystEngComm*, 2009, **11**, 19-32.
19. M. A. Spackman and J. J. McKinnon, *CrystEngComm*, 2002, **4**, 378-392.
20. P. A. Wood, J. J. McKinnon, S. Parsons, E. Pidcock and M. A. Spackman, *CrystEngComm*, 2008, **10**, 368-376.
21. M. A. Neumann, J. van de Streek, F. P. A. Fabbiani, P. Hidber and O. Grassmann, *Nat Commun*, 2015, **6**, 7793.

# Chapter 5 High Pressure/ Low Temperature Polymorphism in 2,6-Dimethylpyridine Formic Acid Co-crystals.

---

## 5.1 Introduction

The previous chapter discussed new polymorphs of pyridine-FA co-crystals obtained and studied by high pressure crystallisation techniques.<sup>1</sup> Datta and coworkers have explored how this system does not obey the  $\Delta pK_a$  [ $pK_a$  (base) –  $pK_a$ (acid)] principle used by the pharmaceutical industry to determine if an acid/base combination will produce a salt or a co-crystal on crystallisation.<sup>2</sup> Generally if the  $\Delta pK_a \geq 2-3$ , a salt will be formed. It was found by the Nangia group that for mixtures of pyridines and carboxylic acids this is not an accurate predictor for salt vs. co-crystal formation.<sup>3</sup> Instead a negative  $\Delta pK_a$  will result in a molecular co-crystal, while above 3.75 a salt will be formed. This leaves an intermediate region  $0 < \Delta pK_a < 3.75$  in which either crystal type, or a disordered solid form will be obtained, the prediction of which is made difficult by the nature of the partially polarized O-H...N hydrogen interaction between the pyridine derivative and carboxylic acid. DFT calculations were used by Datta to emphasize how the cooperative enhancement of formic acid acidity plays a large role in determining the nature of the crystallisation product, although the results of these calculations suggested that pyridine/formic acid crystals in acid: base ratios lower than 4:1 should be unstable with respect to proton transfer and

salt formation. It was concluded from this that at higher stoichiometry,  $\Delta pK_a$  is not a reliable indicator for proton transfer or potential salt or co-crystal formation.

Here we present the investigation into the highly sterically hindered pyridine analogue 2,6-lutidine (2,6-dimethylpyridine, DMP). DMP is a simple substituted pyridine derivative commonly used as a mild base, as well as a food additive.<sup>4</sup> While DMP is a slightly stronger Brønsted base than pyridine its steric bulk makes it a weaker hydrogen bond base and hence DMP complexes are expected to give interesting insight into the effect of basicity on HP/LT polymorphism of weak acid-base co-crystals and their propensity to undergo proton transfer.<sup>5,6</sup> The  $\Delta pK_a$  of a DMP and formic acid mixtures is 2.95.

## 5.2 Experimental

All mixtures of DMP and FA are liquid at room temperature. All low temperature structures were obtained by *in situ* cryo-crystallisation using a 0.3 mm borosilicate glass capillary, loaded with the appropriate mixture, sealed at both ends and affixed to a pin mounted to a goniometer head. Crystals were obtained by a combination of cooling using the cryostream and flash freezing with liquid nitrogen. Once crystals were obtained, the temperature was cycled to obtain a suitable single crystal. An Agilent Xcalibur Gemini diffractometer equipped with Oxford Cryosystems open flow nitrogen cryostat was used for diffraction. CrysAlis PRO<sup>7</sup> was used for data handling of the LT structures.

Crystals grown at high pressure were obtained by loading the liquid mixtures into a diamond anvil cell with diamond culets of 0.8 mm. Samples occupy a sample chamber created by a steel gasket of 0.25 mm thickness, pre-indented to 0.15 mm

with a precision drilled hole of 300  $\mu\text{m}$ . A ruby was included in the sample chamber for pressure determination.<sup>8</sup> The pressure was increased until a polycrystalline phase was obtained, then the pressure was cycled around the melting transition point until a single crystal was obtained of suitable quality and size for diffraction. The sample was pressurized beyond the crystal growth pressure region in order to minimize melting during data collection. The DAC was mounted directly onto the goniometer of XIPHOS II,<sup>9, 10</sup> a four circle Huber diffractometer with Ag-K $\alpha$   $I\mu S$ <sup>11</sup> generator located at Newcastle University. High pressure data were handled using the Bruker APEX2<sup>12</sup> software suite which incorporates SAINT<sup>13</sup> and SADABS<sup>14</sup> for integration, cell refinement and scaling. The program ECLIPSE<sup>15</sup> was used to generate dynamic masks to compensate for shading from the body of the DAC. The SHELX<sup>16</sup> program suite was used for structure solution and refinement within the OLEX2 interface.<sup>17</sup>

## 5.3 Results

Table 5-1. Summary of crystallographic data.

	HP			LT		
Base: Acid	1:1	1:2	1:3	1:1	1:2	1:3
empirical formula	C <sub>8</sub> H <sub>11</sub> NO <sub>2</sub>	C <sub>9</sub> H <sub>13</sub> NO <sub>4</sub>	C <sub>10</sub> H <sub>15</sub> NO <sub>6</sub>	C <sub>8</sub> H <sub>11</sub> NO <sub>2</sub>	C <sub>9</sub> H <sub>13</sub> NO <sub>4</sub>	C <sub>10</sub> H <sub>15</sub> NO <sub>6</sub>
T/K	296			230	200	230
P/kbar	0.28	1.53	3.71	ambient		
Crystal system	Orthorhombic		Monoclinic	Orthorhombic	Triclinic	Monoclinic
space group	<i>Pca</i> 2 <sub>1</sub>	<i>P</i> 2 <sub>1</sub> 2 <sub>1</sub> 2 <sub>1</sub>	<i>Pn</i>	<i>Pca</i> 2 <sub>1</sub>	<i>P</i> $\bar{1}$	<i>P</i> 2 <sub>1</sub> / <i>c</i>
<i>a</i> /Å	15.554(2)	3.969(2)	4.0173(7)	15.723(4)	7.914(2)	3.974(1)
<i>b</i> /Å	7.030(1)	24.22(2)	10.155(2)	7.137(1)	7.975(2)	14.993(5)
<i>c</i> /Å	7.3617(6)	10.116(9)	14.764(5)	7.497(1)	9.861(2)	20.717(7)
$\alpha$	90	90	90	90	69.68(2)	90
$\beta$	90	90	92.64(2)	90	81.57(2)	92.19(2)
$\gamma$	90	90	90	90	64.75(2)	90
Z	4	4	2	4	2	4
Z'	1	1	1	1	1	1
V/Å <sup>3</sup>	805.0(1)	972(1)	601.7(3)	841.3(3)	527.8(2)	1233.4(7)
<i>D</i> <sub>c</sub> /g cm <sup>-3</sup>	1.264	1.368	1.354	1.209	1.253	1.321
Unique reflns.	2965	2223	1747	2965	4346	11137
completeness/%	83	62	52	83	100	78
<i>R</i> <sub>1</sub>	0.0497	0.0815	0.0596	0.0497	0.0691	0.0784
<i>wR</i> <sub>2</sub>	0.12676	0.2913	0.1694	0.1267	0.1703	0.2646
GOF	1.035	1.113	1.076	1.035	1.0140	0.996

Table 5-2. N-H...O bond distances and angles for all structures from X-ray diffraction data.

	Donor	Hydrogen	Acceptor	DH/Å	HA/Å	DA/Å	DHA/°
1:1 HP	O9	H9	N1	1.02(10)	1.6(1)	2.589(8)	170(9)
1:1 LT	O9	H9	N1	0.83(2)	1.8(1)	2.616(3)	155(3)
1:2 HP	N1	H1	O9	1.0(2)	1.80(2)	2.64(3)	165(1)
1:2 LT	N1	H1	O9	1.06(4)	1.62(4)	2.673(3)	176(4)
1:3 HP	N1	H1	O9	0.86(1)	1.96(1)	2.80(2)	163(2)
1:3 LT	N1	H1	O9	0.99(3)	1.80(3)	2.771(3)	165(3)

### 5.3.1 1:1 DMP-FA

Both slow cooling and pressurizing DMP and FA in a 1:1 ratio affords a stoichiometric molecular co-crystal. The same polymorph is obtained from both the HP and LT crystallisation methods, with one molecule of each compound in the asymmetric unit. The dominant interaction is a hydrogen bond between the O-H group of FA and the nitrogen atom of the pyridyl ring of DMP, at a DA distance of 2.589(8) Å and 2.616(3) in the HP and LT crystals, respectively (Table 5-2). The DMP pyridyl rings interact via  $\pi$ - $\pi$  stacking at a plane-centroid distance of 3.6830(3) Å and offset shift of 1.385(9) Å measured from the LT dataset, shown in Figure 5-1 where the distance  $d_1$  is the place-centroid distance,  $d_2$  is the centroid-centroid distance and  $s$  is the shift.

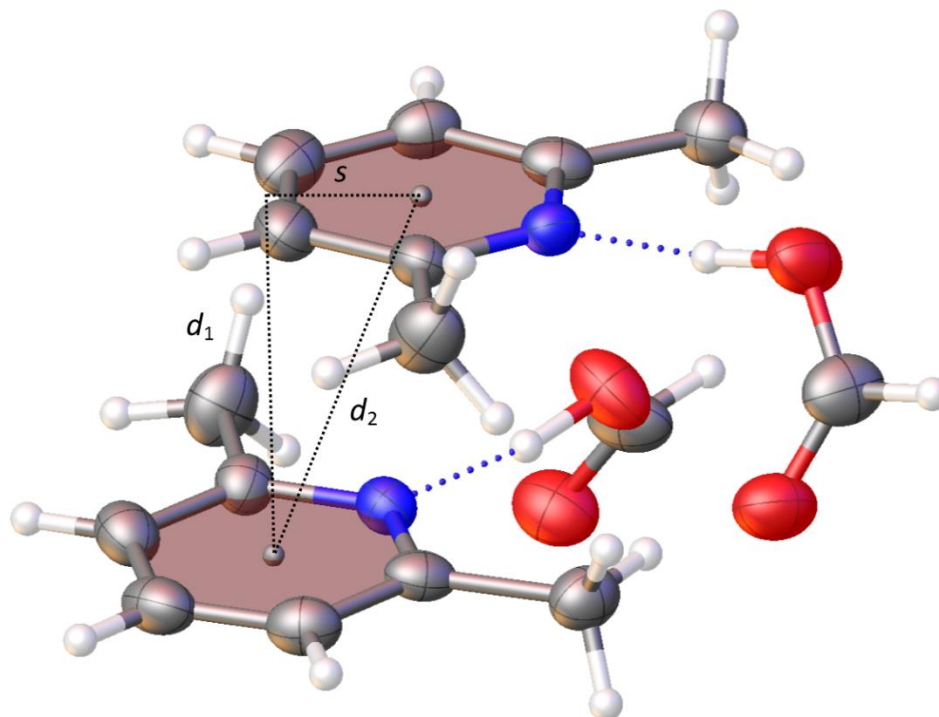


Figure 5-1.  $\pi$ - $\pi$  stacking interactions of DMP- FA crystallised by high pressure.

A comparison of the unit cell volume shows a compression of 4.3% in the HP structure relative to the LT form. The temperature difference of 66 K is a contributor to the change in cell volume, so difference does not accurately represent the extent of the compressibility of the structure. Data for the HP crystal were collected at 0.28 kbar (Table 5-1).

### 5.3.2 1:2 DMP-FA

A 1:2 mixture of DMP and FA crystallises *via* both HP and LT crystallisation methods. At this higher concentration of acid/base, HP/LT polymorphism is seen. While the HP structure crystallises in orthorhombic space group  $P2_12_12_1$ , the symmetry is lower in the LT form which is triclinic space group  $P\bar{1}$ . In the HP structure, the molecules are more closely packed, with a unit cell packing efficiency of 66% compared with 63% for the LT form.



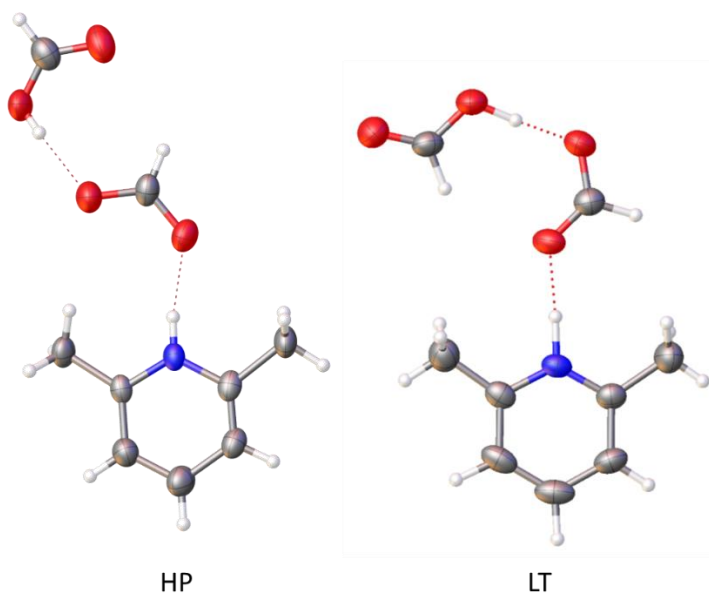


Figure 5-2. 2,6-dimethylpyridinium formate formic acid co-crystal asymmetric units from HP and LT crystallisation.

As with the pyridine analogue, an increased acid/base ratio strengthens the AH...B hydrogen bond interaction resulting in proton transfer between the pyridyl ring and FA, giving rise to a 2,6-dimethylpyridinium formate formic acid salt co-crystal from both crystallisation routes (Figure 5-2).<sup>1, 2, 18</sup> With a  $\Delta pK_a$  of 2.95, the DMP-FA mixtures fall in the intermediate  $\Delta pK_a$  region of salt/co-crystal formation for pyridines and carboxylic acids. This 1:2 salt formation is influenced by the cooperative nature of the FA molecules enhancing acidity and therefore proton transfer at stoichiometries higher than 1:1, the same effect which is seen in the pyridine-FA mixtures.

Each polymorph of 1:2 DMP-FA contains one DMP-H<sup>+</sup> ion, a formate ion and a molecule of formic acid in a planar arrangement, with a charge assisted hydrogen bond between the 2,6-dimethylpyridinium and formate ions. The relative

orientations of the formate and formic acid groups to DMP-H<sup>+</sup> differ between the HP and LT forms (Figure 5-2) resulting in a considerable change in symmetry and unit cell parameters (Table 5-1).

The hydrogen bond distances of the NH...O hydrogen interaction between DMP-H<sup>+</sup> and formate are 2.64(3) and 2.673(3) Å for HP and LT, respectively (Table 5-3). The charge assisted hydrogen bond in the higher ratio co-crystal is a critical factor in determining crystal structure but the ion-ion interaction between DMP-H<sup>+</sup> and formate is also a consideration. The OH...O bond distance in the 1:2 polymorphs is 2.516(4) for the LT form and 2.48(3) for HP.

**Table 5-3. Hydrogen bonding parameters of 1:2 DMP-FA HP**

	D	H	A	DH/ Å	HA/ Å	DA/ Å	DHA/ °
HP	N1	H1	O9	1.0(2)	1.80(2)	2.64(3)	165(1)
	O12	H12	O11	0.82(2)	1.78(2)	2.48(3)	142(1)
LT	N1	H1	O9	1.06(4)	1.62(4)	2.673(3)	176(4)
	O12	H12	O11	1.03(5)	1.49(5)	2.516(4)	177(4)

If we consider the DMP-formate-formic acid arrangement in each structure to be the 'synthon' for that form, the synthons have significantly different packing arrangements in each crystal structure. In the LT polymorph, the synthons pack *via* weak CHO interactions and off-set  $\pi$ - $\pi$  stacking between pyridyl rings into discrete layers in the (440) plane. The HP polymorph has a more complex packing arrangement, as shown in Figure 5-3.

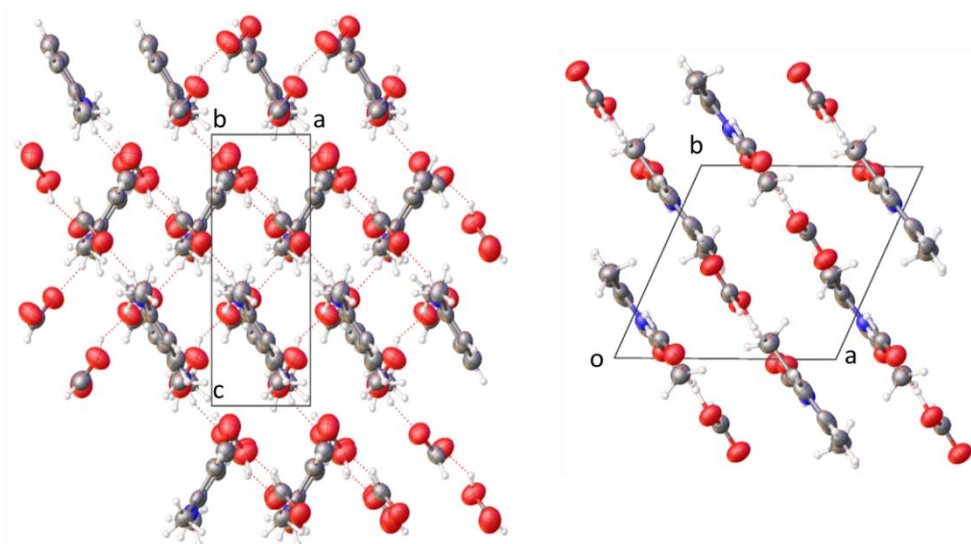


Figure 5-3. Packing arrangements of 1:2 DMP-FA from HP and LT.

Offset  $\pi$ - $\pi$  stacking is present in both HP and LT forms, although the interaction is closer in the LT form with a shift of 1.829(7) Å and distance 3.869(3) Å compared with shift of 2.13(4) Å and distance 3.969(2) Å in the HP polymorph, suggesting it is a more dominant interaction in this configuration.

### 5.3.3 1:3 DMP-FA

Mixtures of DMP and FA in ratios 1:3 and higher, crystallise in a 1:3 structure. This concentration also exhibits HP/LT polymorphism, although it is more subtle than that seen for the 1:2 co-crystal. Figure 5-4 shows the asymmetric units of the 1:3 co-crystals from DAC crystallisation and capillary crystallisation. Both have undergone proton transfer during crystallisation and contain one 2,6-dimethylpyridinium ion, a formate ion and two molecules of formic acid, in a hydrogen bonded synthon. While the unit cell parameters for the two forms are very similar to one another (Table 5-1) the details of the packing arrangement reveals that the crystals are two distinct polymorphs. The primary difference

between the asymmetric units is the orientation of the FA groups relative to the primary DMP-H<sup>+</sup>-formate hydrogen bond interaction.

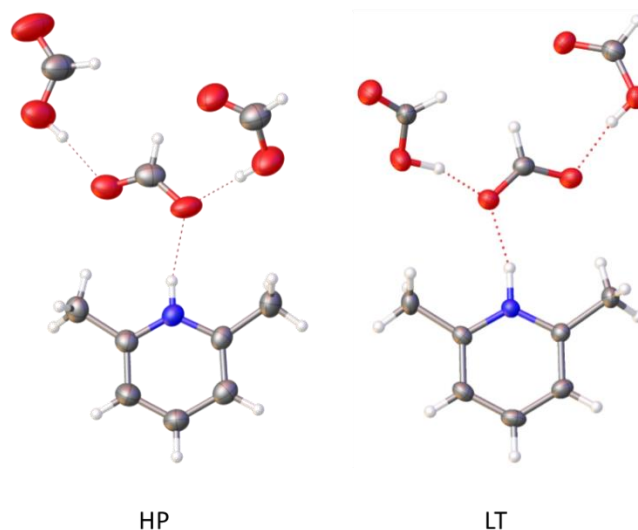


Figure 5-4. Asymmetric unit of 1:3 DMP-FA co-crystals.

An overlay of the two structures (Figure 5-5) shows that while the DMP-H<sup>+</sup> – formate interaction is largely the same, the two FA molecules are ‘flipped’ relative to each other, as if rotated around the C-O bonds O12-C13 and O15-C16.

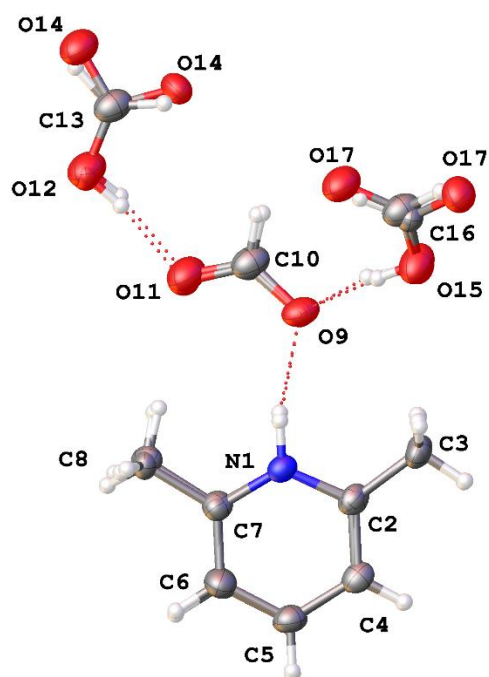


Figure 5-5. Overlay of HP and LT structures of 1:3 2,6-dimethylpyridinium formate bis(formic acid).

While DMP has a 1:3 ratio with formic acid at higher pressures, pyridine forms a 1:4 structure and no evidence of a 1:3 form has been observed.<sup>1</sup> This is likely due to the steric hindrance of the methyl groups preventing FA from packing as closely around the pyridyl ring (Figure 5-6). A 1:4 mixture of DMP and FA acid was found to crystallise in the 1:3 form. The steric hindrance also causes the nature of the charge assisted hydrogen bond to differ between the co-crystal analogues; the pyridinium ion in 1:4 pyridine-FA displays a bifurcated hydrogen bonding pattern to two FA molecules, whereas all of the DMP co-crystals with FA retain the highly directional NHO bond regardless of proton transfer or lack thereof.

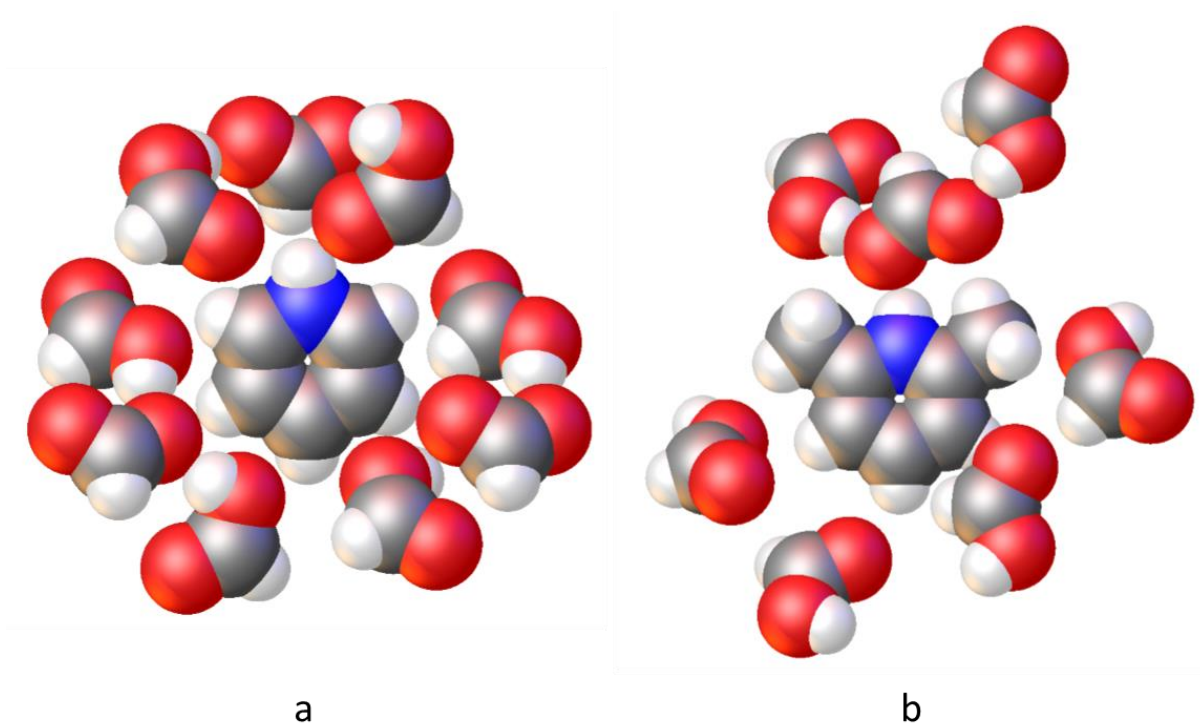


Figure 5-6. Space-filling packing diagrams showing the environment of the pyridyl ring in a) HP 1:4 pyridine-FA and b) HP 1:3 DMP-FA.

Table 5-4. Hydrogen bond parameters of HP and LT polymorphs of 1:3 DMP-FA

	D	H	A	DH	HA	DA	DHA
HP	N1	H1	O9	0.86(1)	1.96(1)	2.80(2)	163(2)
	O15	H15	O9	0.82(2)	1.79(1)	2.60(2)	172(1)
	O12	H12	O11	0.82(2)	1.84(1)	2.56(2)	150(1)
LT	N1	H1	O9	0.99(3)	1.80(3)	2.771(3)	165(3)
	O15	H15	O9	1.02(6)	1.58(6)	2.566(4)	162(5)
	O12	H12	O11	0.83(3)	1.75(6)	2.562(3)	167(1)

The donor...acceptor distances are remarkably similar between the two structures, emphasizing the subtlety of the polymorphism in this system, although the bonds are slightly shorter in the LT polymorph (Table 5-4). The largest difference is seen in the DHA bonding angles, particularly between the formate ion and one FA molecule; the bond O12-H12-O11 has a difference of 17° between polymorphs.

## 5.4 Discussion

All of the DMP-FA co-crystals display relatively strong, directional hydrogen bonds between the DMP and FA components (Table 5-2), including the higher ratio structures. The hydrogen bond type is evident in the DA bond distances; shortest for HP 1:1 DMP-FA at 2.589(8) Å a neutral interaction, but longer distances of 2.64(3) Å and 2.798(17) Å for the HP 1:2 and 1:3 co-crystals, respectively.

In the 1:4 pyridine-FA co-crystal<sup>1</sup> the ion-ion interaction of pyridinium and formate ions takes precedence over strong directional hydrogen bonding in the crystal packing and there are two weaker hydrogen bonding interactions between the pyridyl nitrogen and formic acid molecules as opposed to a single, more directional bond, which is present in all DMP-FA co-crystals reported here. The methyl groups of DMP have the combined effect of sterically hindering the pyridyl nitrogen atom and increasing its Brønsted basicity relative to pyridine.<sup>5</sup> The methyl substitution does not appear to have an effect on proton transfer despite DMP being a slightly stronger base than pyridine, with a  $pK_{aH}$  of 6.8 compared with 5.2, where  $pK_{aH}$  is the  $pK_a$  of the conjugate acid. In both instances, proton transfer occurs for an acid/base ratio of 2 or higher. The difference in the Brønsted basicity between the two heteroaromatic rings is reflected in the hydrogen bond lengths in the higher ratio crystal structures, for both HP and LT forms of DMP-FA and pyridine-FA co-crystals. The HA and DA hydrogen bonding distances are consistently shorter for the DMP co-crystals, due the higher basicity of 2,6-dimethylpyridine. In the HP form of 1:3 DMP-FA the N-H $\cdots$ O charge assisted hydrogen bond has a DA distance of 2.80(2) Å, while the equivalent bond in 1:4 pyridine-FA has a distance of 2.853(10) Å. There

is a larger difference for the equivalent LT forms with 1:3 DMP-FA having an N-H...O distance of 2.771(3) Å compared with 2.870(3) Å for the pyridine analogue. The bifurcated nature of the hydrogen bonding in the pyridine-FA co-crystal contributes to the longer bonding lengths, which are not possible with DMP due to the steric hindrance of the methyl groups adjacent to the pyridyl nitrogen. The relative basicity has a significant effect on the bonding distances and this is seen also for the 1:1 co-crystals of both heteroaromatic rings, where in each case there is a strong, directional hydrogen bond between neutral molecules. The D-A distance for this bond in the 1:1 DMP-FA structure is 2.589(8) Å and 2.634(12) Å for the pyridine-FA.

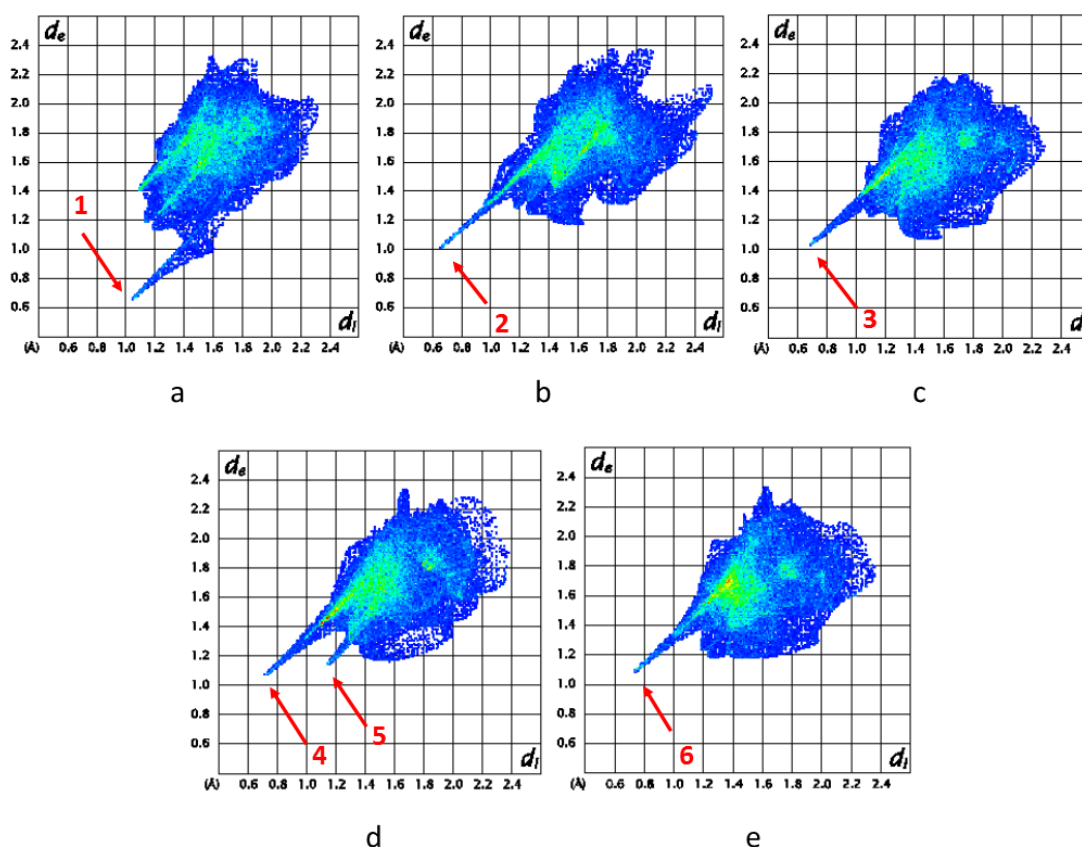


Figure 5-7. Hirshfeld surface fingerprint plots of DMP-FA; a) 1:1 LT, b) 1:2 LT, c) 1:2 HP, d) 1:3 LT and e) 1:3 HP, showing features from N-H interactions (1) O-H interactions (2-4, 6) and H-H interactions (5).



Fingerprint plots generated from Hirshfeld surfaces using the visualization tool Crystal Explorer offer a useful way of representing the intermolecular interactions within a crystal and differences in bonding between polymorphs and comparable co-crystals.<sup>19-21</sup> The program generates a Hirshfeld surface around a selected atom or group and plots the proximity of other atoms or groups to this surface using values  $d_e$ , the distance between the Hirshfeld surface and the nearest external contact and  $d_i$ , the distance between the surface and the nearest internal contact. This plot is known as a fingerprint plot.

Figure 5-7 shows the fingerprint plots for the Hirshfeld surface of DMP/ DMP-H<sup>+</sup> for each polymorph of DMP-FA. The plots show the following differences in the nature of intermolecular contacts within the structure. In Figure 5-7a, the feature labelled 1 is due to the N $\cdots$ H interaction between the nitrogen of DMP and the acidic proton of FA, a neutral hydrogen bonding interaction. As proton transfer has occurred in the other four structures this peak is no longer seen, but a new feature at higher  $d_e$  appears labelled 2,3,4 and 6, as a result of the H $\cdots$ O charge assisted hydrogen bond interaction. When analyzed by individual atom types, the contribution of N $\cdots$ H interactions in plots *b-e* is less than 1%, while for *a*, it is 6.6%.

For all of the structures, the majority of the surface interaction is due to H $\cdots$ H interactions, which make up the bulk of the blue area and the features in the top right of each plot. However in plot Figure 5-7d (1:3 LT) the peak labelled 5 is also due to H $\cdots$ H interactions, within close contact to each other than is seen in any other DMP-FA structure including the HP 1:3 polymorph. This is due to the atom H8C on one of the methyl groups of DMP; crystal packing brings this hydrogen atom

into close contact with equivalent H8C atoms on neighbouring DMP-H<sup>+</sup> in adjacent layers. This is an unusual feature not seen for the other high pressure co-crystals of DMP and pyridine, which instead show changes to the more diffuse region of the fingerprint plot which represents the bulk of H...H contacts, rather than an enforced short contact. In the HP plots, this diffuse H...H region is more compact than in the LT versions as molecules are encouraged into closer contact by the application of pressure.

## 5.5 Conclusions

Mixtures of 2,6-dimethylpyridine and formic acid offer a good example of high pressure/ low temperature polymorphism analogous to that seen for the similar pyridine formic acid systems.

A 1:1 mixture of DMP and FA affords a neutral co-crystal with the same polymorph obtained from both HP and LT crystallisation methods. Higher concentration forms 1:2 and 1:3 afford salt co-crystals with components in the expected acid/base ratio although proton transfer between the acid and base has occurred resulting in charge-assisted hydrogen bonding interactions. This is potentially a contributing factor in the HP/LT polymorphism of the system, given the lack of polymorphism in the neutral molecular co-crystal of 1:1 DMP-FA.

The use of Hirshfeld surface fingerprint plots has clearly indicated structural differences between polymorphs that are otherwise not obvious from inspection of the unit cell and packing of a structure as is the case for the 1:3 polymorphs of DMP-FA, which exhibit subtle differences between polymorphs.

## 5.6 References

1. R. Lee, A. J. Firbank, M. R. Probert and J. W. Steed, *Cryst. Growth Des.*, 2016, **16**, 4005-4011.
2. S. M. Pratik and A. Datta, *The Journal of Physical Chemistry B*, 2016, **120**, 7606-7613.
3. B. R. Bhogala, S. Basavoju and A. Nangia, *CrystEngComm*, 2005, **7**, 551-562.
4. PubChem Compound Database, <https://pubchem.ncbi.nlm.nih.gov/compound/7937>, (accessed Oct 20, 2016).
5. I. I. Grandberg, G. K. Faizova and A. N. Kost, *Chem. Heterocycl. Compd. (N. Y., NY, U. S.)*, 1967, **2**, 421-425.
6. C. Laurence and M. Berthelot, *Perspect. Drug Discovery Des.*, 2000, **18**, 39-60.
7. Agilent *CrysAlis PRO*, Agilent Technologies Ltd: Yarnton, Oxfordshire, UK, 2014.
8. R. A. Forman, G. J. Piermarini, J. D. Barnett and S. Block, *Science*, 1972, **176**, 2.
9. M. R. Probert, C. M. Robertson, J. A. Coome, J. A. K. Howard, B. C. Michell and A. E. Goeta, *J. Appl. Crystallogr.*, 2010, **43**, 1415-1418.
10. M. R. Probert, J. A. Coome, A. E. Goeta and J. A. K. Howard, *Acta Crystallographica Section A*, 2011, **67**, C528.
11. T. Schulz, K. Meindl, D. Leusser, D. Stern, J. Graf, C. Michaelsen, M. Ruf, G. M. Sheldrick and D. Stalke, *J. Appl. Crystallogr.*, 2009, **42**, 885-891.
12. *APEX2*, 1.08; Bruker AXS Inc.: Madison, WI, 2004.
13. *SAINT*, Bruker AXS Inc.: Madison, WI, 2007.
14. *SADABS*, Bruker AXS Inc.: Madison, WI, 2001.
15. S. Parsons *ECLIPSE* Edinburgh, UK, 2010.
16. G. Sheldrick, *Acta Crystallographica Section C*, 2015, **71**, 3-8.
17. O. V. Dolomanov, L. J. Bourhis, R. J. Gildea, J. A. K. Howard and H. Puschmann, *J. Appl. Crystallogr.*, 2009, **42**, 339-341.
18. V. Balevicius, R. Bariseviciute, K. Aidas, I. Svoboda, H. Ehrenberg and H. Fuess, *PCCP*, 2007, **9**, 3181-3189.
19. M. A. Spackman and D. Jayatilaka, *CrystEngComm*, 2009, **11**, 19-32.
20. M. A. Spackman and J. J. McKinnon, *CrystEngComm*, 2002, **4**, 378-392.
21. S. K. Wolff, D. J. Grimwood, J. J. McKinnon, M. J. Turner, D. Jayatilaka and M. A. Spackman *CrystalExplorer*, University of Western Australia, 2012.

# Chapter 6 Polymorphism of ROY at high pressure

---

## 6.1 Introduction

5-methyl-2-[(2-nitrophenyl)amino]-3-thiophenecarbonitrile (Figure 6-1), nicknamed ROY for its bright red, orange and yellow crystals, has seven known polymorphs and evidence of another three for which the structures have not yet been determined.<sup>1</sup>

The compound is a precursor to the anti-psychotic drug olanzapine, patented by Lilly Industries Ltd. in 1991.<sup>2</sup> In more recent years however, it has been of great interest to crystallographers because of its extensive polymorphism.

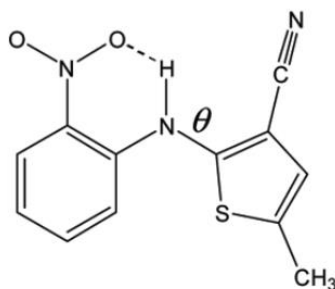


Figure 6-1. Molecular structure of ROY, with torsional angle  $\theta$ .

The first crystal structures of ROY in the Cambridge Structural Database (CSD) were elucidated by Yu *et al.*, who simultaneously reported six solvent free polymorphs in 2000; orange needles (ON), yellow prisms (Y), red prisms (R), orange prisms (OP), yellow needles (YN) and orange-red plates (ORP) (Figure 6-2).<sup>1, 3</sup>

The seventh polymorph of ROY was obtained in 2001 by the Ward group, by sublimation of ROY onto the (010) surface of a succinic acid crystal.<sup>4</sup> It was labelled RPL due to its red plate appearance (Figure 6-2). RPL was confirmed as a new polymorph by Raman spectroscopy, although no crystal structure was obtained as the crystallites are observed only when adhered to the succinic acid surface and are unstable with respect to the other polymorphs, with a tendency to convert to the YN form when heated. Additionally, the crystallites obtained were microscopic in scale, with dimensions on the order of 1-20  $\mu\text{m}$  (Figure 6-2).

In 2004, ROY became the most polymorphic compound on record at the time with the discovery of two new polymorphs Y04 and YT04 by the Yu group.<sup>5</sup> The crystal structure of YT04 was determined, but not Y04. Y04 was obtained by crystallisation from the melt and subsequently undergoes solid state transformation to YT04 over time, or to R when heated. As such, no melting point data is available and no Raman spectra of Y04 are reported. It is determined to be a new polymorph largely by a process of elimination based on transformation behaviour and crystal habit.

The same group reported the 10<sup>th</sup> polymorph of ROY in 2005, obtained by cross-nucleation between polymorphs.<sup>6</sup> Y04 crystallises spontaneously from the melt and subsequently seeds the nucleation of other polymorphs. The R and YN forms nucleate on the surface of Y04 and a novel form also crystallised – dubbed R05 for its red colour and year of discovery. Which cross-nucleation event is seen depends on the temperature and surface characteristics of the initial Y04 crystallite. The

structure of R05 has not been determined, so currently there are known crystal structures for only seven of the ten forms of ROY.

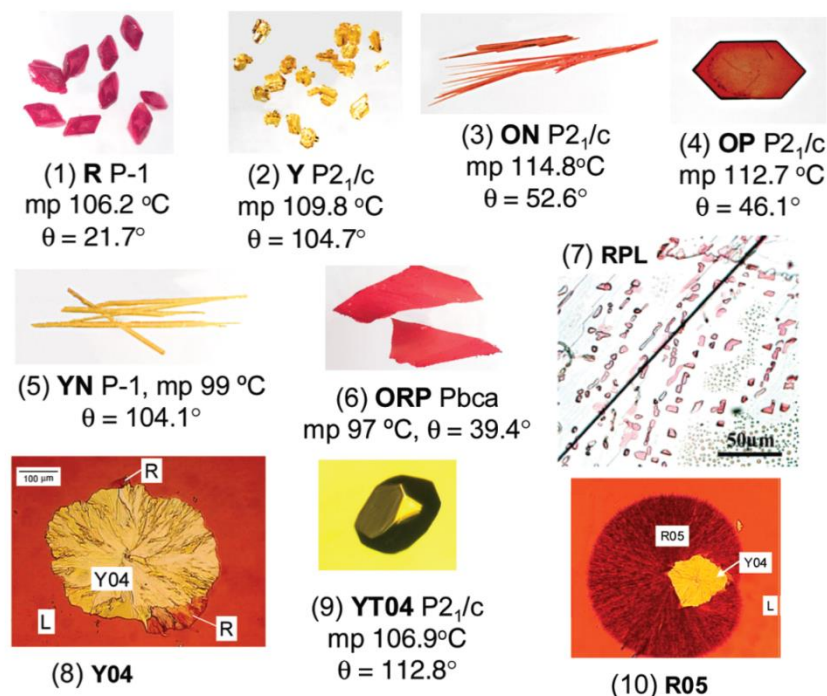


Figure 6-2. Polymorphs of ROY. Adapted with permission from L. Yu, *Acc. Chem. Res.*, 2010, 43, 1257-1266. Copyright 2010 American Chemical Society

ROY has previously held the record for most polymorphic compound in the Cambridge Structural Database when the seventh crystal structure YT04 was solved in 2004.<sup>5</sup> Since then, it has been surpassed by the drug compound aripiprazole, which currently has nine solved single crystal structures reported, and evidence of a further three.<sup>7</sup> The extensive polymorphism of ROY arises largely from conformational differences in the crystal structures, giving rise to the different coloured crystals, as well as significant differences in crystal habit. This conformational polymorphism is also evident in analogues of ROY.<sup>8,9</sup> The largest

contributing factor to ROY's extensive polymorphism is the torsional angle between the thiophene ring and amino group, labelled  $\theta$  in Figure 6-1. The various forms of ROY crystallise from a number of different solvents (Table 6-1), often concomitantly and frequently convert to one of the more stable forms. The yellow prism form (Y) is the thermodynamically most stable polymorph, followed by the orange needle form (ON), which will convert to Y above 70°C.<sup>10</sup>

Table 6-1. Crystallisation solvents of common polymorphs of ROY.<sup>10</sup>

Solvent	Polymorph
Acetone	YN, Y
Acetonitrile	Y
Dichloromethane	ON, Y
Ethyl Acetate	ON, Y, YN
Methanol	YN
1-Propanol	Y, ON

ROY is frequently the subject of investigations into the nature of polymorphism, nucleation and crystal growth.<sup>11, 12</sup> It is also used as test case for the development of crystal structure prediction (CSP) methodologies owing to its reasonably small size and array of well characterised forms. CSP has previously been used to successfully 'predict' the seven known crystal structures as lattice-energy minima and further offers possible structures for the three as-yet unsolved forms.<sup>13</sup> Other computational methods have also been applied to ROY in an effort to determine the nature of its conformational polymorphism and the relationship to the bright

colours of the crystals.<sup>14, 15</sup> Steed and co-workers recently reported a method for consistently obtaining the metastable red prism form of ROY without concomitant crystallisation.<sup>16</sup> A series of supramolecular bis(urea) gels were designed specifically to mimic the functionality of ROY using *o*-nitroaniline derived functional groups. The metastable polymorph was obtained from crystallisation within a toluene gel.

Here we report the use of high pressure crystallisation from solution using diamond anvil cell pressurisation to further explore the polymorphic landscape of ROY. CSP results of *ab initio* techniques applied to ROY suggest that there may be more polymorphs of the compound to be discovered.<sup>13</sup> Crystallographic and spectroscopic techniques have been utilised to characterise the obtained form, using crystallisation methods not previously reported in the investigation of ROY polymorphism.

## 6.2 Experimental

High-pressure structures were obtained by *in situ* compression in a diamond anvil cell. A 0.25 mm thickness steel gasket, pre-indented to 0.15 mm, with a precision drilled 300  $\mu\text{m}$  hole created the sample chamber between the two diamond anvils, of culet size 0.8 mm. A ruby chip was included in the sample chamber for pressure determination. Pressure was applied until the sample gave a polycrystalline material, at which point the pressure was cycled around the melting transition to reduce the number of crystals in the cell. The DAC was directly attached to a goniometer head and mounted on the diffractometer. Data were collected using the XIPHOS II<sup>17, 18</sup> diffractometer at Newcastle University, a four-circle Bruker



diffractometer with Ag-K $\alpha$   $I\mu S$  generator.<sup>19</sup> The pressure inside the cell was measured after equilibration by the R<sub>1</sub> ruby fluorescence method.<sup>20</sup>

X-ray data for ROY crystals were collected at 100 K on beamline I19 at Diamond Light Source using synchrotron radiation ( $\lambda = 0.68890 \text{ \AA}$ ) and processed using APEX2.<sup>21</sup>

Yellow prisms (Y) and orange needles (ON) of ROY were crystallised at ambient pressure and temperature by slow evaporation from concentrated solutions of acetone and ethyl acetate, respectively. A concentrated solution of ROY in acetone, obtained by adding acetone dropwise to approximately 50 mg of ROY until fully dissolved, was loaded into the DAC and pressure was increased until crystallisation occurred.

In order to determine which form of ROY was being obtained from the DAC, Raman spectra were obtained using a Horiba Jobin-Yvon LabRAM HR confocal Raman microscope equipped with an Nd:YAG (532 nm) and He-Ne (633 nm) laser. Spectral resolution is 3 cm<sup>-1</sup>. Spectra were collected on yellow prisms, orange needles and the needles present in the cell.

### 6.3 Results and Discussion

As seen in Table 6-1, a solution of ROY in acetone typically produces yellow crystals, either as yellow prisms or yellow needles. When a concentrated solution of ROY is loaded into the DAC, it can produce prisms or needles. If the Y form nucleates the solution is seeded with this form and the other polymorphs are never observed

concomitantly in the DAC. When the solution was too concentrated, or had time to evaporate before the cell was sealed, the Y form of ROY nucleated in the cell, grew with increased pressure but then did not dissolve entirely when the pressure was reduced (Figure 6-3A). If the pressure was reduced too far, the seal on the cell was lost and the solvent evaporated rapidly. Equally, if the cell was heated in order to dissolve the crystal without reducing the pressure, the seal on the cell was lost and the acetone evaporated. If the Y form crystallised in the cell it is an indicator that the initial ROY solution was too concentrated and needed to be diluted with a few additional drops of acetone. Additionally, cooling the various parts of the DAC and the gasket slowed down evaporation of the solution during sample loading, so the Y form did not have time to nucleate.

A trial and error process was used to obtain the correct concentration in the cell, beginning with a saturated solution at ambient temperature and reducing the concentration dropwise until loading the solution into the cell resulted in needles rather than prisms once pressure was applied. Once the correct concentration was obtained in the cell, crystals with a needle like habit nucleated and grew to fill the majority of the cell at a pressure of 8.8 kbar (Figure 6-3B and C), herein termed ONP (Orange Needles from Pressure). On pressure cycling, the needles proved to be very susceptible to changes in pressure. Even if a single needle, or small cluster could be isolated, the solution showed a preference for nucleating additional crystals over growing those already present in the sample chamber. As such, no single crystal of ONP could be obtained in order to carry out single crystal diffraction (Figure 6-3D).

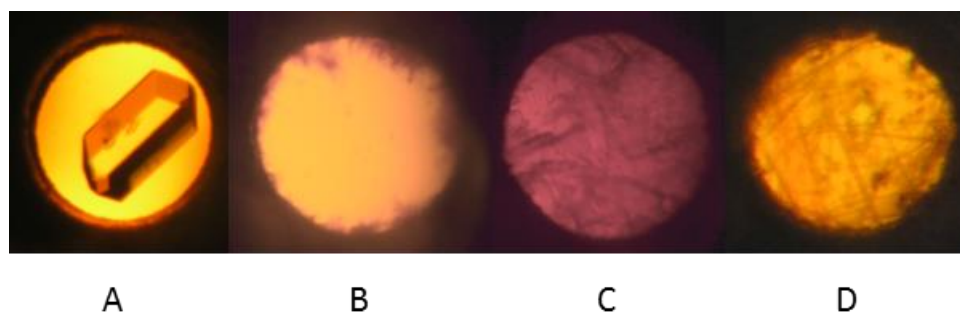


Figure 6-3. Crystals grown in DAC by application of pressure. A)  $\gamma$  crystals. B) ONP nucleating on gasket surface. C) ONP needles filling the cell. D) Larger ONP needles grown by pressure cycling.

Raman spectroscopy was used to differentiate between polymorphs from DAC crystallisation and those obtained using conventional solution methods. Raman spectra of pure ROY polymorphs already existing in the literature were used for comparison.<sup>10</sup>

The crystals of ONP were retrieved from the apparatus, using a method which has not previously been reported in the literature associated with high pressure crystallisation. Typically, crystals grown from solution or liquids in a DAC cannot be extracted in order to carry out conventional single crystal diffraction. This is primarily because the action required to open the cell is the same as to reduce the pressure and the crystals will dissolve if they are in solution, or melt if the sample is liquid at ambient pressure. The first example in the literature of a high pressure phase being successfully recovered from a pressure cell is the isolation of ikaite, a HP polymorph of calcium carbonate.<sup>22</sup> The crystal was obtained by cooling the pressure cell to 0°C before recovering the ikaite crystal. Crystals of  $\gamma$ -amino butyric acid monohydrate have previously been retrieved from a DAC by rapidly opening the cell and immersing the crystal in oil before significant dissolution could occur.<sup>23</sup>

Additionally, a polymorphic derivative of maleic hydrazine has previously been retrieved to ambient conditions, although the method used is not reported.<sup>24</sup>

Another example is the recovery of a crystal of a ciprofloxacin sodium salt from an aqueous solution in a DAC.<sup>25</sup> In this case, temperature cycling was used to grow the crystal and when held at 293 K, the pressure could be reduced slowly and only minimal dissolution of the crystal was observed. The ONP crystals presented a particular challenge owing to the high solubility of ROY in the solvent. Unlike  $\gamma$ -amino butyric acid and ciprofloxacin, opening the DAC containing ROY at ambient pressure resulted in rapid dissolution of the crystals on reduction of pressure, so additional measures were required to recover the crystals intact.

In order to circumvent the dissolution process, a DAC containing ONP from acetone was submerged in liquid nitrogen and allowed to cool, freezing the solvent. The pressure was reduced and the top half of the cell body and screws removed while the cell was still under nitrogen. The cell was removed from the nitrogen and the top diamond and backing disc were removed. Once the cell was open to the atmosphere, the acetone remaining in the cell evaporated rapidly on exposure to air, before the crystals were able to re-dissolve. The resulting ONP crystals deposited on the surface of the diamond (Figure 6-4). There were also some yellow crystals on the diamond surface, with a habit consistent with form Y, which were not present in the sample chamber prior to opening the cell. It is likely that these samples crystallised outside the sample chamber on the surface of the gasket and were deposited on the culet on evaporation of the acetone, as the evaporation

would have been too rapid for crystals of this size to grow as the cell was opened. Residue from the solution and some tiny crystallites can also be seen adhering to the diamond surface in Figure 6-4.

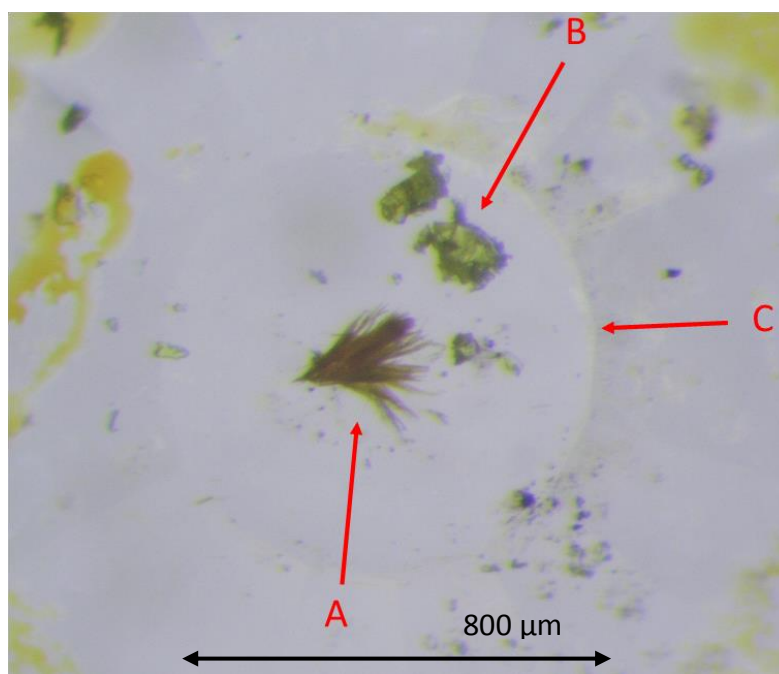


Figure 6-4. ROY crystals on diamond surface after opening of DAC. A) ONP form. B) Y form. C) Edge of diamond culet.

The ONP crystals were carefully extracted from the diamond surface and studied by Raman spectroscopy (Figure 6-5) and synchrotron X-ray diffraction at Diamond Light Source, instrument EH1, beamline I19. The crystals were prone to breaking and were grouped in very tight clusters which were difficult to separate without crystal disintegration.

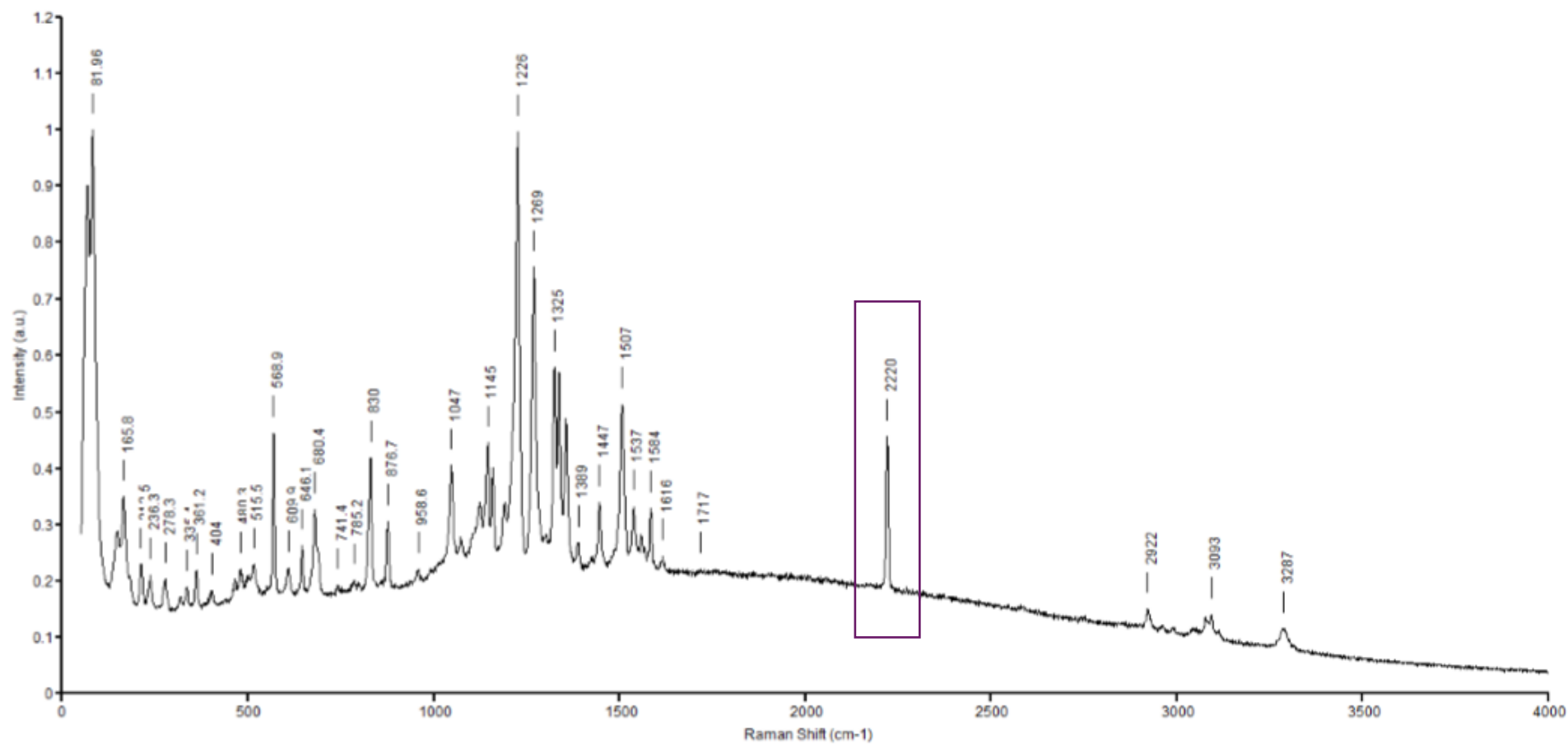


Figure 6-5. Raman spectrum of ROY needles grown in a DAC, once recovered from the cell.  $\nu_{CN}$  peak is highlighted.

Figure 6-5 shows the Raman spectrum of the crystals of ONP grown in a DAC and recovered to ambient conditions. The highlighted peak indicates the  $\nu_{\text{CN}}$  stretch which is commonly used to distinguish between ROY polymorphs. Table 6-2 details what values of this stretch for the polymorphs of ROY which have spectral data available in the literature.<sup>10, 26</sup>

**Table 6-2. Characteristic  $\nu_{\text{CN}}$  Raman stretches of ROY polymorphs.<sup>10, 26</sup>**

Polymorph	$\nu_{\text{CN}}$ stretch/ $\text{cm}^{-1}$
RPL	2210
R	2214
ORP	2219
ONP	2220
YN	2223
ON	2225
OP	2228
YN	2234
Amorphous	2234

The closest match with ONP is that of the ORP polymorph, although given the spectral resolution of  $3 \text{ cm}^{-1}$  polymorphs YN and ON are also close matches. The full Raman spectrum of ORP is not available in the literature.

### 6.3.1 Synchrotron diffraction data

A sample of the crystals retrieved from the DAC by the method described previously were taken to Diamond Light Source where synchrotron diffraction data were collected. The sample proved troublesome due to the size and fragility of the

crystals and no single crystal could be isolated for the diffraction experiment. A dataset of over 3000 reflections was collected from a cluster of crystals, which also contained residual ruby dust which adhered to the crystals on opening of the DAC. Isolating the reflections from individual crystals was challenging. After some effort, a unit cell was obtained from reflections attributed to ONP: monoclinic  $a = 4.00(4)$ ,  $b = 23.1(2)$ ,  $c = 12.87(12)$ ,  $\beta = 94.89(14)$ . This unit cell is crystallographically related to the ORP form of ROY (Table 6-3) with the relationship:  $a_{\text{ONP}} \approx \frac{1}{2}b_{\text{ORP}}$ ,  $b_{\text{ONP}} \approx c_{\text{ORP}}$ ,  $c_{\text{ONP}} \approx a_{\text{ORP}}$ . This suggests that the crystals grown *in situ* are a modified version of ORP. ORP has been obtained from methanol solution in concomitant crystallisation with other forms, but has not been reported as a crystallisation product from acetone solution. Primarily, yellow forms of the compound are obtained from ambient pressure acetone crystallisation.



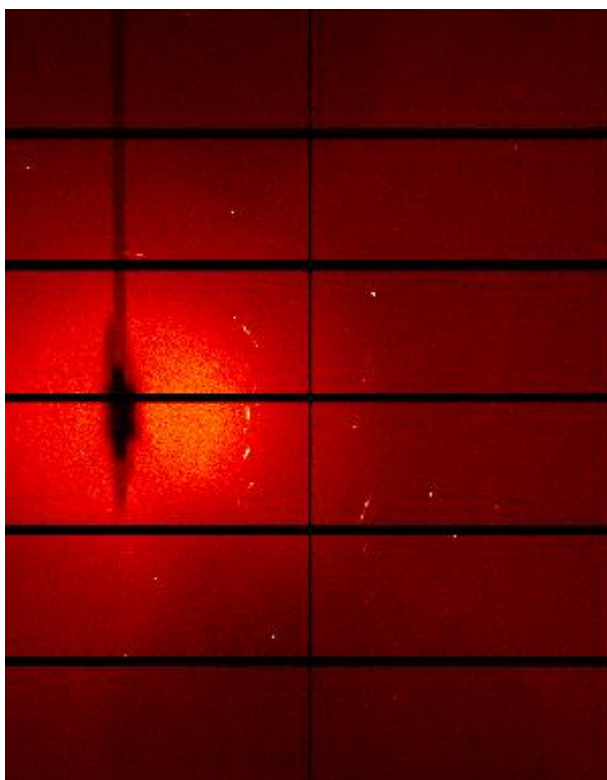


Figure 6-6. Single diffraction frame of ROY crystals collected on I19, DLS.

Figure 6-6 is a diffraction image of the ROY crystals obtained from DAC crystallisation, showing that while the sample diffracts, very few discrete diffraction spots are observed, due to the nature of the crystals. Figure 6-7 shows a representation of the diffraction pattern in reciprocal space, visualised using the reciprocal lattice viewer of APEX2.<sup>21</sup> The image on top displays the total reflections obtained from one data collection on the sample, while the image below shows the reflections belonging to one crystal only. This lattice was used to index the unit cell of ONP, but structure solution and refinement were unfeasible.

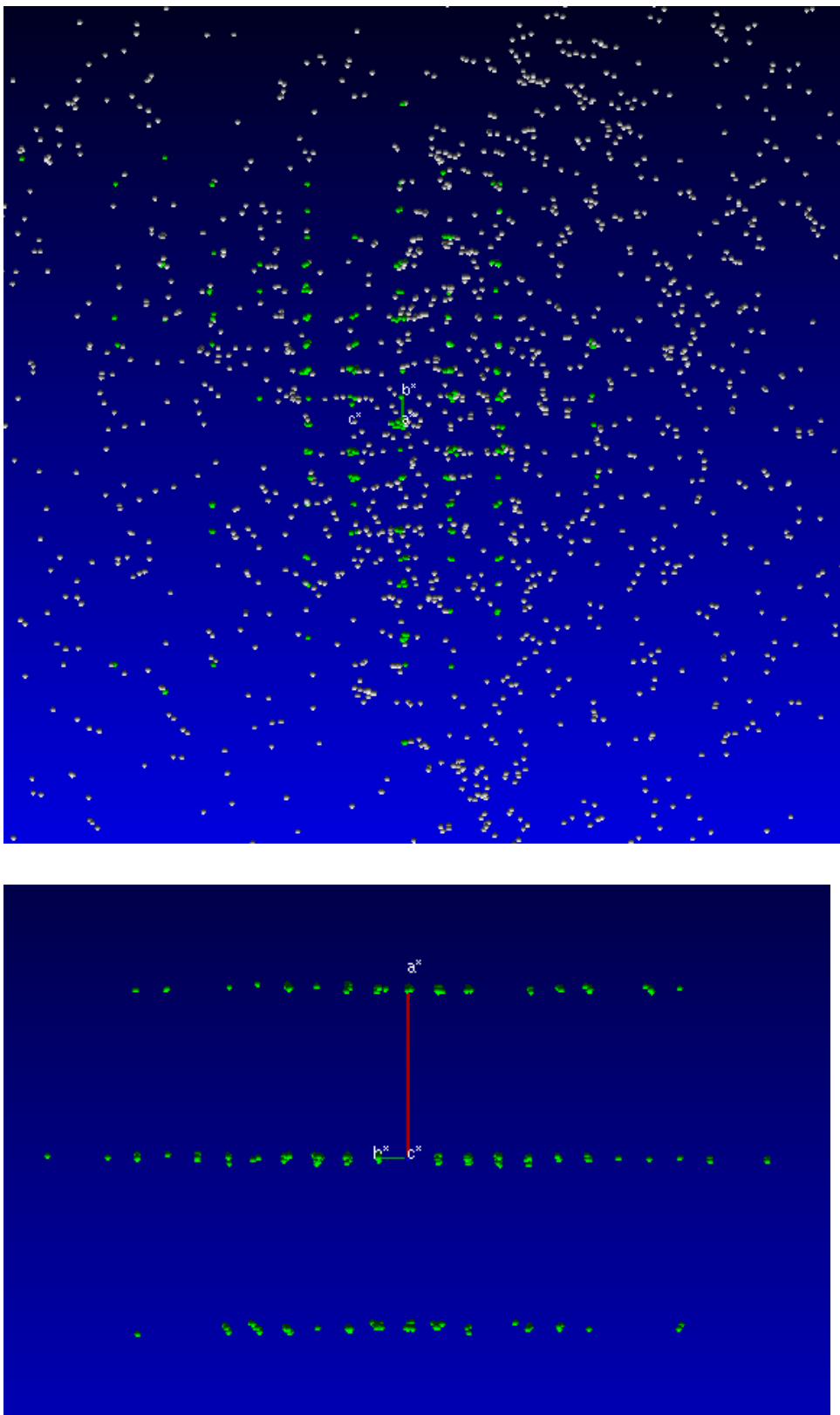


Figure 6-7. Reciprocal lattice of reflections from ONP crystals. (Top) Total reflections from one data collection. (Bottom) Individual lattice from single crystal.

The unit cell of ONP does not correspond with any of the solved structures of ROY, nor does it appear to be any of the forms for which the crystal structure has not yet been obtained – Y04, R05 or RPL based on colour, crystal habit and Raman spectroscopy. RPL was characterised by melting point (mp) and Raman spectroscopy. <sup>4</sup> It has mp 62-63°C and characteristic  $\nu_{\text{CN}}$  Raman shifts at 2210 and 2215  $\text{cm}^{-1}$ . All other forms of ROY have only one peak in this region associated with the  $\nu_{\text{CN}}$  stretch. ONP has only one stretch in this region also, therefore it cannot be the same polymorph as RPL.

Form R05 can also be eliminated as it has distinct Raman stretches  $\nu_{\text{CN}} = 2217\text{cm}^{-1}$  and  $\nu_{\text{NH}} = 3276\text{cm}^{-1}$  which are not present in the spectrum of ONP. It is somewhat more difficult to determine if ONP and Y04 are the same crystals as no Raman spectra or mp are reported for Y04. However, the habits of the two crystal forms are significantly different in both colour and shape, as well as crystallisation method. Additionally, Y04 transforms visibly to the YT04 form over time, and the crystals of ONP do not show evidence of any solid state transformation either visually or by Raman spectroscopy.

Table 6-3. Polymorphs of ROY.

Form	Y	YT04	R	OP	ON	YN	ORP	ONP
Crystal System	monoclinic	monoclinic	triclinic	monoclinic	monoclinic	triclinic	orthorhombic	monoclinic
Space group	$P2_1/n$	$P2_1/n$	$P\bar{1}$	$P2_1/n$	$P2_1/c$	$P\bar{1}$	$Pbca$	-
Habit	yellow prism	yellow prism	red prism	orange plate	orange needles	yellow needles	orange-red plate	orange needles
$a/\text{Å}$	8.5001	8.2324	7.4918	7.976	3.9453	4.5918	13.177	4.03
$b/\text{Å}$	16.413	11.8173	7.7904	13.319	18.685	11.249	8.0209	22.75
$c/\text{Å}$	8.5371	12.3121	11.911	11.676	16.3948	12.315	22.801	12.71
$\alpha/^\circ$	90	90	75.494	90	90	71.194	90	90
$\beta/^\circ$	91.767	102.505	77.806	104.683	93.83	89.852	90	98.89
$\gamma/^\circ$	90	90	63.617	90	90	88.174	90	90
Z	4	4	2	4	4	2	8	-

The melting point of the ONP needles is 102.9°C. This does not correspond with the mp of the known forms (Figure 6-2), including RPL which has mp 62-63°C. ORP, to which ONP appears to be crystallographically related, has a melting point of 97°C, suggesting a difference between the two forms.

#### 6.4 Conclusions

Crystals of ROY were successfully grown by application of high pressure and subsequently retrieved to ambient conditions using the novel method of freezing the sample *in situ* with liquid nitrogen. Raman spectra of the sample show similarities with the ONP, ON and YN forms, based on the  $\nu_{\text{CN}}$  stretches, which vary between polymorphs. The unit cell obtained from synchrotron diffraction data show a crystallographic relationship to the ORP form. ONP may be a high pressure phase of ORP but better quality diffraction data would be required to determine if ONP is a previously unobserved form of ROY (see Conclusions and Future Work).

Considering the results from spectroscopy, diffraction, melting point and observation of the crystals, there is evidence that the needles of ROY grown in the DAC may a previously unseen form of ROY, but further characterisation is required. High pressure crystallisation using DAC compression methods represent a new polymorph discovery method for samples which are stable at ambient conditions once retrieved from the DAC in the correct manner.

## 6.5 References

1. L. Yu, G. A. Stephenson, C. A. Mitchell, C. A. Bunnell, S. V. Snorek, J. J. Bowyer, T. B. Borchardt, J. G. Stowell and S. R. Byrn, *J. Am. Chem. Soc.*, 2000, **122**, 585-591.
2. *UK Eur. Pat.*, 0 454 436 A1, 1991.
3. L. Yu, *Acc. Chem. Res.*, 2010, **43**, 1257-1266.
4. C. A. Mitchell, L. Yu and M. D. Ward, *J. Am. Chem. Soc.*, 2001, **123**, 10830-10839.
5. S. Chen, I. A. Guzei and L. Yu, *J. Am. Chem. Soc.*, 2005, **127**, 9881-9885.
6. S. Chen, H. Xi and L. Yu, *J. Am. Chem. Soc.*, 2005, **127**, 17439-17444.
7. T. A. Zeidan, J. T. Trotta, P. A. Tilak, M. A. Oliveira, R. A. Chiarella, B. M. Foxman, O. Almarsson and M. B. Hickey, *CrystEngComm*, 2016, **18**, 1486-1488.
8. K. M. Lutker, Z. P. Tolstyka and A. J. Matzger, *Cryst. Growth Des.*, 2008, **8**, 136-139.
9. H. Li, J. G. Stowell, T. B. Borchardt and S. R. Byrn, *Cryst. Growth Des.*, 2006, **6**, 2469-2474.
10. T. Gnutzmann, Y. Nguyen Thi, K. Rademann and F. Emmerling, *Cryst. Growth Des.*, 2014, **14**, 6445-6450.
11. J. L. Hilden, C. E. Reyes, M. J. Kelm, J. S. Tan, J. G. Stowell and K. R. Morris, *Cryst. Growth Des.*, 2003, **3**, 921-926.
12. Y. Sun, H. Xi, S. Chen, M. D. Ediger and L. Yu, *J. Phys. Chem. B*, 2008, **112**, 5594-5601.
13. M. Vasileiadis, A. V. Kazantsev, P. G. Karamertzanis, C. S. Adjiman and C. C. Pantelides, *Acta Crystallogr., Sect. B: Struct. Sci.*, 2012, **68**, 677-685.
14. L. Yu, *J. Phys. Chem. A*, 2002, **106**, 544-550.
15. T. Li, P. W. Ayers, S. Liu, M. J. Swadley and C. Aubrey-Medendorp, *Chem. Eur. J.*, 2009, **15**, 361-371.
16. J. A. Foster, K. K. Damodaran, A. Maurin, G. M. Day, H. P. G. Thompson, G. J. Cameron, J. C. Bernal and J. W. Steed, *Chemical Science*, 2017, DOI: 10.1039/C6SC04126D.
17. M. R. Probert, C. M. Robertson, J. A. Coome, J. A. K. Howard, B. C. Michell and A. E. Goeta, *J. Appl. Crystallogr.*, 2010, **43**, 1415-1418.
18. M. R. Probert, J. A. Coome, A. E. Goeta and J. A. K. Howard, *Acta Crystallographica Section A*, 2011, **67**, C528.
19. T. Schulz, K. Meindl, D. Leusser, D. Stern, J. Graf, C. Michaelsen, M. Ruf, G. M. Sheldrick and D. Stalke, *J. Appl. Crystallogr.*, 2009, **42**, 885-891.
20. G. J. Piermarini, S. Block, J. D. Barnett and R. A. Forman, *J. Appl. Phys.*, 1975, **46**, 2774-2780.
21. *APEX2*, 1.08; Bruker AXS Inc.: Madison, WI, 2004.
22. A. V. Valkenburg, H. K. Mao and P. M. Bell, *Carnegie Institution Yearbook 70. Annual Rept. Geoph. Lab.*, 1971, **1970-1971**, 237-238.
23. F. P. A. Fabbiani, G. Buth, D. C. Leventis and A. J. Cruz-Cabeza, *Chem. Commun.*, 2014, **50**, 1817-1819.
24. K. Roszak, A. Katrusiak and A. Katrusiak, *Cryst. Growth Des.*, 2016, **16**, 3947-3953.
25. F. P. A. Fabbiani, B. Dittrich, A. J. Florence, T. Gelbrich, M. B. Hursthouse, W. F. Kuhs, N. Shankland and H. Sowa, *CrystEngComm*, 2009, **11**, 1396-1406.
26. C. P. Price, A. L. Grzesiak and A. J. Matzger, *J. Am. Chem. Soc.*, 2005, **127**, 5512-5517.

# Chapter 7 Conclusions and future work

---

The results herein demonstrate the advantages of using non-typical and non-ambient crystallisation methods in order to fully explore the extensive co-crystal landscape of a given compound or mixture. Standard laboratory crystallisation techniques, while essential and often effective, may not offer the most complete exploration of the properties and behaviour of a chemical system. High pressure crystallisation is an effective and complementary route to obtaining polymorphs previously unseen from ambient pressure methods.

## 7.1 Acid-base co-crystals

Multiple high pressure crystallisation studies conducted on acid-base mixtures which are liquid at ambient conditions have resulted in the discovery of several new co-crystal polymorphs. Two new forms were found for pyridine-formic acid co-crystals from HP crystallisation. At high concentration of FA, proton transfer occurs and a salt co-crystal is obtained. This is consistent with concentration dependent polymorphism observed in the previously known co-crystals of pyridine and formic acid. Five new co-crystals were obtained for DMP-formic acid mixtures. Similar to the pyridine analogues, the neutral equimolar acid-base co-crystal is obtained from both HP and LT crystallisation methods. For the structures where HP/LT polymorphism is evident, there is a non-equimolar acid-base concentration, and proton transfer occurs between the components, resulting in a salt co-crystal. The effect of acidity and basicity has also been highlighted as a consideration in the HP/LT polymorphism of both pyridine and DMP examples. In both mixtures, a high

concentration of acid relative to the base has significant effects on the bonding interactions seen in the crystal structure. When proton transfer occurs between the base and formic acid, the resulting ionic interaction between components becomes an important factor in the polymorphism of their crystal structures. In addition to insights into the structure and behaviour of these particular co-crystals, their determination contributes to what existing literature there is regarding low melting molecular co-crystals obtained from *in situ* crystallisation and diffraction techniques.

In order to further explore the nature of these co-crystals and the prevalence of HP/LT polymorphism, a more extensive library of acid and base mixtures should be studied. The co-crystallisation of other aromatic bases with simple acids may offer insight into why some co-crystals exhibit HP/LT polymorphism, while others do not. Given the structures obtained for pyridine and DMP co-crystals, it stands to reason that other appropriate aromatics might display the same crystallisation behaviour. A systematic study should be carried out in order to determine what characteristics are desirable for HP/LT polymorphism, such as basicity, acidity, functionality, substitution and concentration effects. Any information and conclusions obtained from such work would contribute to the existing body of knowledge which informs fields such as crystal engineering and crystal structure prediction. These areas in turn have practical application in the pharmaceutical industry, for example, if compounds were chosen which are used as co-formers or are structurally related to molecules used in the drug and food industries.



## 7.2 High pressure ROY crystallisation

ROY was chosen as the subject of a high pressure solution crystallisation due to its extensive polymorphism. An acetone solution was chosen for the high solubility of ROY in this solvent, which is preferable for this type of *in situ* crystallisation. Once the correct concentration and crystallisation conditions were obtained, needles of ROY were isolated in the DAC (named ONP) and studied by Raman spectroscopy. The needles were recovered from the cell and synchrotron diffraction data were collected. There is evidence that a new form of ROY has been obtained by *in situ* pressurisation and crystal growth, based on the unit cell indexed from 213 reflections. However, due to the fragile and clustered nature of the ONP crystals, and the presence of ruby dust in the sample, complete structure solution and refinement could not be achieved. Raman spectroscopy indicates similarities between ONP and the known forms ORP, ON and Y. Further investigation into the ONP form is required in order to determine with any degree of certainty whether it is a new form or one of the known forms. If ONP corresponds to the ORP form, it is notable as acetone has not previously been reported as a crystallisation solvent for this polymorph, and the crystal habit and nucleation conditions are considerably different to those observed before.

The next stage of this project would be to recrystallise ONP by DAC pressurisation, without ruby present in the sample chamber, and retrieval of the crystals to ambient conditions. The synchrotron diffraction experiment should be repeated, preferably on a single crystals or a smaller cluster of crystals than were in the original sample.

Structure solution and refinement would confirm the existence of a new polymorph and how it is related to the ORP form of ROY.

Additionally, further Raman spectroscopy studies should be carried out on samples of both the ONP needles obtained from the DAC and ORP crystals grown at ambient pressures, in order to determine if there are Raman characteristics unique to ONP, which would aid in identification of the phase in the future.

Further high pressure experiments would include compression of an existing crystal of ORP to see if a single-crystal-to-single-crystal phase transformation is possible from ORP to ONP. If there is a phase transition and the crystal remains intact, the pressure could be reduced back to ambient conditions and diffraction data collected to determine if the transition is reversible.

As ROY has been the subject of CSP techniques, it would be useful to compare the unit cell parameters of ONP with predicted structures which have not been observed experimentally. If a close match exists, some insight could be gained into the nature of ONP if recrystallisation and structure determination by conventional methods prove unsuccessful.

### 7.3 Urea inclusion compounds

Through a detailed study of a series of UICs using both X-ray and neutron diffraction techniques, the relationship between guest and host in these clathrate compounds has been thoroughly explored. The effect of guest size, shape and characteristics have been shown to have a significant effect on the hydrogen bonding of urea in these systems. Perturbations arise in the channel structure which manifest as

changes to the individual hydrogen bonds which make up the system, as well a loss of planarity in urea molecules in the 1,6-dibromohexane and 2,7-octanedione examples. The urea host network proves to be quite versatile in adapting to various guest compounds, such as large halo-alkanes or the introduction of additional hydrogen bond acceptors to the system as with diketones. The host can undergo significant deviation from the model hexagonal system without a loss of structural integrity. However, if a guest is used which does meet the criteria for UIC formation, a stoichiometric co-crystal may be observed instead such as with DMF. In this case, there are similarities between the hydrogen bonding in the UIC examples and the co-crystal, but the hexagonal channel structure is no longer present.

Further study into these clathrate compounds would include collecting diffraction data on further examples of UICs, preferably those which exhibit different guest types and bonding patterns to those discussed in this work. An additional dimension to the investigation would be gained by studying the effects of systematically changing the guest compound in thiourea inclusion compounds. These exhibit similar structural features to UICs with a greater cross-sectional channel size and different guest requirements and also often have an incommensurate host-guest relationship.

# Appendix A

---

## Courses

- 14<sup>th</sup> BCA/CCG Intensive Teaching School in X-ray Structure Analysis April 2013, Durham University, Durham, UK.

## Conferences and Meetings

- 28<sup>th</sup> European Crystallographic Association Meeting 2013, Warwick, UK.
- 14<sup>th</sup> International Seminar on Inclusion Compounds 2013, Heriot-Watt University, UK.
- BCA Spring Meeting, 7-10 April 2014, Loughborough University, UK.
- 23<sup>rd</sup> Congress and General Assembly of the International Union of Crystallography 2014, Montreal, Canada.
- British Crystallographic Association Spring meeting 2016, Nottingham University, UK.

## Publications

- Structure of organic solids at low temperature and high pressure. R. Lee, J. A. K. Howard, M. R. Probert, J. W. Steed, *Chem. Soc. Rev.*, 2014, **43**, 4300.
- Expanding the pyridine-formic acid cocrystal landscape under extreme conditions. R. Lee, A. J. Firbank, M. R. Probert, J. W. Steed. *Cryst. Growth & Des.*, 2016, **16**, 4005.
- Neutron diffraction studies on guest-induced distortions in urea inclusion compounds. R. Lee, S. Mason, E. Mossou, G. Lamming, M. R. Probert, J. W. Steed. *Cryst. Growth & Des.*, 2016.

## Appendix B – Crystallographic Information

---

CD containing CIF and checkCIF files of crystal structures.